Structure, Petrography, Geochemistry and Geochronology of Gabbroic and Associated Granitoid Rocks in Parts of the South Delhi Fold Belt, Rajasthan, India: Implications for tectonic evolution

Thesis submitted by

Anirban Manna

Index no. 14/20/Geol. Sc./26

Registration No: SOGE01101420

Thesis submitted to Jadavpur University

For the degree of Doctor of Philosophy (Science)

Department of Geological Sciences
Jadavpur University
Kolkata-700032
August 2024

যাদবপুর বিশ্ববিদ্যালয়
কলকাতা - ৭০০০৩২, ভারত

JADAVPUR UNIVERSITY
KOLKATA-700 032, INDIA

FACULTY OF SCIENCE : DEPARTMENT OF GEOLOGICAL SCIENCES

CERTIFICATE FROM THE SUPERVISOR

This is to certify that the thesis entitled "**Structure, Petrography, Geochemistry and Geochronology of Gabbroic and Associated Granitoid Rocks in Parts of the South Delhi Fold Belt, Rajasthan, India: Implications for Tectonic Evolution**", submitted by **Mr. Anirban Manna,** who got his name registered on **25.09.2020** for the award of **PhD (Science)** degree of Jadavpur University, is absolutely based upon his own work under the supervision of **Dr. Sadhana M. Chatterjee** and that neither this thesis nor any part of it has been submitted for either any degree/ diploma or any other academic award anywhere before.

Sadhana M Chatterjee
20/08/2024

Dr. Sadhana M Chatterjee
Associate Professor
Department of Geological Sciences
Jadavpur University
Kolkata-700032, India

Dr. Sadhana M Chatterjee
Associate Professor
Department of Geological Sciences
Jadavpur University
Kolkata-700 032

Dedicated

to my Family

ACKNOWLEDGEMENTS

I would like to express my deep sense of gratitude to my supervisor, Dr. Sadhana M. Chatterjee, Associate Professor, Department of Geological Sciences, Jadavpur University, Kolkata, for her unwavering support and guidance throughout this work. Her numerous ideas, suggestions and constant encouragement have been invaluable in completing my thesis.

I also like to thank all the members of the Department of Geological Sciences, including the faculty, research scholars, fellow students, and non-teaching staff, for their assistance and support during the course of my work.

My gratitude also goes to the Council of Scientific and Industrial Research for providing me with a research fellowship for five years, which made this work possible.

I am especially thankful to my lab mates Dr. Alip Roy and Dr. Ayan Kumar Sarkar for their help in various ways throughout this journey.

Lastly, I am deeply grateful to my family for their constant support, encouragement and all kinds of help throughout this work.

Anirban Manna

Table of contents

Abstract:

In the north-western Indian shield, the South Delhi Fold Belt (SDFB) of Proterozoic age is trending NE-SW. The SDFB is juxtaposed with the Marwar craton along its western margin through the Phulad Shear Zone (PSZ). The PSZ is described as a terrane boundary shear zone that separates the SDFB to the east and the Marwar craton to the west. The PSZ has developed in a ductile transpressional regime with a top-to-the-NNW reverse movement around ~820 Ma. Within the SDFB, there is a substantial occurrence of isolated gabbro rocks and ~1 Ga granites extending in an NE-SW orientation, mirroring the alignment of the PSZ and the regional trend of the SDFB. The origin of these gabbro rocks has been a subject of intense debate, and the ~1 Ga granites from the SDFB are often correlated with the assembly of the Rodinia Supercontinent. The present study integrates field observations, petrology, geochemistry, and geochronology of the gabbro and ~1Ga granites of SDFB that occur in a 6-15 km wide linear belt extending for more than 200km.

The gabbro and the granite rocks occur as isolated patches along a linear belt and are variably deformed. Detailed investigations reveal synchronous foliations in the gabbro rocks, granites, and mylonites within the PSZ, indicating a common stress regime. Petrographic examinations were conducted on all the sampled gabbro and granite bodies along the fold belt. The gabbro rocks exhibit igneous assemblages with notable metamorphic imprints. The gabbro shows a prominent development of solid-state foliation, characterized by the preferred orientation of amphibole and plagioclase. The gabbroic rocks depict the replacement of primary minerals by amphibole and garnet. In the granites, the replacement of primary minerals appears to have occurred in two stages in all the separated granite bodies. Initially, amphibole was replaced sequentially by an epidote–titanite–quartz symplectite, followed by the formation of garnet. The euhedral garnet grains and titanite coronas are post-tectonic relative to the regional fabric, whereas the symplectite assemblage formed during deformation (PSZ formation).

Geochemically, these gabbro rocks exhibit a tholeiitic composition with flat HREE trends, whereas LREEs display a wide range of distributions from N-MORB to E-MORB. Geochemically, the granites are ferroan, calc-alkalic and metaluminous. Granite discrimination diagrams confirm A-type, further classified as A_2 type granite. Observations revealed a bimodal magmatic composition in the SDFB, encompassing both gabbro rocks and A-type granite. Both, these gabbroic and granite rocks show within-plate signatures in their respective tectonic discrimination diagrams, indicating extension-related magmatism. U-Pb zircon dates from the gabbro rocks indicate a magmatic Concordia age of 983.4 ± 6.0 Ma, while the granites indicate a magmatic Concordia age of 970.7 ± 2.9 Ma, overprinted by a metamorphic Concordia age of 824.5 ± 5.3 Ma. The later age coinciding with the NNW reverse sense of movement of the PSZ. Thus, it is suggested that the gabbroic and granitic rocks formed during crustal thinning at ~980-970 Ma, followed by the solid-state exhumation of the rocks that occurred at 820 Ma, coinciding with PSZ formation.

By integrating field relations, petrography, geochemistry, and geochronology of the studied gabbroic and granitic rocks, the possible tectonic model suggests that crustal thinning occurred due to the rollback of a subducting oceanic plate. This process facilitated mantle upwelling and the formation of basaltic magma, which accumulated in the lower crust. Heat flow from the upwelling mantle and crystallizing mafic phases caused significant partial melting in the continental crust, resulting in the formation of gabbro through mafic magma emplacement and granite through crustal melting. The oldest reported age of the basement rocks of the Marwar Craton, dated to ~880 to 860 Ma, suggests that it sutured with remaining India around 820 Ma. The exhumation of the gabbro and granitic rocks occurred during the suturing of the Marwar Craton with the SDFB along the Phulad Shear Zone around 820 Ma.

Chapter 1

Introduction

1.1: Introduction:

In northwestern India, the South Delhi Fold Belt (SDFB) is a NE-SW trending Proterozoic fold belt. The westernmost part of the SDFB is marked by the Phulad Shear Zone (PSZ), which exposes thickness (5-10 km) of mafic-ultramafic complexes like gabbro, a few ultramafic bodies and granite intrusive over a distance of more than 200 km. These mafic rock formations have been identified by previous workers as an ophiolitic suite, representing remnants of Proterozoic oceanic crust within the Proterozoic Delhi Supergroup in Rajasthan, India (Sudgen et al., 1990; Gupta et al., 1980; Khan et al., 2005, 2018). However, some researchers argue that it is a mafic sequence similar to those found in extensional regions (Roy, 1988; Volpe & Macdougall 1990). These mafic rocks are always closely associated with the granitic rocks. All these mafic and granite rocks are strictly restricted within the SDFB (Map 1). Different researchers have studied the isolated granite plutons separately, giving them distinct names, such as Sendra granite (Tobisch et al. 1994), Chang granite (Pandit et al. 2003; Tiwana et al. 2022), Moras Granite (Zhao et al. 2018), Foliated Granite (Dharma Rao et al. 2013). All these granites are dated as ~1 Ga (Dharma Rao et al. 2013; Pandit et al. 2003; Tiwana et al. 2022; Tobisch et al. 1994; Zhao et al. 2018**)**. However, there are no reports of any zircon age of the mafic rocks to date (Map 2). The availability of ~1 Ga magmatic rocks in northwestern India has prompted researchers to suggest Grenvillian age collisional orogeny between the Marwar craton to the west and the North Indian block to the east (Bhowmik et al., 2009, 2010; Deb et al., 2001; Pandit et al., 2003). However, recent studies argue that the Greater India landmass was accreted with the Malani Igneous Suite (MIS) hosted Marwar craton along PSZ as late as 810-820 Ma (Chatterjee et al., 2017, 2020, 2023). It is unclear if these granite plutons and the mafic rocks indeed represent separate events that were emplaced with distinct geological histories or constitute a single event found in spatially separated outcrops formed during a single orogenic event.

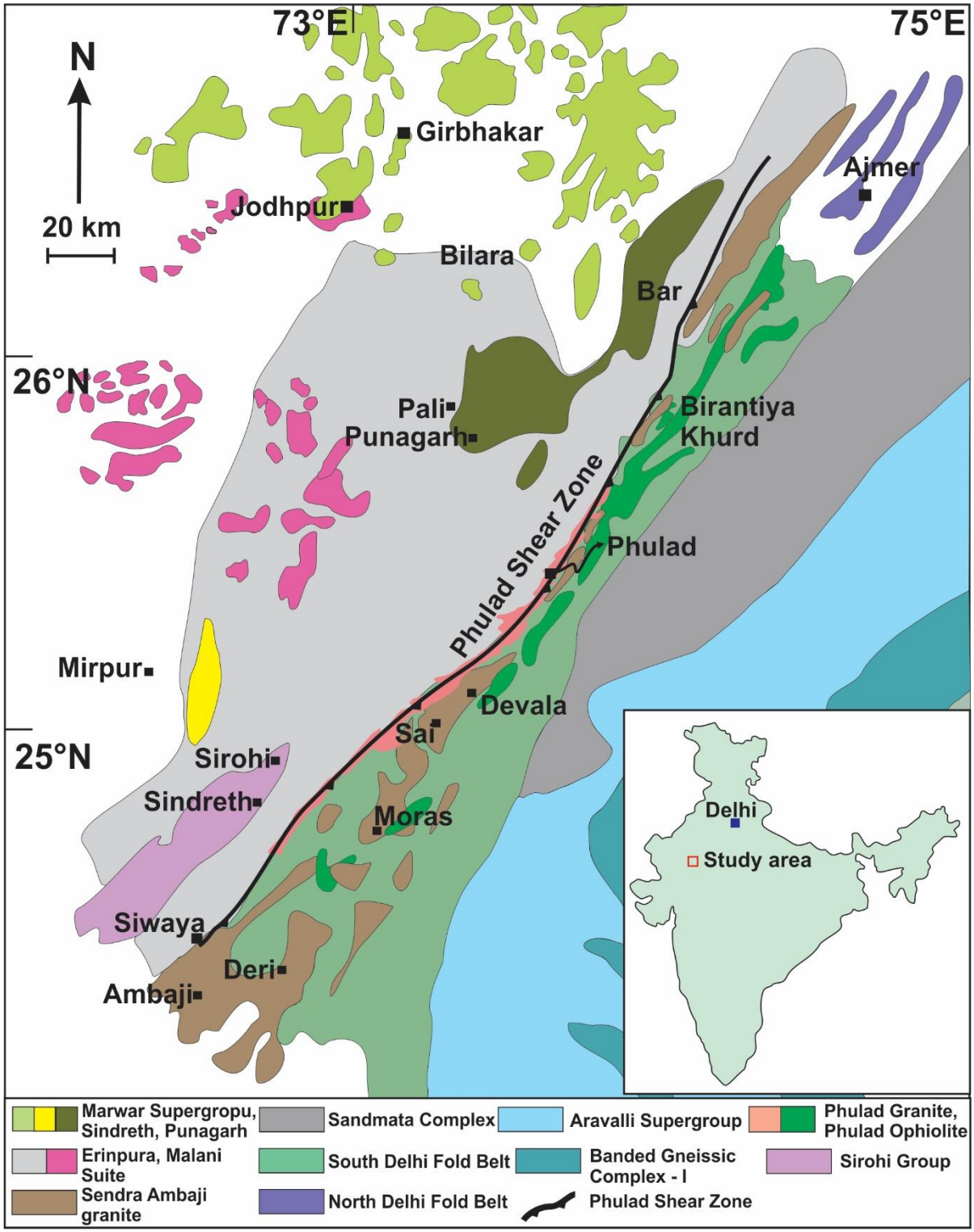

Map 1. Geological map depicting the different crustal domains in northwestern India (modified after Chatterjee et al., 2020; Heron, 1953; Gupta et al., 1980; and Roy and Jakhar, 2002).

It is, therefore, crucial to understand the proper tectonic set-up of this terrane around ~1Ga by integrating detailed field relations, petrological, geochemical, and geochronological information on the gabbro rocks and the closely associated granitic rocks before evaluating India's role and position with respect to the Rodinia supercontinental framework.

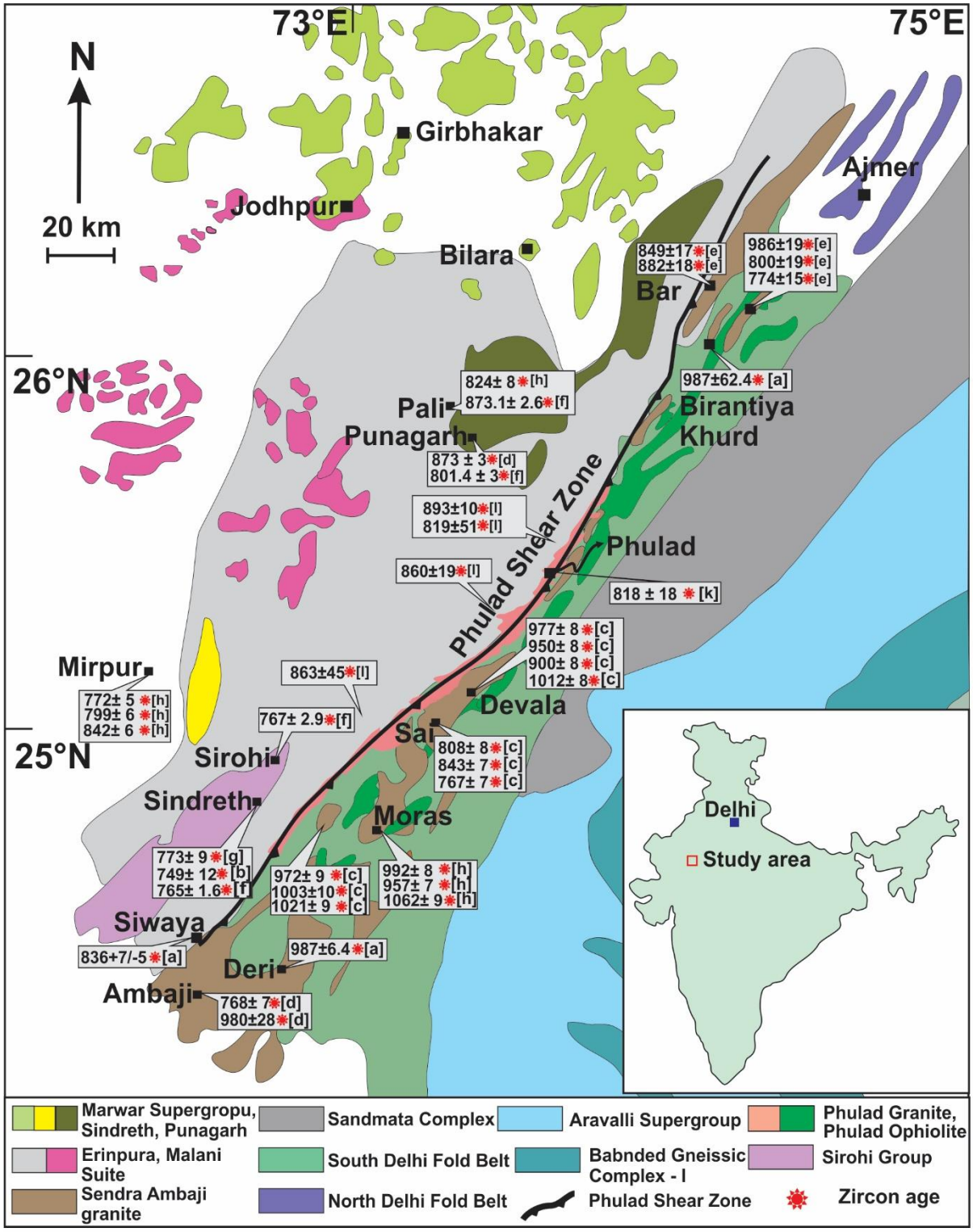

Map 2. Geological map depicting the different crustal domains in northwestern India (modified after Chatterjee et al., 2020; Heron, 1953; Gupta et al., 1980; and Roy and Jakhar, 2002). Available concordant zircon data are shown in boxes. Data sources: (a) Deb et al. (2001); (b) de Wall et al. (2018); (c) de Wall et al. (2022); (d) Dharma Rao et al. (2013); (e) Meert et al. (2013); (f) Singh et al. (2010); (g) Singh et al. (2021); (h) Van Lente et al. (2009); (i) Wang et al. (2018); (j) Zhao et al. (2018); (k) Chatterjee et al. (2020); and (l) Chatterjee et al. (2023).

1.2: Geological background:

The SDFB of northwestern Indian shield is a NE-SW trending; multiply folded and poly-metamorphosed rocks of Proterozoic age (Chatterjee et al., 2017; Gupta et al., 1980; Heron, 1953; Roy and Jakhar, 2002; Sinha Roy, 1998). To the west of SDFB lies the Marwar Craton and the boundary between them is defined by Phulad Shear Zone (PSZ) (Chatterjee et al., 2017; Ghosh et al., 1999; Sengupta and Ghosh, 2004; Sengupta and Chatterjee 2016). The PSZ is recognized on the basis of extensive development of mylonite (Ghosh et al., 1999; Golani et al., 1998). All the different rocks along this PSZ are transformed into mylonites. The main shear zone is composed of calcareous unit intercalated with quartzo-feldspathic layers. The mylonitic foliation dips steeply towards southeast with prominent development of steep stretching and striping lineation (Sengupta and Ghosh, 2007). The shear zone shows a regional NE-SW strike. However, along the strike, at regular interval, the shear zone deviates from its regional trend to small N-S bends (Chatterjee et al., 2020). The shear zone is characterized by development of sheath folds with apical direction parallel to the stretching lineation. Field relationships show evidences of stretching in both XZ (subvertical section perpendicular to foliation and parallel to lineation) and YZ (subhorizontal section perpendicular to foliation and lineation) sections indicating a three-dimensional strain with a component of flattening across the shear zone (Sengupta and Ghosh, 2004; Chatterjee et al., 2017, 2020). In the XZ section, mesoscopic structures (asymmetric folds) and inclusion trails in pophyroblasts suggest top-to-the-NNW reverse sense of movement (Chatterjee et al., 2020). Taken together, these features indicate that the shear zone developed during a transpression regime with top-to-the-NNW reverse sense of movement. The rocks to the west i.e. the Marwar craton belong to footwall unit and the rocks to the east of PSZ i.e. SDFB to the hanging wall unit.

The Marwar craton, neighbouring the PSZ, mainly contains variably deformed megacrystic granites. Three phases of ductile deformation have been reported from the Marwar craton (Chatterjee et al., 2023). The mean orientation of foliation and lineation of the third deformation in the megacrystic granites of the Marwar craton broadly overlaps with that of the PSZ mylonites and is interpreted to have formed synchronously (Chatterjee et al. 2023). The deformation in the megacrystic granitic rocks increases from weakly-deformed to mylonitic, neighbouring the PSZ (Roy Choudhury et al. 2016).

The SDFB consists of mica schists inter-layered with calc-silicate rocks, amphibolites, gabbro, deformed granitoid bodies and quartzites. Two phases of ductile deformation (D1, D2) have been reported from the SDFB (Chatterjee et al. 2017; Gupta et al. 1995; Roy and Sharma 1999; Roy and Jakhar 2002). The first generation of folds is preserved as rootless hinges interfolial to S1 schistosity. This S1 schistosity is again folded to give rise to F2 folds with a NNE-trending axial plane. Close to the PSZ, all rock types show strong development of a single foliation and are strictly parallel to the mylonitic fabrics in the PSZ. The present study primarily focuses on the gabbroic rocks and ~1 Ga granites that occur exclusively within this SDFB and east of PSZ (Map 2). These granites are closely associated with gabbroic rocks (Map 1, 2).

There is another porphyritic granite named Phulad granite. The Phulad granite is porphyritic in nature and completely different from the megacrystic granite of the Marwar craton (Chatterjee et al., 2023) and the ~1 Ga granites. This Phulad granite is found to intrude both the megacrystic rocks of the Marwar craton and the rocks of SDFB and is interpreted as syn-tectonic granite that emplaced during the shearing of the PSZ (Chatterjee et al, 2020).

1.3: Definition of the problem:

In SDFB there are several isolated reports of ~1Ga intrusives, particularly granite plutons, within the SDFB (Map 1). The emplacement of these granites coincides with the broad timing of the amalgamation of crustal blocks forming the Rodinia supercontinent (Bhowmik et al., 2009, 2010; Deb et al., 2001; Pandit et al., 2003). Different researchers have studied these isolated granite plutons separately, giving them distinct names, such as Sendra granite (Tobisch et al. 1994), Chang granite (Pandit et al. 2003; Tiwana et al. 2022), Moras Granite (Zhao et al. 2018), Foliated Granite (Dharma Rao et al. 2013). These granites are closely associated with the mafic rocks of SDFB. However, there has been no attempt to correlate these ~1 Ga granites and the associated mafic rocks by combining their structural, petrological and geochemical aspects approaches. It is, therefore, crucial to understand the proper tectonic set-up of this terrane around ~1Ga by integrating detailed field relations, petrological, geochemical and geochronology of the mafic rocks and the associated granitic rocks before evaluating the role and position of India with respect to Rodinia supercontinental framework.

The present work aims to reconstruct the detailed field relations, mesoscopic and microscopic structures of the gabbro and associated ~1Ga granites, and their relationship with the PSZ; their petrographic, geochemistry and geochronology to understand the process of granite and gabbro emplacement and discuss the implications of the outcomes for the tectonics of the region.

1.4: **The objective of the Present Work:**

1. Detailed study of mesoscopic structural elements of gabbro and granitic rocks and their relationship with the PSZ, if any.

2. Detailed petrographic study of the gabbro and granites with special emphasis on understanding the magmatic and metamorphic processes.

3. Geochemical study (major, trace and REE patterns) of the gabbro and the granite to understand the petrogenesis and tectonic setting of the study area.

4. Geochronological study of gabbro and granite using conventional zircon age dating technique.

5. Integrating all the above-mentioned data to understand the tectonic setting of the gabbro and granites of SDFB.

1.5: Location, physiography and climate:

1.5.1: Location:

SDFB is located in the southern part of Rajasthan state in India. The scope of the current study encompasses 200km length and 10-15km breadth along and across SDFB east to the Phulad Shear Zone (PSZ). The area falls within the Survey of India toposheets: 45D/13, 45D/14, 45D/15, 45F/16, 45G/4, 45G/8, 45G/10, 45G/11, 45G/12, 45G/13, 45G/14, 45G/15, and 45H/1, 45H/2, 45H/3, 45H/5, 45J/2, 45J/3, 45J/4, 45J/7, and 45K/1 arranged sequentially from north to south in Rajasthan. Geographically, it is bounded by latitudes ranging from 24°15'N to 26°N and longitudes from 72°45'E to 74°15'E.

Accessibility to the field area is well-established. To the north, it is well-connected to the Jaipur Railway Junction, while the Ajmer Railway Junction-Udaipur section of the Western Railway traverses the southern part of the area. This section includes the Marwar Junction and Beawar Railway station. Various roads, such as National Highway NH-62, NH-27, State Highway, and local village roads, provide access to the entire field area. This region forms a

part of the primary NE-SW trending Aravalli Mountains and constitutes the geologically western portion of the Southern Delhi Fold Belt (SDFB).

1.5.2: Physiography of the Study Area:

The study area can be categorized into three distinct domains: (i) the western sandy plains, (ii) the hilly ranges, and (iii) the eastern plains. These divisions are based on the prevailing relief features and serve as a foundation for examining the geomorphic evolution of the region, which has been shaped through numerous erosional cycles represented by various landforms. The area boasts a mature topography, characterized by flat-topped mountain ridges, escarpments, inselberg surfaces, river valleys, intermontane valleys, and extensive plains. The terrain throughout the region is predominantly undulating in nature and is dominated by hilly landscapes.

1.5.3: Climate:

The study area falls within a tropical, warm climate zone and is in close proximity to the Thar Desert in west Rajasthan. Consequently, the region experiences significant diurnal temperature fluctuations. Daytime temperatures can soar up to 50°C during the summer months, and even during winter, daytime temperatures remain around 35°C, dropping to as low as 5°C at night. The average annual rainfall is quite limited, typically ranging from 5 to 10 cm. Generally, the most suitable time for fieldwork is between September and February. However, it's worth noting that the climate in Rajasthan has undergone changes in recent years, with a reduction in the temperature gap between summer and winter due to increased plantation efforts.

Chapter 2

Field relations and deformation patterns

2.1: Introduction:

The present study focuses on the isolated gabbro and granite rocks within the SDFB. These granites within the SDFB are pink coloured, medium grained, homogeneous, and are completely different from the Megacrystic granite and Phulad granite. The Megacrystic granites are porphyritic and restricted to the Marwar craton, whereas phulad granite is also a porphyritic granite and found in the Marwar craton and also in SDFB. The present work traced these gabbro and medium grained, homogeneous granite rocks within the SDFB for more than 200 km, extending from Beawar in the north to Devala in the south. The new satellite image shows that these mafic rocks and granite extend parallel to the PSZ and strictly occur within the SDFB along a narrow linear belt (Figures 2.1 and 2.2).

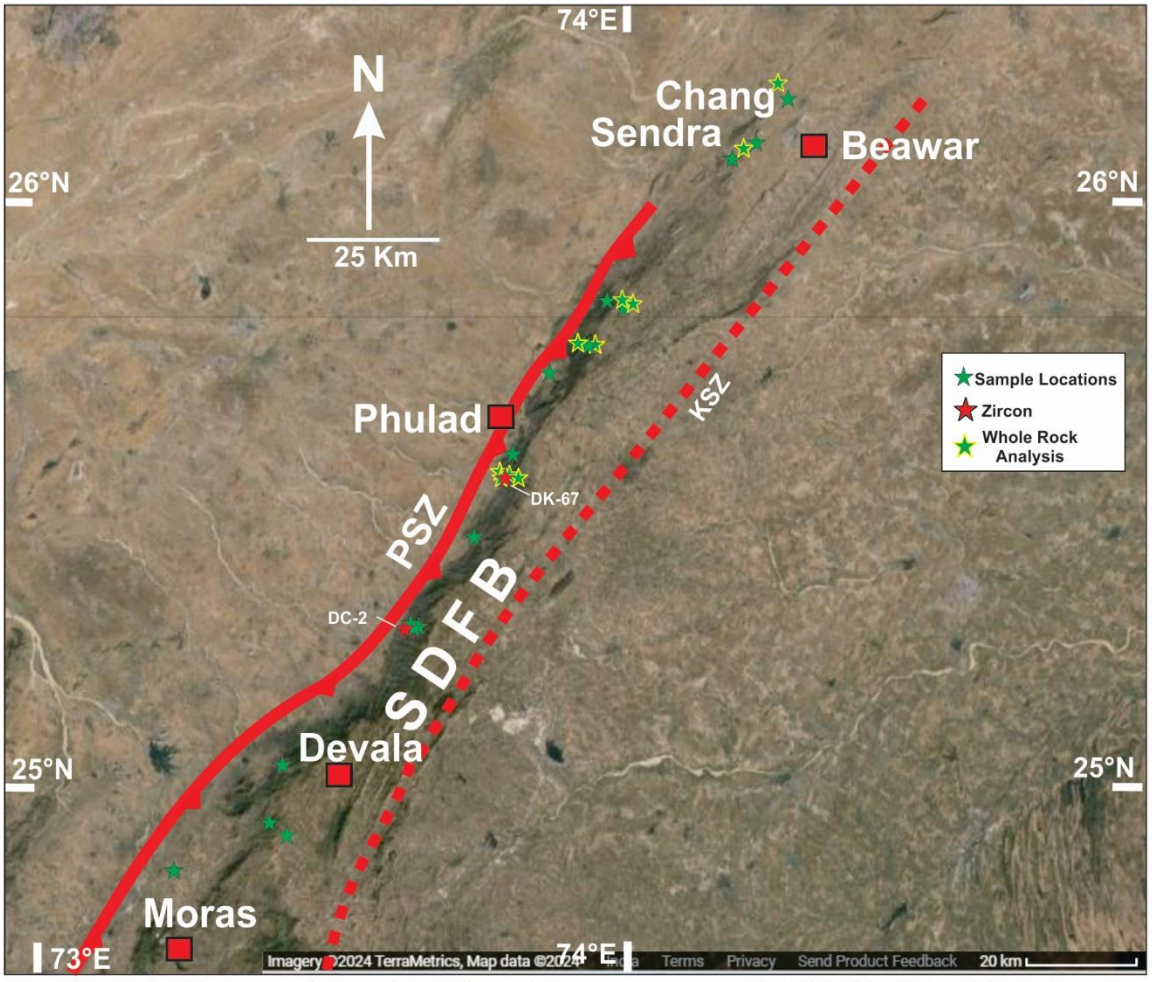

Fig. 2.1. Satellite image taken from Google imagery, map data © 2024 of the SDFB showing the disposition of the sample locations of gabbro rocks.

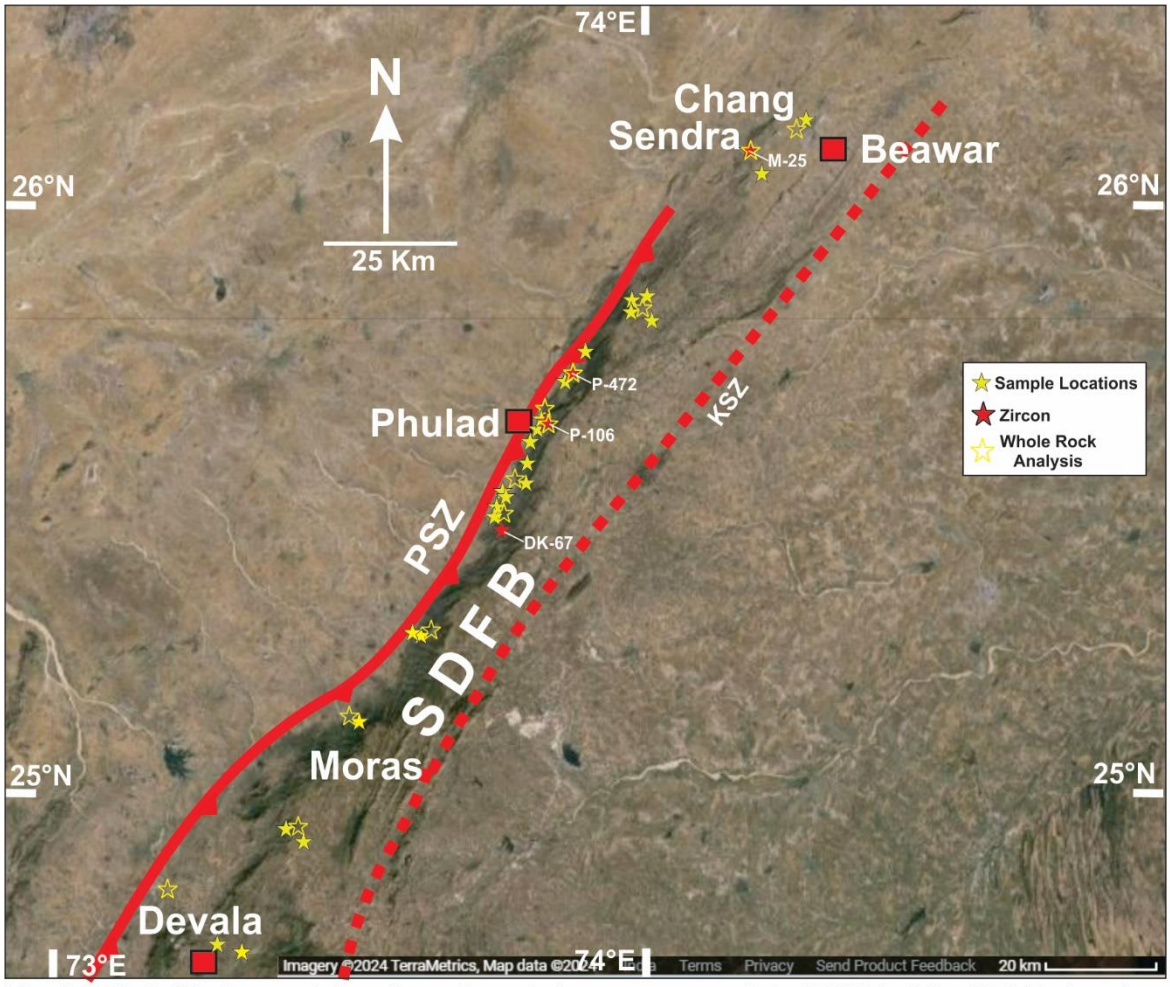

Fig. 2.2. Satellite image taken from Google imagery, map data © 2024 of the SDFB showing the disposition of the sample locations of granitic rocks.

Both the gabbro (Fig. 2.3 a) and the granites (Fig. 2.3 b) are closely associated with each other (Fig. 2.3 c) and restricted within the SDFB and are variably deformed. It is, therefore, crucial to understand the deformation patterns in these rocks and their relationship with the crustal-scale PSZ deformation. The following sections describe the detailed structural study of the PSZ and its relationship with the gabbro (Fig. 2.3 a) and granitic bodies (Fig. 2.3 b) and the regional deformation of the SDFB based on rigorous fieldwork.

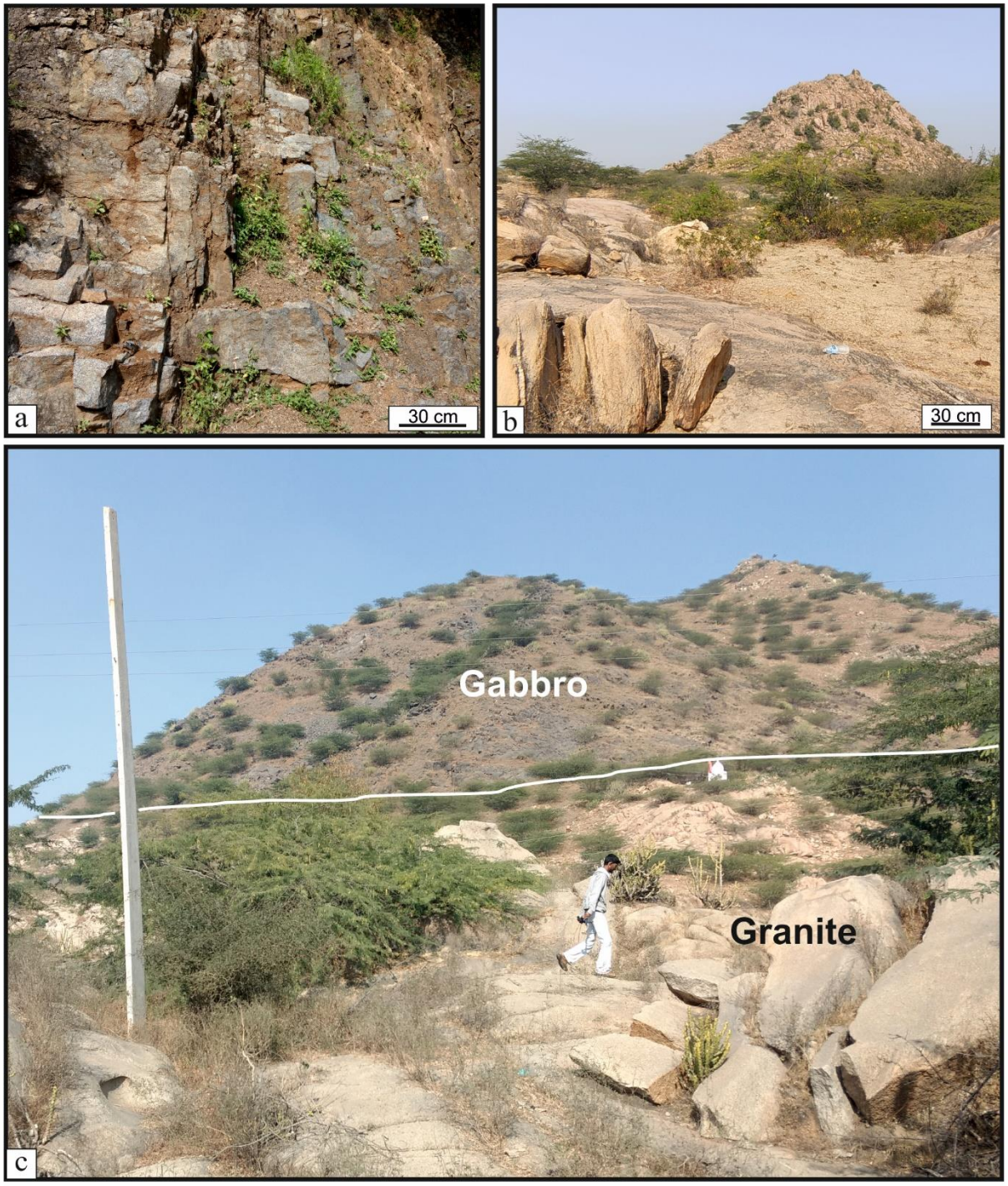

Fig. 2.3. Field photographs showing (a) Gabbro, dark coloured, medium to large grain, exposed within the SDFB, (b) The granite plutons, pink in colour, medium grained, equigranular, exposed within the SDFB exibit typical sheroidal weathering pattern, (c) Gabbro and granite plutons always associated with each other.

2.2: Phulad Shear Zone

The PSZ is distinguished by the strong development of mylonitic foliation within the intercalated calcareous quartzo-feldspathic layers (Fig. 2.4 a). It is characterized by a steep

southeast ward dip and a prominent set of steep oblique striping (see Fig. 2.4 b). A stereoplot illustrates both the foliation and steep plunging lineation within the PSZ (Fig. 2.4 d). Stereographic analysis of the foliation within the mylonites reveals an average orientation of 25°→77°E. The lineation data reveal a steep plunge towards SSE (with a mean orientation of 68°→169°) (Fig. 2.4 d). In the XZ section (a sub-vertical section perpendicular to foliation and parallel to lineation), asymmetric field features are observed, implying a top-to-the-NNW reverse sense of movement (Fig. 2.4 c). This movement direction in the PSZ aligns with the

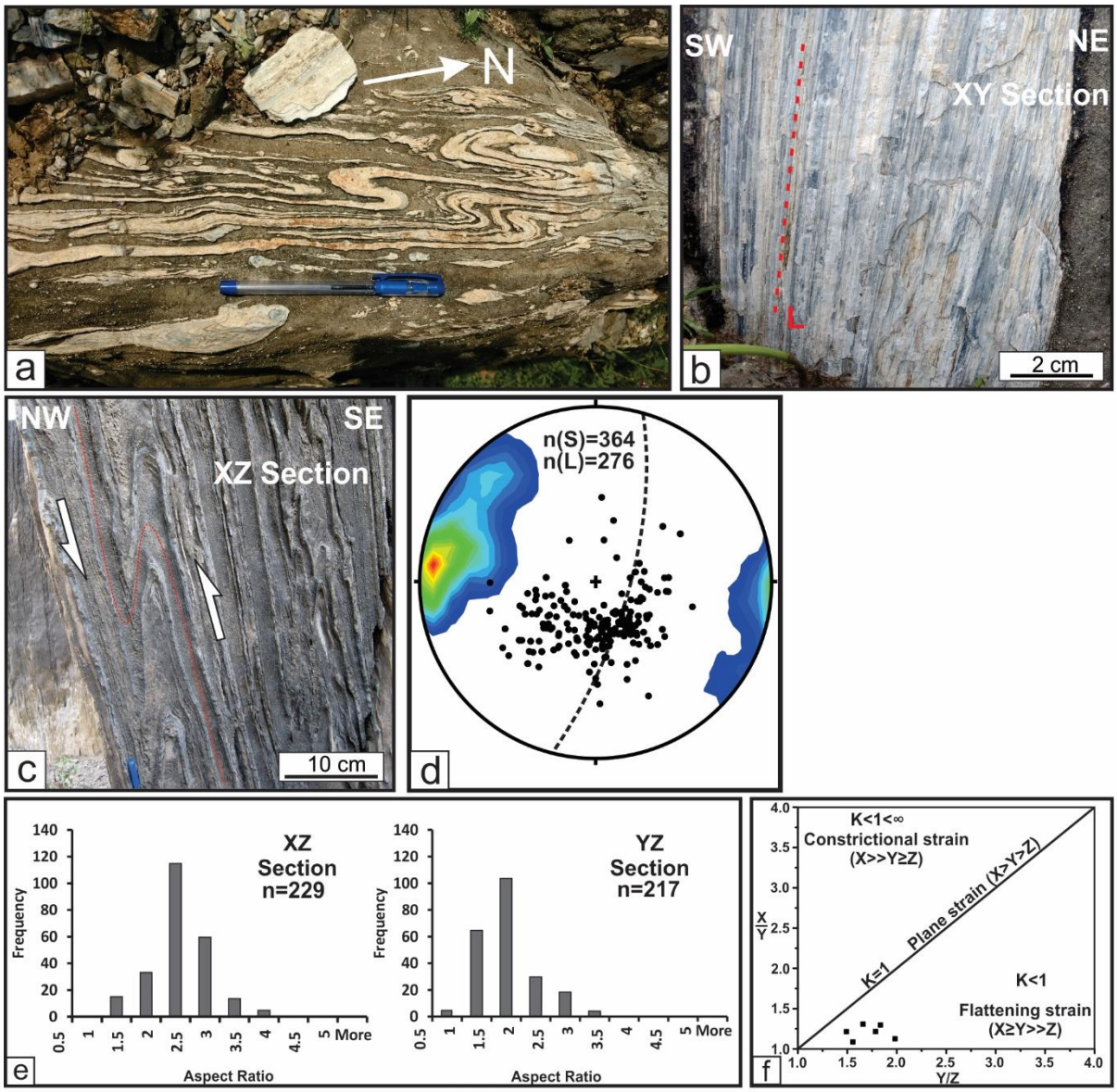

Fig. 2.4. Field photographs showing (a) Mylonitised calcareous unit intercalated with quartzo-feldspathic layers, (b) Prominant down dip striping lineation, (c) Assymetric fold pattern with top to the NNW reverse sence of movement on sub-vertical section, (d) Stereograph showing a mean orientation of 25°/77°E and the lineation show mean principal direction being 68°→169°, (e) Histograms showing the aspect ratio of feldspar porphyroclasts in the quartzofeldspathic mylonites in the XZ and YZ sections. (f) Flinn diagram shows the flattening type of deformation in the granites. n = number of data. n(S) = Foliation data, n(L) =Lineation data.

stretching lineation and is perpendicular to the vorticity axis (Sengupta and Ghosh, 2004, 2007; Chatterjee et al., 2017). Due to this oblique reverse slip movement within the shear zone, there is a component of sinistral slip movement on the sub-horizontal section. In both the XZ and YZ sections (which are perpendicular to foliation and lineation), the feldspar grains within quartzo-feldspathic mylonites exhibit stretching. Notably, the stretching along the x-axis is considerably more pronounced than along the y-axis (Fig 2.4 e), indicating a general flattening type of deformation (Fig. 2.4 e) ($X > Y > 1 > Z$) across the shear zone (Sengupta and Ghosh, 2004; Sengupta and Chatterjee, 2016). All these features collectively suggest that PSZ has developed under a top-to-the-NNW reverse sense of movement within a transpressional setting, where there is a strong component of compression along with a simple shear.

2.3: Field Relations and Deformational Patterns of the Gabbro

The gabbro rocks within SDFB form elongated isolated bodies within a narrow linear zone, extending over a distance of more than 200 km (as depicted in the Fig. 2.1). During the course of this study, detailed fieldwork of the SDFB was conducted (as shown in the Fig. 2.1), revealing the distribution pattern of these gabbro within the linear zone. In the mesoscopic scale, the gabbro is melanocratic, medium-grained, equigranular and shows interlocking texture. The rocks typically exhibit a massive nature, and some portions show a clear igneous texture comprising predominantly pyroxene, feldspar, and amphibole. However, in many parts, the gabbro rocks are variably deformed and display distinct foliation with a steep easterly dip (as illustrated in the Fig. 2.5 a). Stereographic analysis of the foliation within the gabbro reveals an average orientation of 40°→83°E, as depicted in Fig. 2.5 b. This orientation aligns with the regional trend of the SDFB and PSZ, respectively. To further understand the deformation, the aspect ratio of feldspar clasts in both the XZ and YZ sections was measured. The plots provide evidence of stretching, as illustrated in Fig. 2.5 c. Additionally, strain analysis was performed on the feldspar grains in the gabbro using the Flinn diagram. First, the finite strain ellipse was

determined using the Fry method (Fry, 1979). Then, these strain data were plotted on the Flinn diagram (Flinn, 1962). The resulting strain analysis plot indicates a flattening type of deformation for the gabbro, as shown in Fig. 2.5 d.

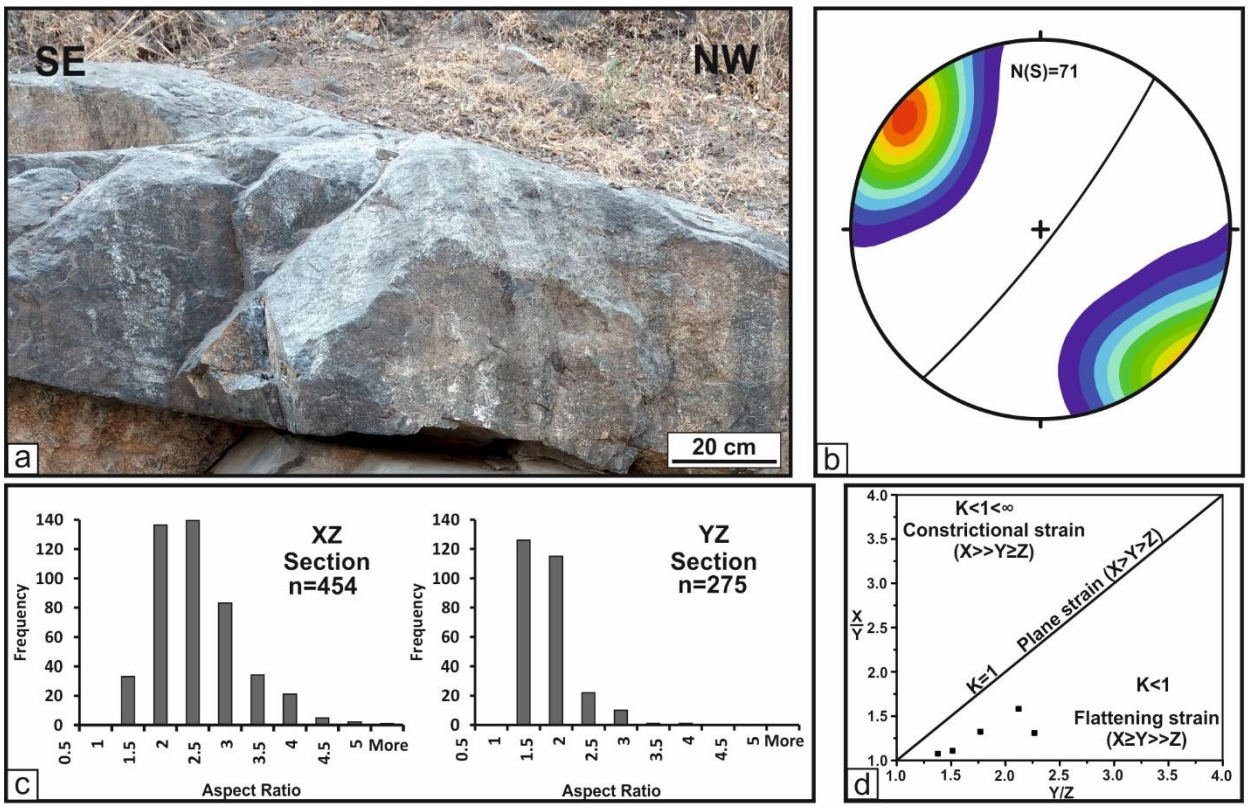

Fig. 2.5. Field photographs showing (a) Gabbro shows prominent development of foliation with steep dip, (b) The stereographic plot of the foliation in granite show a mean orientation of 40°/83°E (c) Histograms showing the aspect ratio of feldsper grains in the gabbro in the XZ and YZ sections. (d) Flinn diagram shows the flattening type of deformation in the gabbro. n = number of data. n(S) = Foliation data.

2.4: Field Relations and Deformational Patterns of the Granites

The gabbro rocks in the SDFB are always associated with pink-coloured granitic rocks (Fig 2.3 c). The granite rocks within the SDFB exhibit a distinctive pink colouration and possess a medium-grained, equigranular texture. Comprising predominantly quartz, feldspar, amphibole, and biotite, these granites can be traced along a narrow linear zone spanning over 200 kilometres within the SDFB, as illustrated in Fig. 2.2. During the course of the study (see Fig. 2.2), detailed mapping was conducted, shedding light on their distribution within this linear

zone. At the mesoscopic scale, these granitoids display a pronounced development of foliation with a steep easterly dip, as depicted in Fig. 2.6a. This orientation of the granite foliation aligns with the axial traces of the regional F2 folds within the SDFB and the mylonites of the PSZ. Furthermore, the granites exhibit a significant development of a down-dip mineral lineation, defined by the preferred orientation of micaceous minerals, amphiboles, and stretched quartz and feldspar, as illustrated in Fig. 2.6b. Stereographic analysis of the foliation within the granites reveals an average orientation of 30°→87°E, while the lineations exhibit an average principal direction of 64°→229°, as depicted in Fig. 2.6c. The aspect ratio of feldspar clasts in both the XZ and YZ sections provides evidence of stretching, as illustrated in Fig. 2.6d. To gain further insight into the deformation, strain analysis was conducted on the matrix quartz using the Flinn diagram. Initially, the finite strain ellipse was determined by employing the Fry method (Fry, 1979). Subsequently, these strain data were plotted on the Flinn diagram (Flinn,

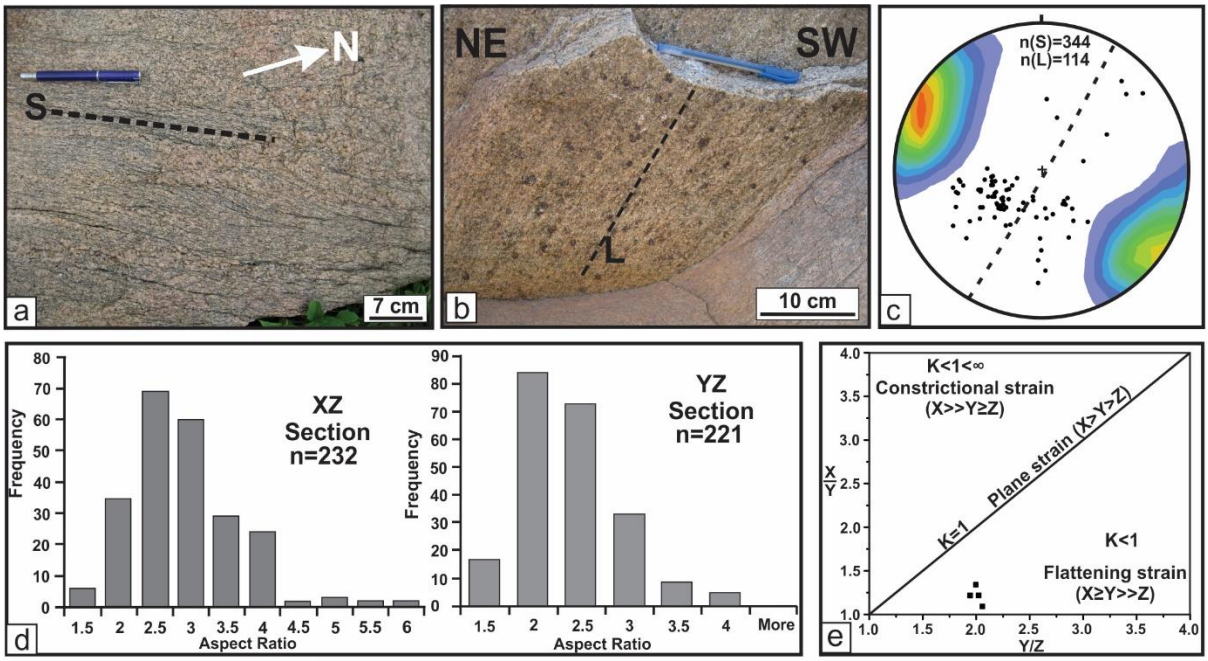

Fig. 2.6. Field photographs showing (a) Granitoids show prominent development of foliation with steep dip, (b) Showing strictly down dip mineral lineation defined by preferred orientation of micaceous minerals, amphiboles and stretched quartz and feldspars. (c) The stereographic plot of the foliation in granite show a mean orientation of 30°/87°E and the lineation show mean principal direction being 64°→229°, (d) Histograms showing the aspect ratio of quartz grains in the granites in the XZ and YZ sections. (e) Flinn diagram shows the flattening type of deformation in the granites. n = number of data. n(S) = Foliation data, n(L) =Lineation data.

1962). The strain analysis plot indicates a flattening type deformation for the granite, as presented in Fig. 2.6 e.

2.5 Summary:

The foliation of the gabbro and granite is parallel to the regional trend of the SDFB. The development of foliation and lineation in both the granite and gabbro displays a geometry and style similar to the structural elements of the mylonitic foliation found in the PSZ. Therefore, similarity in field relations suggests that the foliation in the gabbro, granite, of the SDFB, and mylonites in the shear zone rocks all formed under the same stress conditions, implying that the deformation in these units is broadly synchronous.

Chapter 3

Petrography, mineral chemistry and P-T calculation

3.1: Introduction:

This study involved an extensive microstructural examination of both gabbro and granite samples, utilizing transmitted and reflected light microscopy techniques. The analysis was conducted on over 100 oriented thin sections. Subsequent sections of this chapter delve into the sample preparation process, provide insights into the detailed microstructures, and conduct. The chapter concludes with a comprehensive discussion of the findings.

3.2: Sampling and Analytical Methods:

To facilitate laboratory investigations, over 100 thin sections were prepared. These thin sections were meticulously crafted by making cuts perpendicular to the foliation and parallel to the lineation (referred to as XZ sections), as well as cuts perpendicular to both the foliation and lineation (referred to as YZ sections). The petrographic study was conducted with observations on these thin sections using a high-resolution optical microscope, specifically the Leica DM750P model. To document our findings, photomicrographs of the thin sections were captured with the aid of standard image analysis software, namely LAS Image Analyzer (Version 4.13.0, 2017).

Electron probe microanalysis (EPMA) was conducted on the silicate and oxide minerals present in the gabbro and granite samples. Electron probe micro-analysis was carried out with a 4-WDS CAMECA SX-100 EPMA in the Department of Science and Technology, India – sponsored National Facility in the Department of Geology and Geophysics, Indian Institute of Technology, Kharagpur, India. The operating conditions for silicate minerals and X-ray mapping were an accelerating voltage of 15 kV, beam current of 20 nA and beam size of 1 μm using natural mineral standards. ZAF matrix corrections were made based on the factory-supplied PAPSIL program. For rare earth element (REE) analysis, the operating conditions

were an accelerating voltage of 20 kV, beam current of 50 nA and beam size of 1 μm. Mineral abbreviations are after Whitney & Evans (2010).

3.3: Gabbro Petrography:

The present study compiles the petrological evolutionary history of gabbroic rock. In this section, a summary of petrographic analysis results is presented based on transmitted light microscopy of ~50 thin sections prepared from different gabbroic bodies all along the SDFB. The rocks show a holocrystalline, medium-grained (phaneritic) texture. The crystals form an interlocking texture with a subhedral shape (Fig 3.1 a, b). The rock contains 55% pyroxene and 45% plagioclase. The gabbro contains clinopyroxene (cpx), orthopyroxene (opx), plagioclase feldspar, magnetite (and occasionally ilmenite) as primary mineral phases, along with amphibole, garnet, and titanite as secondary mineral phases and zircon as accessory minerals. These rocks show ophitic to sub-ophitic texture and contain several minerals as their constituents. Plagioclase laths are partially enclosed by pyroxene grains suggesting a lower nucleation rate of clinopyroxene compared to plagioclase. The secondary minerals in the

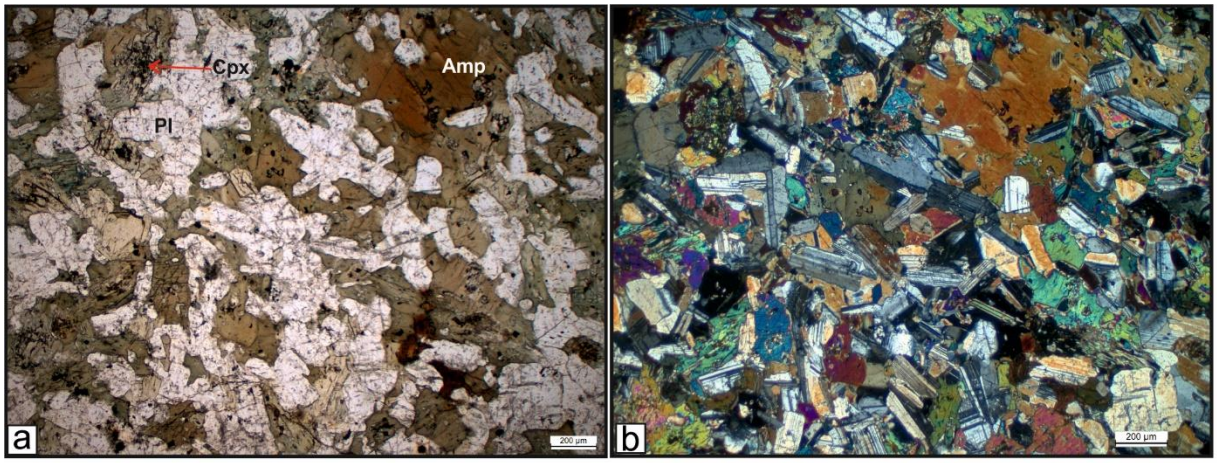

Fig. 3.1. Photomicrographs showing Igneous texture (interlocking) in gabbro defined by haphazard orientation of plagioclase, amphibole and relict clinopyroxene grains in PPL (a), and in CPL (b). PPL= Plane polarized light, CPL= Cross polarized light.

gabbro are amphibole (such as ferro-hornblende, mg-hornblende, edenite, actinolite, pargasite, and tschermakite) and garnet, which have replaced- the original igneous phases. Additionally,

titanite occurs as a corona texture surrounding the ilmenite (Fig. 3.5 a, b). In some gabbro, a noticeable foliation has developed, characterized by the preferred orientation of amphibole minerals and elongated feldspar grains (Fig 3.2 a, b). These rocks often exhibit

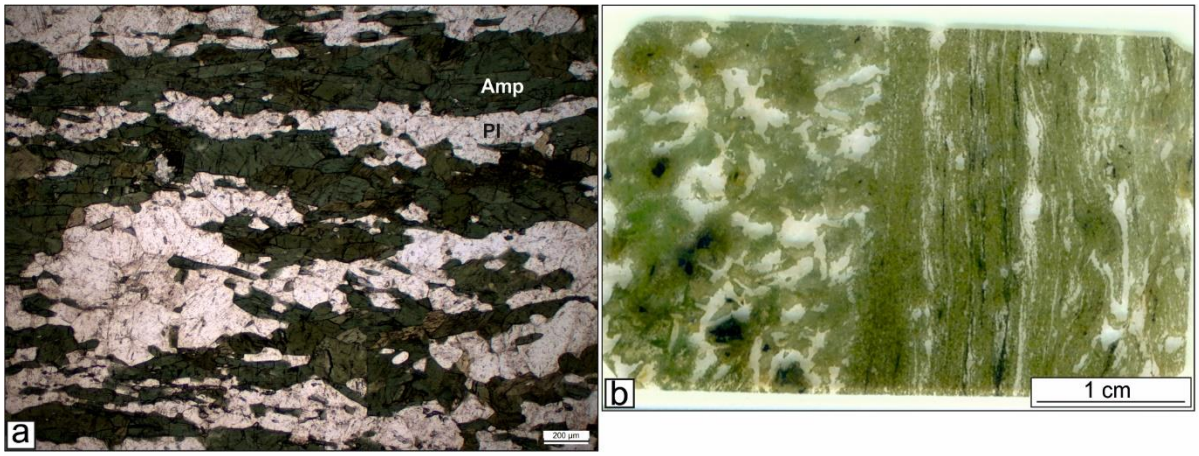

Fig. 3.2. Photomicrographs showing prominent development of foliation defined by preferred orientation of amphibole (Amp) and plagioclase (Pl) grains in PPL (a), and the scanned thin section displays a transition from magmatic texture at the left side, characterized by haphazard orientation of amphibole and plagioclase, to a deformed, foliated variety at the right side (b). PPL= Plane polarized light.

reaction textures, indicating the replacement of primary minerals by secondary minerals, which is a common feature in the deformed gabbroic rocks. In some cases, the minerals contain fractures. The primary minerals of these rocks were replaced by distinct secondary minerals (s): amphibole (Amp), titanite (Ttn), garnet (Grt), and quartz (Qz). Amphibole engulfed the Opx/Cpx grains (Fig 3.3, 3.4). Garnet also formed at the contact of Opx and plagioclase (Fig 3.3 d-f). Titanite coronae formed around the ilmenite grains in most of the samples (Fig 3.5).

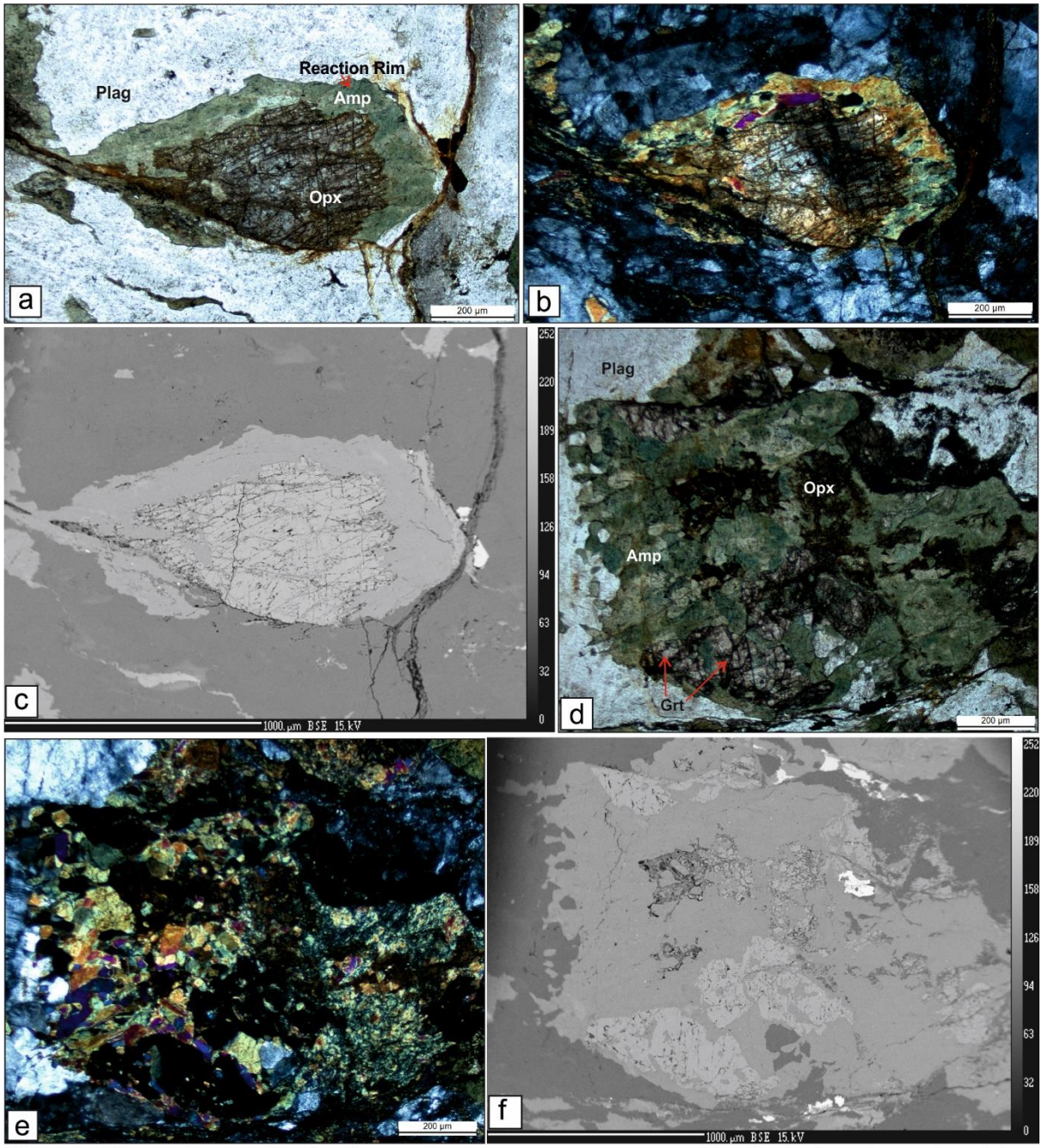

Fig. 3.3. Photomicrograph showing orthopyroxene at contact with plagioclase is replaced by amphibole in PPL (a), CPL (b) BSE (c). Photomicrograph showing orthopyroxene at contact with plagioclase is replaced by garnet and amphibole in PPL (d), CPL (e) BSE (f). PPL= Plane polarized light, CPL= Cross polarized light. BSE= Back scattered electron.

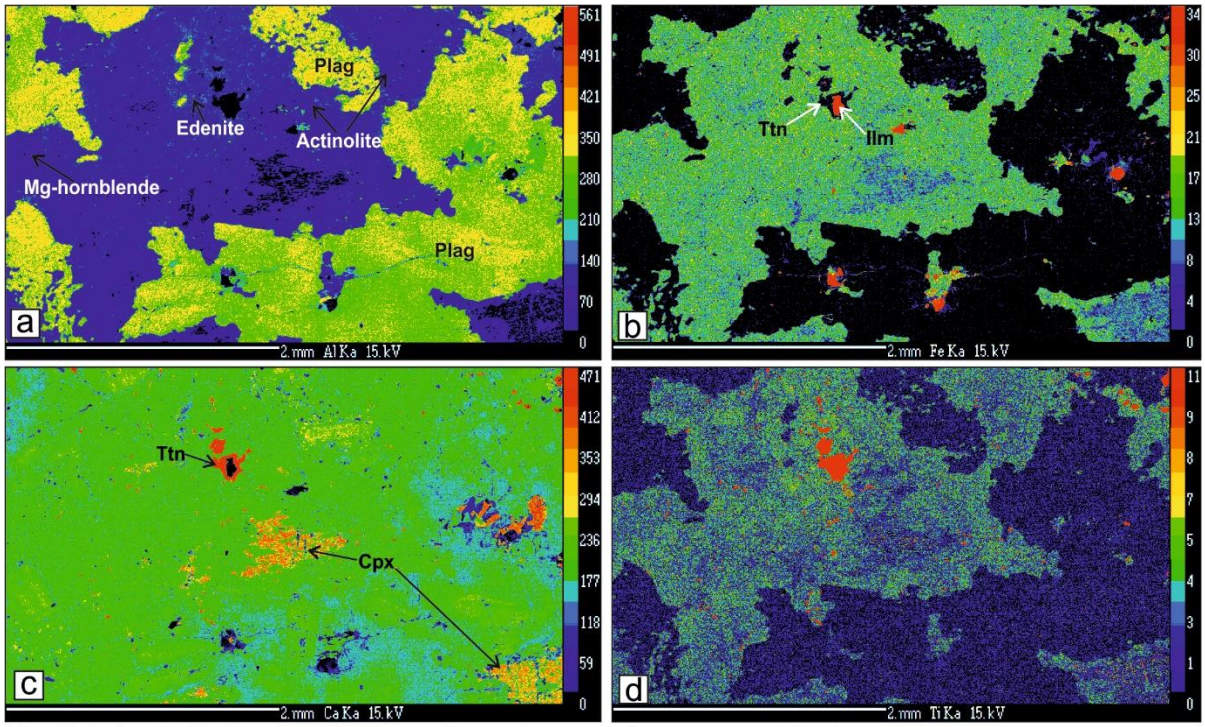

Fig. 3.4. (a–d) Al, Fe, Ca, Ti, X-ray element maps showing amphiboles replace clinopyroxene and plagioclase and titanite corona formed around ilmenite grain.

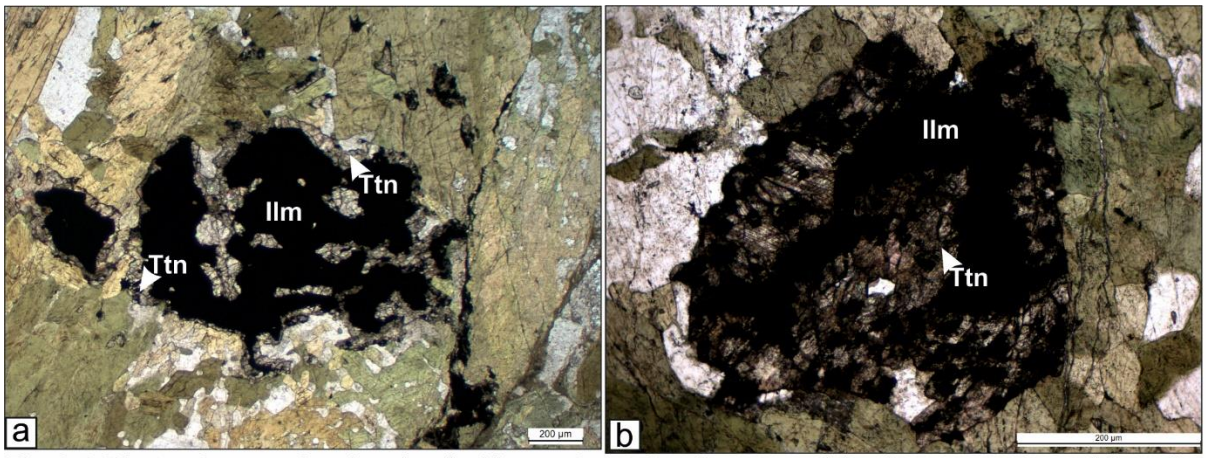

Fig. 3.5. Photomicrographs showing (a, b) prominent development of titanite corona around ilmenite in PPL. PPL= Plane polarized light.

3.4: Gabbro Mineral Chemistry:

Feldspar: The sample contains both plagioclase feldspar and orthoclase feldspar. The XCa (Ca/Ca+Na) values predominantly range from 50% to 80%, while the XNa (Na/Ca+Na) values are mainly within the range of 20% to 50%. As a result, the albite component is less abundant compared to the anorthite component in the plagioclase feldspar.

Clinopyroxene: The clinopyroxene mineral identified is predominantly diopside (98%).

Orthopyroxene: The enstatite content ranges from 34% to 35.6%, Ferrosilite content ranges from 62.3% to 64.3%, and Wo content ranges from 0.83 to 3%.

Amphibole: Following Leake et al. (2004), the amphiboles were classified into Group 2, where (Ca + Na) varies between 2 to 2.3 and Na> 0.50, classifying them into the calcic group. The Ca_A content is less than 0.5, and the Si in the formula ranges between 6.5 to 7.8, thus narrowing down most of the amphiboles as hornblende. The $Mg/(Mg+Fe^{2+})$ values determine the amphibole species as magnetio-hornblende to ferro-hornblende.

3.5: Granite petrography:

This section presents a summary of the petrographic analysis results based on transmitted light microscopy of ~70 thin sections. The petrological evolutionary history of the granitic rocks was carried out from all granite plutons along the SDFB. The medium-grained granites contain quartz, feldspar, amphibole, biotite, epidote, magnetite (± ilmenite) and garnet with allanite, titanite and zircon as accessory minerals. Quartz, feldspar (both plagioclase and k-feldspar), amphibole, biotite, magnetite (with exsolved ilmenite phases), allanite and titanite occur as magmatic minerals and garnet, epidote, as well as some biotite and titanite as metamorphic minerals replacing the igneous phases. The granites show prominent development of solid-state foliation defined by the preferred orientation of amphibole and biotite grains (Fig. 3.6 a) along with stretched quartz and feldspar grains (Fig. 3.6 b) and elongated magnetite. Amphibole is replaced by epidote+titanite+ quartz symplectite (Figs. 3.6c, 3.7, 3.8). This replacement is a very common feature in these rocks. This symplectite typically forms along the foliation-parallel faces of amphibole (Figs. 3.6c, 3.7, 3.8). This specific directional preference of this assemblage in terms of their occurrence is observed throughout the rock. In some instances, amphibole is replaced by fine biotite grains, while epidote+titanite+quartz symplectite is less

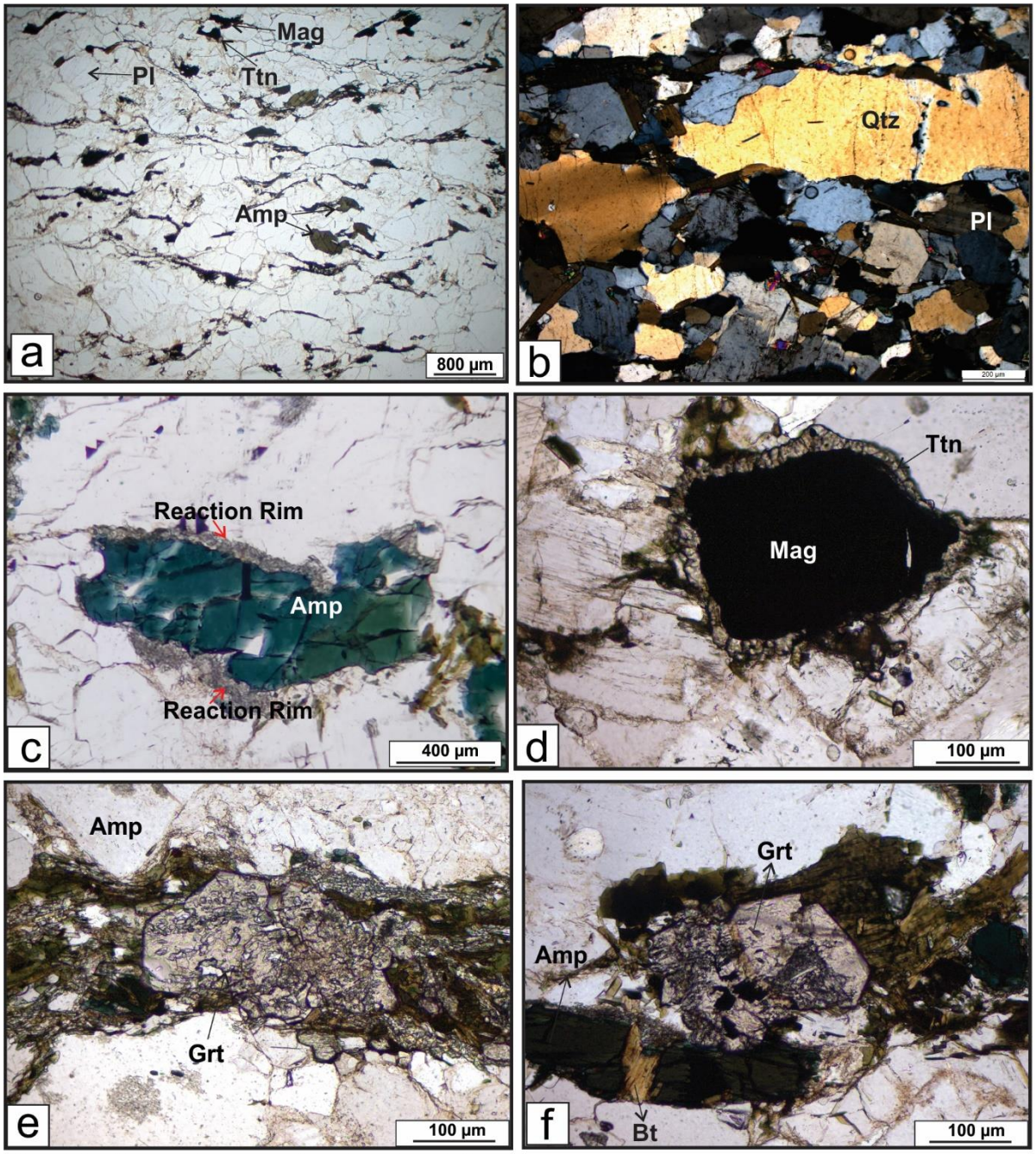

Fig. 3.6. Photomicrographs showing (a) prominent development of foliation defined by preferred orientation of amphibole and biotite grains along in PPL,(b) stretched quartz and feldspar grains in CPL, (c) Amphibole at contact with plagioclase is replaced by epidote+titanite+quartz symplectite in PPl, (d) secondary titanite forms corona texture around magnetite in PPL, (e) & (f) Euhedral garnets with epidote, quartz, titanite, magnetite as included minerals overprint the amphibole and biotite in PPL. PPL= Plane polarized light, CPL= Cross polarized light.

common. Magnetite grains with ilmenite exsolutions (Fig. 3.9c) show the occurrence of coronal titanite (Fig. 3.6d). In certain cases, euhedral titanite grains form thick coronas around magnetite with or without ilmenite. Some magnetite grains do not exhibit any titanite corona.

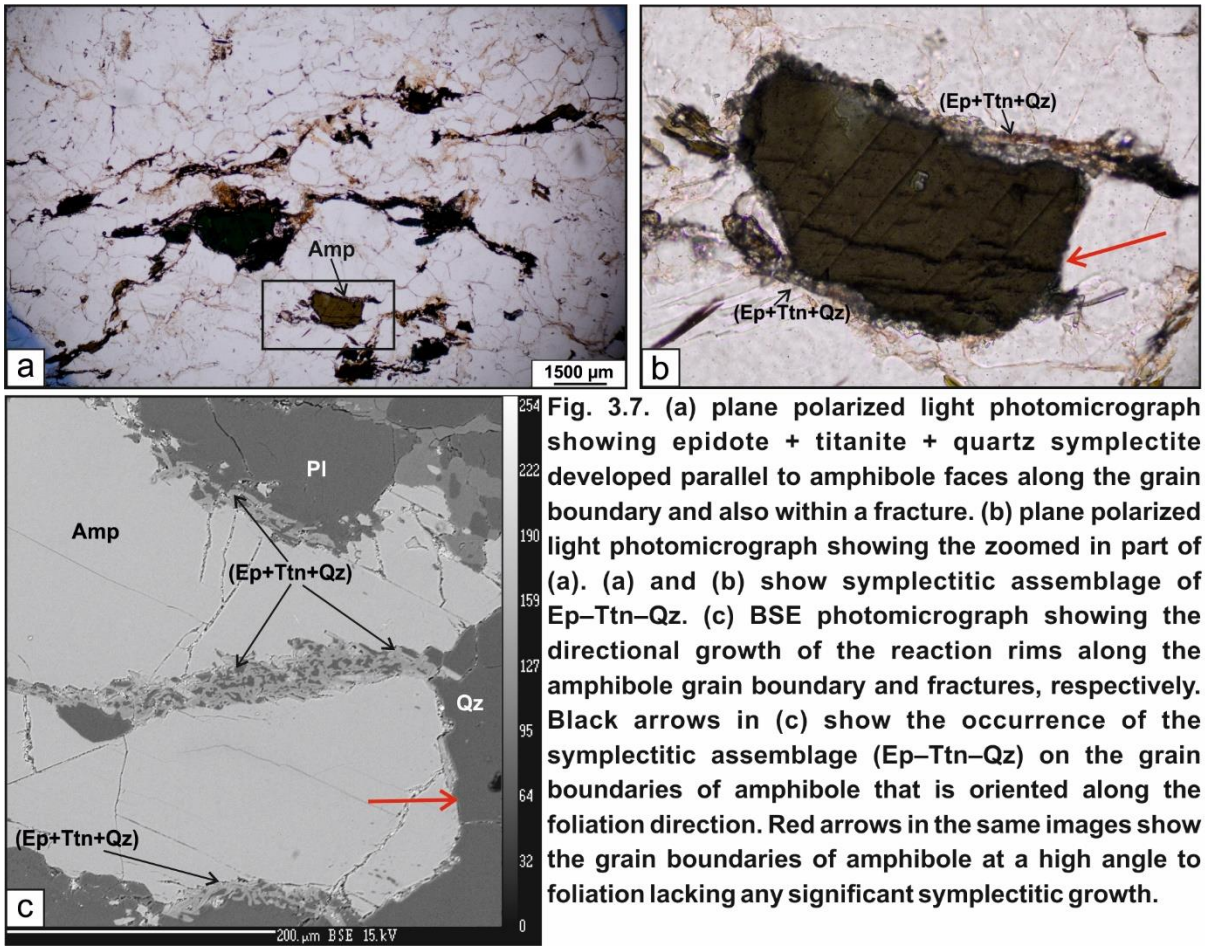

Fig. 3.7. (a) plane polarized light photomicrograph showing epidote + titanite + quartz symplectite developed parallel to amphibole faces along the grain boundary and also within a fracture. (b) plane polarized light photomicrograph showing the zoomed in part of (a). (a) and (b) show symplectitic assemblage of Ep–Ttn–Qz. (c) BSE photomicrograph showing the directional growth of the reaction rims along the amphibole grain boundary and fractures, respectively. Black arrows in (c) show the occurrence of the symplectitic assemblage (Ep–Ttn–Qz) on the grain boundaries of amphibole that is oriented along the foliation direction. Red arrows in the same images show the grain boundaries of amphibole at a high angle to foliation lacking any significant symplectitic growth.

Euhedral garnets with epidote, quartz, titanite, and magnetite as included minerals overprint the amphibole and biotite, defining the regional foliation (Figs. 3.6 e, f). Euhedral garnet grains are found to overprint foliation-defining oriented amphibole (Figs. 3.6 e, f). Though both garnet and the Ep–Ttn–Qz assemblage replace the same mineral, no essential correlation in their occurrence has been observed. The Ep–Ttn–Qz assemblage is found to replace amphibole both in the presence and in the absence of garnet, and vice versa. If they are found in the same domain, Ep–Ttn–Qz is found as inclusions within garnet, and the pattern of the included assemblage continues at the rim of the amphibole adjacent to the host garnet grain (Figs. 3.9 a, b). Textural studies demonstrate an initial igneous assemblage of quartz + feldspar + amphibole + biotite + magnetite + ilmenite + allanite + titanite + zircon, which was followed successively by the formation of epidote-titanite-quartz symplectitic coronas around amphibole grains, and

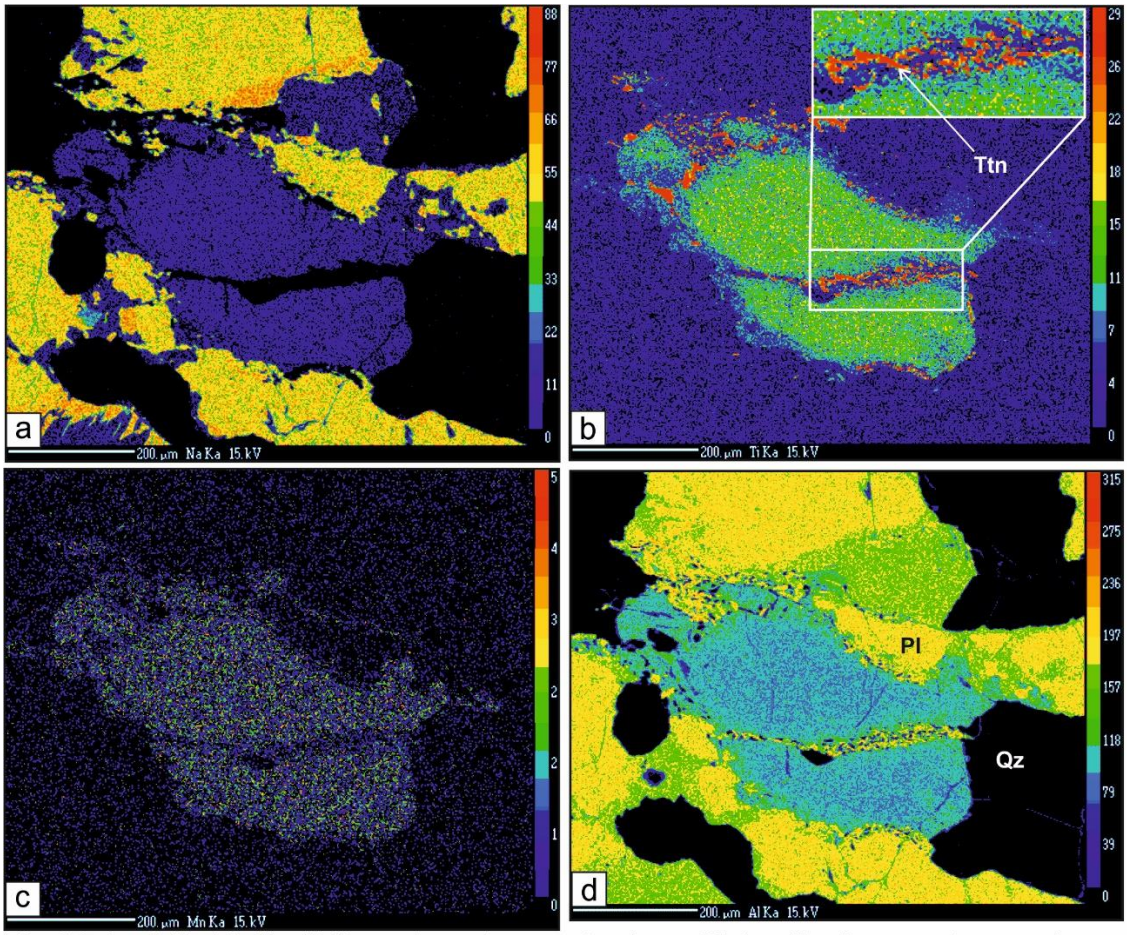

Fig. 3.8. (a–d) Na, Ti, Mn, Al X-ray element maps showing epidote + titanite + quartz occurring as symplectite within a fracture and along the amphibole grain boundary. Inset in (b) shows the zoomed in part marked with a white box.

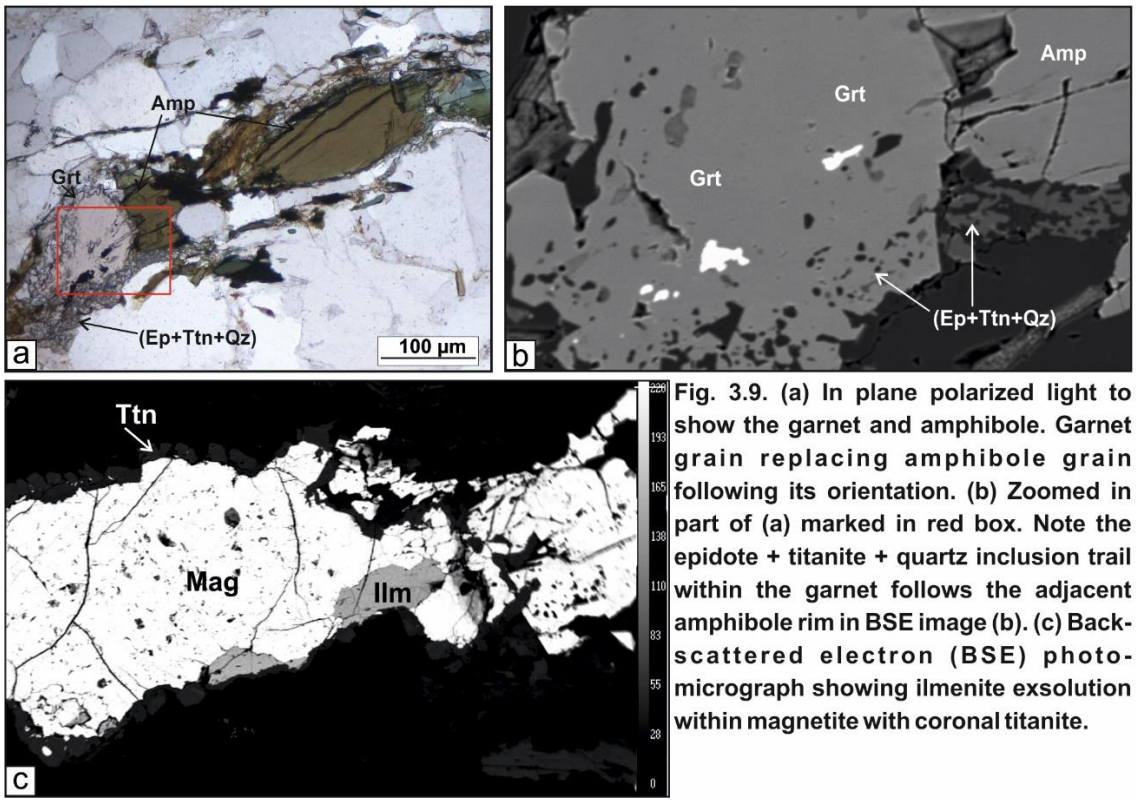

Fig. 3.9. (a) In plane polarized light to show the garnet and amphibole. Garnet grain replacing amphibole grain following its orientation. (b) Zoomed in part of (a) marked in red box. Note the epidote + titanite + quartz inclusion trail within the garnet follows the adjacent amphibole rim in BSE image (b). (c) Back-scattered electron (BSE) photo-micrograph showing ilmenite exsolution within magnetite with coronal titanite.

titanite coronas mantling magnetite and euhedral garnet overprinting the dominant foliation. This sequence of textural evolution is similar in all the studied granite plutons.

3.6: Granite Mineral Chemistry:

Feldspar: X_{Ca} (Ca/Ca+Na) values vary dominantly between 1% and 15%, with few in the range of 30% to 36%. Thus, the albite component is greater than that of the anorthite component in plagioclase feldspar. K-feldspar is present in small amounts.

Amphibole: Following Leake et al. (2004), the amphiboles were classified into Group 2, where (Ca + Na) varies between 2 to 2.3 and Na< 0.50, classifying them into the calcic group. The Ti content is less than 0.2, and the Si in the formula ranges between 5.97 and 6.22, thus narrowing down most of the amphiboles as ferropargasite. The Mg/ ($Mg+Fe^{2+}$) values determine the amphibole species as ferropargasite and hastingsite.

Biotite: The biotite grains present in the samples display high FeO content (>25 wt%) and TiO_2 (>1 wt%). X_{Fe} (Fe^{2+}/ (Fe^{2+}+Mg)) is in the range of 0.72-0.94. According to the mica classification, all of them fall approximately midway between the Fe-rich siderophyllite and annite end-members.

3.7: Reaction modelling:

Mass balance equations were modelled to investigate the adjustment of chemical constituents between reactants and products during the formation of the different replacement textures. Gain/loss of components (if occurred), as suggested by the equations, were used to understand the role of mobile components during the reaction. The balanced equation was formulated by applying singular value decomposition (SVD), a matrix factorization method in linear algebra. The software program C Space has been used (Torres-Roldan et al. 2000) for this purpose. This technique has been proven to be a robust method for modelling metamorphic textures (Lang &

Rice, 1985; Lang et al. 2004; Sengupta et al. 2009; Chowdhury et al. 2013; Banerjee et al. 2019; Adak & Dutta, 2021). SVD tests the linear dependencies and offers a number of possible mass balance equations considering a matrix composed of minerals (x) in terms of chemical components (y) while modelling reaction textures (details of the SVD method have been described by Chowdhury et al. 2013). The representative equations are chosen by the users on the basis of their observation and interpretation of the natural system. In modelling mineral reactions, the fundamental selection criteria are that the equation should contain reactant and product phases (as predicted from textural relationships) on the opposite sides of the equation (Chowdhury et al. 2013).

Here the 'x' parameter of the studied matrix is defined by phases and mobile species. The compositions have been expressed as system components that define the 'y' parameter of the matrix used for calculation (y). The rationales for choosing appropriate equation(s) representing the observed reaction relationships have been discussed individually for the replacement textures. Reaction volume change ($\Delta Vs = \Sigma Vproduct - \Sigma Vreactant)/\Sigma Vreactant) \times 100$) was calculated using the molar volume of the phases. Molar volumes for the phases were determined using the thermodynamic dataset of Holland & Powell (2011, updated in 2012) and the computer program Perple_X 6.9.1 (Connolly, 2005, updated in 2021) and the mole fraction of the end-members of each phase.

The volume proportions of the minerals from textural observations were estimated using the ImageJ software (Hu et al. 2019) Abbreviations used for the phases in the reactions are as follows: amphibole (Amp), epidote (Ep), quartz (Qz), garnet (Grt), magnetite (Mag), ilmenite (Ilm), plagioclase (Pl) and titanite (Ttn), following Whitney & Evans (2010). Parentheses after equations include the ΔV s of the reaction, and the volume proportion of reactant/product minerals and elements released or generated to form 1 mole of product.

3.7.1: Reaction modelling of the Gabbro:

Considering the textures of the replacing phases, three domains, (i) Opx, Cpx replaced by amphibole (Figs. 3.3, 3.5), (ii) garnet & amphibole both replacing the contact Opx and Plagioclase (Fig. 3.4), (iii) titanite corona on ilmenite in contact with plagioclase were identified in this rock (Figs. 3.6), and hereafter they are referred to and treated separately as three micro-reaction domains.

Table 2 represents the three separately designed matrices with the composition used from the three types of textural domains:

(i) Amphibole formation:

In the studied rocks, amphibole always occurs either around orthopyroxene or clinopyroxene rims, or completely replaced in contact with feldspar (Figs. 3.3, 3.4, 3.5). The solution offers several reactions. To understand the influence of other primary minerals, reactions were modelled with three approaches: (i) amphibole from orthopyroxene and plagioclase (Reactions 1-5), and (ii) amphibole from clinopyroxene and plagioclase (Reactions 6-9).

The matrixes are given as matrix A and matrix B in Table 2a, 2b. The solution for the matrix yielded four rational reactions having amphibole and its reactants (opx, cpx, plagioclase) on the opposite sides of the equation.

Reaction-1: 169.529Plag(11) + 7.7336Opx(14) +53.1604H2O + 6.9456 K_{1+} + 18.2317Ca_{2+} + 121.9212Fe_{3+} + 94.8223Mg_{2+} + 1Ti_{4+} = 53.1604Amph(10) + 89.9721AqSiO2 + 67.6173Na_{1+} + 135.3033 Al_{3+} (ΔVs = -17.5 %; Opx:Pl = 3:97)

Reaction-2: 29.8326Plag(11) + 179.1349Opx(14) + 46.8106H2O + 8.8632K_{1+} + 69.9552Ca_{2+} + 50.884Al_{3+} + 1Ti_{4+} = 46.8106Amph(10) + 5.2361Mn_{2+} + 118.4138AqSiO2 + 92.7873Fe_{3+} + 50.3351Mg_{2+} (ΔVs = -12.77 %; Opx:Pl = 79.5:20.5)

Reaction-3: 90.2031Plag(11) + 105.063Opx(14) + 49.5547H2O + 8.0345K_{1+} + 47.6027Ca_{2+} + 12.3954Mg_{2+} + 1Ti_{4+} = 49.5547Amph(10) + 2.9733Mn_{2+} + 106.1226AqSiO2 + 29.2212Na_{1+} + 29.5778Al_{3+} (ΔVs = -15 %; Opx:Pl = 43:57)

Reaction-4: 78.274Plag(11) + 119.6994Opx(14) + 49.0125H2O + 8.1982K_{1+} + 52.0195Ca_{2+} + 1Ti_{4+} = 49.0125Amph(10) + 3.4204Mn_{2+} + 108.5513AqSiO2 + 23.4471Na_{1+} + 18.3345Fe_{3+} + 13.6788Al_{3+} (ΔVs = -14.6 %; Opx:Pl = 49.5:50.5)

Reaction-5: 68.0109Plag(11) + 132.2919Opx(14) + 48.5459H2O+ 8.3391K_{1+} + 55.8195Ca_{2+} + 1Ti_{4+} = 48.5459Amph(10) + 3.8051Mn_{2+} + 110.6408AqSiO2 + 18.4794Na_{1+} + 34.1087Fe_{3+} + 10.6644Mg_{2+} (ΔVs = -14.2 %; Opx:Pl = 55.5:44.5)

The equations showing amphibole formation demonstrate that the Opx:Pl volume proportion can vary significantly in the reaction. Reaction 1 suggests that amphibole can be formed from low Opx concentration (Opx:Pl = 3:97), Reaction 2 suggests that Opx:Pl in the reaction requires a 79.5:20.5 ratio, and Reactions 3-5 suggest that Opx:Pl in the reaction requires 43-55.5:57-44.5 ratios. Textural attributes demonstrate that the Opx domain is always rimmed by amphibole.

Considering this relationship, the role of Opx as a reactant becomes obvious. Therefore, the reaction yielding insignificant Opx compared to plagioclase (Reactions 1) is found not to be suitable for explaining the observed texture. Reactions 2 to 5 were chosen as representative

equations out of the five reactions (Reactions 2–5) modelled for amphibole formation. These reactions show a negative ΔVs.

Reaction-6: 22.5026Plag(17) + 39.8132Cpx(1) + 18.213H2O + 1.2763K_{1+} + 23.2076Fe_{3+} + 23.4501Mg_{2+} + 1Ti_{4+} = 17.213Amph(15) + 9.2559Na_{1+} + 11.0936Ca_{2+} + 9.225Al_{3+} (ΔVs = -0.03 %; Cpx:Pl = 52.5:47.5)

Reaction-7: 16.0009Plag(17) + 49.8358Cpx(1)+ 18.3701H2O + 1.3007K_{1+} + 20.691Fe_{3+} + 16.5228Mg_{2+} + 1Ti_{4+} = 17.Amph(15) + 2.2544AqSiO2 + 6.0545Na_{1+} + 16.7557Ca_{2+} (ΔVs = -0.02 %; Cpx:Pl = 66:34)

Reaction-8: 3.7049Plag(17) + 68.7905Cpx(1) + 18.6672H2O + 1.3469K_{1+} + 15.9316Fe_{3+} + 3.4218Mg_{2+} + 17.4462Al_{3+} + 1Ti_{4+} = 18.6672Amph(15) + 6.5179AqSiO2 + 27.4637Ca_{2+} (ΔVs = 6 %; Cpx:Pl = 92:8)

Reaction-9: 35.2413Plag(17) + 20.176Cpx(1) + 4.417AqSiO2 + 17.9052H2O + 1.2285K_{1+} + 28.1383Fe_{3+} + 37.0228Mg_{2+} + 1Ti_{4+} = 17.9052Amph(15) + 15.5284Na_{1+} + 27.2993Al_{3+} (ΔVs = 0.07 %; Cpx:Pl = 26.5:73.5)

In the case of amphibole replacing the Cpx, the equations to show amphibole formation demonstrate that the Cpx:Pl volume proportion can vary significantly in the reaction. Reactions 6-7 suggest that Cpx:Pl in the reaction requires 52.5-66:47.5-34 ratios with negative ΔVs, and Reactions 8 suggest that Cpx:Pl in the reaction requires mostly Cpx (Cpx:Pl: 92:8) ratio. Textural attributes demonstrate that the Cpx domain is always rimmed by amphibole.

Reactions 8 and 9 show positive ΔVs. Therefore, reactions 8-9 are found not to be suitable for explaining the observed texture. I have chosen Reactions 6 and 7 as representative equations out of the four reactions (Reactions 6–9) modelled for amphibole formation. These reactions show a negative ΔVs.

(ii) Garnet formation:

Opx has also been replaced by garnet in the studied rock. In samples, amphibole is always associated with garnet. However, to understand the influence of other primary minerals, modelling of the reactions was done by two approaches: (i) only garnet formed from Opx and Plagioclase (Reactions 10-12) and (ii) garnet and amphibole both formed from Opx and plagioclase (Reactions 13–16). The matrix is given as matrix A in Table 2a.

Reaction-10: 933. 1000Plag(11) + 1313.0407Opx(14) + 119.6832Mn_{2+} + 406.9619Fe_{3+} + 340.7617Al_{3+} = 716Grt(9) + 2336.8257AqSiO2 + 23K_{1+} + 503.3022Na_{1+} + 790.3816Mg_{2+} + 1Ti_{4+} (ΔVs = -42.7 %; Opx:Pl = 46:54)

Reaction-11: 1000Plag(11) + 2197.04Opx(14) + 144.0137Mn_{2+} + 144.7567Ca_{2+} + 906.6931Al_{3+} = 1233.2384Grt(9) + 3191.6896AqSiO2 + 23K_{1+} + 504.8522Na_{1+} + 1403.3406Mg_{2+} + 1Ti_{4+} (ΔVs = -42.2 %; Opx:Pl = 58.6:41.4)

Reaction-12: 1000Plag(11) + 780.7622 Opx(14) + 105.0331Mn_{2+} + 652.004Fe_{3+} = 753.366Grt(9) + 1822.0905AqSiO2 + 23K_{1+} + 502.369Na_{1+} + 87.1617Ca_{2+} + 421.3034Mg_{2+} + 1Ti_{4+} (ΔVs = -43.2 %; Opx:Pl = 33.5:66.5)

Reaction-13: 72.8477Plag(11) + 62.2783Opx(14) + 6.9046Mn_{2+} + 3.3113H2O + 42.1459Fe_{3+} = 51.3862Grt(9) + 3.3113Amph(10) + 131.8292AqSiO2 + 1K_{1+} + 35.5264Na_{1+} + 2.1378Ca_{2+} + 29.464Mg_{2+} (ΔVs = -40.5 %; Opx:Pl = 35.5:64.5)

Reaction-14: 113.1859Plag(11) + 153.5941Opx(14) + 50.5994H2O + 7.719K_{1+} + 51.6578Ca_{2+} + 1Ti_{4+} = 25.9982Grt(9) + 50.5994Amph(10) + 175.6445AqSiO2 + 40.4801Na_{1+} + 16.9274Mg_{2+} + 11.0871Al_{3+} (ΔVs = -21.5 %; Opx:Pl = 46.6:53.4)

Reaction-15: 121.7206Plag(11) + 131.4997Opx(14) + 50.9873H2O + 7.6018K_{1+} + 46.5946Ca_{2+} + 18.4682Fe_{3+} + 1Ti_{4+} = 22.0601Grt(9) + 50.9873Amph(10) + 162.6671AqSiO2 + 44.5907Na_{1+} + 29.903Al_{3+} (ΔVs = -21 %; Opx:Pl = 41:59)

The solution for the matrix yielded four rational reactions with garnet and its reactants (Opx, plagioclase) on the opposite sides of the equation. The equations to show garnet formation demonstrate that the Opx:Pl volume proportion can vary significantly in the reaction. Reactions 10–12 require a varying ratio of 33.5-58.6: 66.5-41.4, and Reactions 13-15 require a varying ratio of 35.5-46.6: 53.3-64.5. Textural attributes demonstrate that the garnet domain always contains amphibole.

Therefore, reactions yielding only garnet and garnet with amphibole are found to be suitable for explaining the observed texture. I have chosen all the Reactions as representative equations out of the six reactions (Reactions 10–15) modelled for garnet formation. These reactions show a negative ΔVs.

(iii) Titanite corona formation:

Titanite coronas grow on ilmenite and girdle it (Figs 3.6 a, b)**.** The titanite corona-forming reactions were modelled considering ilmenite + plagioclase as a reactant. The solution yields an equation with ilmenite and titanite on the opposite side.

Reaction-16: 147.7149Plag(17) + 3.7021Ilm(8) + 77.1621Ca_{2+} + 138.7446Ti_{4+} = 149.4956Spn(9) + 222.6736AqSiO2 + 1K_{1+} + 77.7398Na_{1+} + 2.5059Fe_{3+} + 209.2958Al_{3+} (ΔVs = -44.4 %; Ilm:Pl = 0.8:99.2)

Reaction-17: 142.4994Plag(17) + 223.4186Ilm(8) + 295.533Ca_{2+} + 123.094Ti_{4+} = 362.0502Spn(9) + 1K_{1+} + 74.9813Na_{1+} + 205.2069Fe_{3+} + 4.9969Mg_{2+} + 195.7301Al_{3+} (ΔVs = -5.7 %; Ilm:Pl = 33:67)

Reaction-18: 67.2484Plag(17) + 3393.5597Ilm(8) + 3212.8064AqSiO2 + 3446.2595Ca_{2+} = 3428.8559Spn(9) + 1K_{1+} + 35.1814Na_{1+} + 3129.8438Fe_{3+} + 77.0944Mg_{2+} + 102.7183Ti_{4+} (ΔVs = 67.7 %; Ilm:Pl = 94:6)

Reaction-19: 101.4788Plag(17) + 1951.5149Ilm(8) + 1751.3539AqSiO2 + 2013.0461Ca_{2+} = 2033.8166Spn(9) + 1K_{1+} + 53.2857Na_{1+} + 1799.4748Fe_{3+} + 44.2984Mg_{2+} + 89.0344Al_{3+} (ΔVs = 57.8 %; Ilm:Pl = 85.5:14.5)

Matrix C contains ilmenite, plagioclase and titanite minerals along with the other mobile species (Table 2c) as the ‘x’ parameter. The solution yields four equations having plagioclase + ilmenite and titanite on the opposite side. The volume proportion of reactants (Ilm, Pl) to form titanite also shows variation. Calculated ΔV s of Reactions 16–17 are negative but

positive for Reactions 18–19. So, Reactions 16-17 are chosen as representative equations for explaining the observed texture.

3.7.2: Reaction modelling of the Granite:

Considering the textures of the replacing phases, three domains, (i) Ep–Ttn–Qz symplectite at amphibole rim, (ii) euhedral garnet replacing amphibole, and (iii) titanite corona on magnetite, were identified in this rock, and hereafter they are referred to and treated separately as three micro-reaction domains.

Table 2 represents the three separately designed matrices with the composition used from the three types of textural domains: (i) Ep–Ttn–Qz symplectite (matrix D), (ii) euhedral garnet (matrix E), and (iii) titanite corona (matrix F).

For each of the reaction domains, a unique matrix has been defined.

(i) Epidote–titanite–quartz symplectite:

Epidote, titanite and quartz symplectite always occur either within amphibole fractures or at amphibole rims in contact with quartz/ feldspar (Figs. 3.8, 3.9). This texture suggests amphibole was the only reactant in the symplectite-forming reaction. So, in matrix D (Table 2d) the ‘x’ parameter involves only amphibole, epidote, titanite (symplectitic) and quartz minerals, along with other mobile species. The solution of matrix A offers several reactions; the following reaction most closely matching the Ep–Ttn–Qz proportion in the symplectite (~47:35:18) was considered.

Reaction 20:15.290 Amp + 18.311 Ti_{4+} + 19.506 Ca_{2+} = 13.173 Ep + 24.697 Ttn + 31.763 Qz + 52.310 Fetotal + 5.079 Mg_{2+} + 1 Mn_{2+} + 6.397 Na_{1+} + 6.483 K_{1+} + 8.704 H2O (ΔVs = -6 %, Ep:Ttn:Qz = 46.77:34.80:18.43)

The reaction shows a negative ΔVs and an Ep–Ttn–Qz proportion of ~47:35:18.

(ii) Euhedral garnet:

In addition to Ep–Ttn–Qz symplectite, amphibole has also been replaced by euhedral garnet in the studied rock (Figs. 3.7 e, f). The two replacement assemblages do not show any systematic textural association/ relationship between them. Other than amphibole, no particular primary mineral is typically found to be associated with garnet. However, to understand the influence of other primary minerals, modelling of the reactions was done by two approaches: (i) garnet from only amphibole (Reaction 21) and (ii) garnet from amphibole and plagioclase (Reactions 22–25). The matrix is given as matrix E in Table 2e. The solution for the matrix yielded four rational reactions having garnet and its reactants (amphibole, plagioclase) on the opposite sides of the equation. The reactant amphibole (± plagioclase) in this rock does not contain any significant manganese, whereas the product garnet contains 24–29 mol % spessartine. To estimate the amount of manganese needed to form 1 mole of garnet (12 oxygen basis), the Mn/Grt ratio is indicated for each of the equations in parentheses.

Reaction 21: 10.903 Amp + 19.982 Al_{3+} + 16.108 Mn_{2+} + 3.507 Ca_{2+} + 14.775 O2 = 23.361 Grt + 1 Ti_{4+} + 17.246 Fetotal + 3.441 Mg_{2+} + 4.397 Na_{1+} + 4.576 K_{1+} + 10.903 H2O

(ΔVs = -6 %; Mn/Grt = 0.69)

Reaction 22: 11.17 Amp + 12.65 Pl + 29.84 Al_{3+} + 25.65 Mn_{2+} + 14.80 Ca_{2+} + 37.12 O2 = 36.02 Grt + 1 Ti_{4+} + 3.43 Mg_{2+} + 15.61 Na_{1+} + 4.03 K_{1+} + 11.17 H2O

(ΔVs = -0.02 %; Amp:Pl = 71:29, Mn/Grt = 0.71)

Reaction 23: 20.61 Amp + 973.74 Pl + 758.91 Al_{3+} + 1195.96 Fetotal + 1 Mg_{2+} + 734.89 Mn_{2+} + 869.54 Ca_{2+} + 4.28 K_{1+} + 1804.19 O2 = 989.37 Grt + 847.19 Na_{1+} + 20.61 H2O

(ΔVs = 15 %; Amp:Pl = 5:95, Mn/Grt = 0.74)

Reaction 24: 81.83 Amp + 3351.02 Pl + 2631.69 Al_{3+} + 4100.23 Fetotal + 2545.16 Mn_{2+} + 2995.92 Ca_{2+} + 10.64 K_{1+} + 6222.60 O2 = 3427.96 Grt + 1 Ti_{4+} + 2920.11 Na_{1+} + 81.83 H2O

(ΔVs = 15 %; Amp:Pl = 6:94, Mn/Grt = 0.74)

Reaction 25: 30.60 Amp + 930.46 Pl + 745.16 Al_{3+} + 1127.27 Fetotal + 718.33 Mn_{2+} + 834.39 Ca_{2+} + 1737.68 O2 = 968.56 Grt + 1 Ti_{4+} + 2.49 Mg_{2+} + 814.14 Na_{1+} + 30.60 H2O

(ΔVs = 14 %; Amp:Pl = 8:92, Mn/Grt = 0.74)

The equations to show garnet formation demonstrate that Amp:Pl volume proportion can vary significantly in the reaction. Reaction 2 suggests garnet can be formed from amphibole only (Amp:Pl = 100:0), Reaction 22 suggests Amp:Pl in the reaction requires a 71:29 ratio, and Reactions 23–25 indicate this ratio can be as low as 5–8:92–95. Textural attributes demonstrate that the garnet domain always contains amphibole. However, no specific choice for the other primary minerals was observed as garnet + amphibole is found near plagioclase/alkali feldspar/ quartz.

Considering this relationship, the role of amphibole as a reactant becomes obvious, but the same cannot be stated for the other primary phases. Therefore, reactions yielding insignificant amphibole compared to plagioclase (Reactions 23–25) are found not to be suitable for

explaining the observed texture. Reactions 21 and 22 were chosen as representative equations out of the five reactions (Reactions 23–25) modelled for garnet formation. These two reactions show negative ΔVs (Reaction 22 gives a negligible value for ΔVs, ~0) and suggest 0.69–0.71 moles of Mn2+ need to be added to form 1 mole of garnet (12 oxygen basis).

(ii) Titanite corona:

Titanite coronas grow on magnetite containing exsolved ilmenite. The corona contains ilmenite and plagioclase as relics and girdles the magnetite grain. This feature suggests that the three minerals were reactants for titanite formation (Fig 3.10 c).

Modelling of the titanite corona-forming reactions was done by considering magnetite + ilmenite + plagioclase as a reactant. Matrix F contains magnetite, ilmenite, plagioclase and titanite minerals along with the other mobile species (Table 2f) as the 'x' parameter. The solution yields seven equations having plagioclase + magnetite + ilmenite and titanite on the opposite side.

Reaction 26: 69810.062 Mag + 89.765 Ilm + 100 Pl = 683.430 Ttn + 239.409 Al_{3+} + 207380.765 Fetotal + 69.327 Mg_{2+} + 215.453 Mn_{2+} + 152.972 Na_{1+} + 1 K_{1+} + 138446.196 O2 (ΔVs = -99 %; Mag:Ilm = 99.91:0.09, Mag:Ilm:Pl = 99.59:0.09:0.32; Mn/Ttn = 0.32, Mag/Ttn = 102.15, Ilm/Ttn = 0.13)

Reaction 27: 79.317 Mag + 217.334 Ilm + 100 Pl + 249.327 Ca_{2+} = 279.317 Ttn + 50.326 Al_{3+} + 420.830 Fetotal + 25.822 Mn_{2+} + 85.517 Na_{1+} + 1 K_{1+} + 186.343 O2 (ΔVs = -25 %; Mag:Ilm = 34.09:65.91, Mag:Ilm:Pl = 17.43:33.71:48.86; Mn/Ttn = 0.09, Mag/Ttn = 0.28, Ilm/Ttn = 0.78)

Reaction 28: 2342.226 Mag + 240.128 Ilm + 1689.079 Pl + 3237.949 Ti_{4+} + 4204.645 Ca_{2+} = 4720.384 Ttn + 850.074 Al_{3+} + 6918.775 Fetotal + 1 Mg_{2+} + 1438.585 Na_{1+} + 16.891 K_{1+} (ΔVs = -8 %; Mag:Ilm = 93.25:6.75, Mag:Ilm:Pl = 37.38: 2.70:59.92; Mn/Ttn < 0.01, Mag/Ttn = 0.50, Ilm/ Ttn = 0.05)

Reaction 29: 79.196 Mag + 93.066 Ilm + 100 Pl + 117.346 Ti_{4+} + 249.215 Ca_{2+} = 279.196 Ttn + 50.228 Al_{3+} + 305.778 Fetotal + 9.916 Mn_{2+} + 85.269 Na_{1+} + 1 K_{1+}
(ΔVs = -7 %; Mag:Ilm = 54.66:45.34, Mag:Ilm:Pl = 21.57:17.89:60.54; Mn/Ttn = 0.04, Mag/Ttn = 0.28, Ilm/Ttn = 0.33)

Reaction 30: 958.524 Mag + 410.279 Ilm + 2482.691 Pl + 4709.454 Ti_{4+} + 1 Mg_{2+} + 6189.122 Ca_{2+} + 4846.535 O2 = 6923.906 Ttn + 1242.786 Al_{3+} + 2845.212 Fetotal + 2112.205 Na_{1+} + 24.827 K_{1+} (ΔVs = 26 %; Mag:Ilm = 76.80:23.20, Mag:Ilm:Pl = 14.16:4.28:81.56; Mn/Ttn < 0.01, Mag/Ttn = 0.14, Ilm/Ttn = 0.06)

Reaction 31: 79.145 Mag + 39.731 Ilm + 100 Pl + 167.709 Ti_{4+} + 249.167 Ca_{2+} + 79.976 O2 = 279.145 Ttn + 50.186 Al_{3+} + 256.399 Fetotal + 3.090 Mn_{2+} + 85.163 Na_{1+} + 1 K_{1+}
(ΔVs = 4 %; Mag:Ilm = 73.84:26.16, Mag:Ilm:Pl = 24.02:8.51:67.47; Mn/Ttn = 0.01, Mag/Ttn = 0.28,Ilm/Ttn = 0.14)

Reaction 32: 79.121 Mag + 15.591 Ilm + 100 Pl + 190.504 Ti_{4+} + 249.145 Ca_{2+} + 116.175 O2 = 279.121 Ttn + 50.167 Al_{3+} + 234.049 Fetotal + 85.115 Na_{1+} + 1 K_{1+}
(ΔVs = 10 %; Mag:Ilm = 87.79:12.21, Mag:Ilm:Pl = 25.32:3.52:71.15; Mn/Ttn < 0.01, Mag/Ttn = 0.28, Ilm/Ttn = 0.06)

Modelled garnet-forming reactions demonstrate that manganese is required to be added to balance the mass in the equations. In contrast, all the titanite-forming reactions release manganese, though the amount varies significantly. The volume proportion of reactants (Mag, Ilm, Pl) to form titanite also shows variation and, depending on that, the released Mn_{2+} amount ranges from 0.01 to 0.32 moles/mole of titanite. Reaction 26 suggests that 0.32 moles of Mn_{2+} can be yielded during titanite formation. Calculated ΔV s of Reactions 26–29 are negative but positive for Reactions 30–32.

3.8: Pressure-Temperature estimation:

Estimation of the temperature and pressure of the gabbro and granite through a number of conventional geothermobarometers. These are given as follows:

3.8.1: P-T estimation of Gabbro:

Two Pyroxene geothermometer:

Orthopyroxene and clinopyroxene compositions were used in the two-pyroxene geothermometer (Wood and Banno, 1973 and Wells, 1977) for the gabbro rocks. The compositions of coexisting orthopyroxene-clinopyroxene pairs were used for temperature calculations. The calculated temperature values range from 650ºC to 780ºC.

Sample No Pair Temperature	T℃ (Wood and Banno,1973)	T℃ (Wells, 1977)

Opx1-Cpx23	756°C	780°C
Opx2-Cpx24	644°C	622°C

Two Pyroxene geobarometer:

The existing barometers ranges from 10 kbar to 60 kbar and requires temperature (ranges from 900°C -1400°C) as a major component for calculating pressure. Based on the calculated low temperature range (below 900°C) and the limitation of pressure constrain of barometers, pressure of the gabbro samples could not be calculated (Brey, 1984; Brey and Kohler, 1990; Finnerty & Boyd, 1987; Nickel, 1989).

3.8.2: P-T estimation of Granite:

Al in Amphibole geobarometer:

Amphibole composition was used in the Al-in-hornblende geobarometer (Holland & Blundy, 1990; Johnson & Rutherford, 1989), which accounts for the linear variation of Al concentration in amphibole with the pressure of crystallization and the extent of post-crystallization upward movement. EPMA data of several amphibole grains were used for pressure estimation. The resulting pressure values ranged around 7 kbar ± 1 kbar, 6.7 kbar ± 0.6 kbar respectively.

Sample No	Holland & Blundy, 1990 (P in kb)	Johnson & Rutherford, 1989 (P in kb)
P-491 70 / 1	7.62	5.94
P-492 73 / 1	8.22	6.46
P-106 1 / 1	8.44	6.65

P-107 2 / 1	8.79	6.94
P-108 8 / 1	8.90	7.04
P- 225bz 6	7.55	5.88
P- 225bz 18	7.26	5.64
P- 225bz 19	9.22	7.31
P-104 68 / 1	8.69	6.86
P-245az 97/ 1	8.79	6.94
P-199 74 / 1	8.12	6.37
P-200 79 / 1	8.86	7.00
P-201 80 / 1	9.08	7.19

Plagioclase and Amphibole geothermometer:

For the hornblende–plagioclase thermometer (Holland & Blundy, 1994), temperature was determined using amphibole-plagioclase assemblages, which provides a framework to account for the composition-dependence of the ideal (mixing-on-sites) equilibrium constants. The compositions of coexisting amphibole-plagioclase pairs were used for pressure-temperature calculations. The hornblende–plagioclase thermometer yields a temperature of 700 ± 50°C (at 7 kbar). A notable contrast exists between the temperature-pressure values of the core and rim regions. It should be noted that this calibration has a reported uncertainty of ± 75ºC.

Sample No Pair	T℃ (Holland & Blundy, 1994)
225BZ Amp6–Pl3	720°C
225BZ Amp18/1–Pl25/1	678°C
225BZ Amp19/1–Pl22/1	690°C
P-491 Amp73/1–Pl8/1	658°C

P-491 Amp51/1–Pl53/1	736°C
P-491 Amp61/1–Pl63/1	709°C

3.9: Summary

The texture of the gabbro suggests the replacement of the primary minerals occurred by the formation of amphibole and garnet. The texture of the granites suggests the replacement of the primary minerals occurred in two stages. Amphibole was replaced sequentially by Ep–Ttn–Qz symplectite followed by garnet. Euhedral garnet grains and titanite corona are post-tectonic to the regional fabric, whereas the symplectite assemblage formed during deformation.

Chapter 4

Whole rock geochemistry

4.1: Introduction:

The present chapter focuses on the whole-rock geochemical characteristics of the gabbro and granite rocks of the SDFB. Specifically, fifteen samples were collected from relatively unaltered igneous gabbro and twelve samples of minimally altered granite were collected for geochemical analysis (Fig 4.1). The data obtained from major elements, minor elements, trace elements, and Rare Earth Elements (REE) were acquired using X-ray fluorescence (XRF) and inductively coupled plasma mass spectrometry (ICP-MS) techniques at the ACME Laboratory

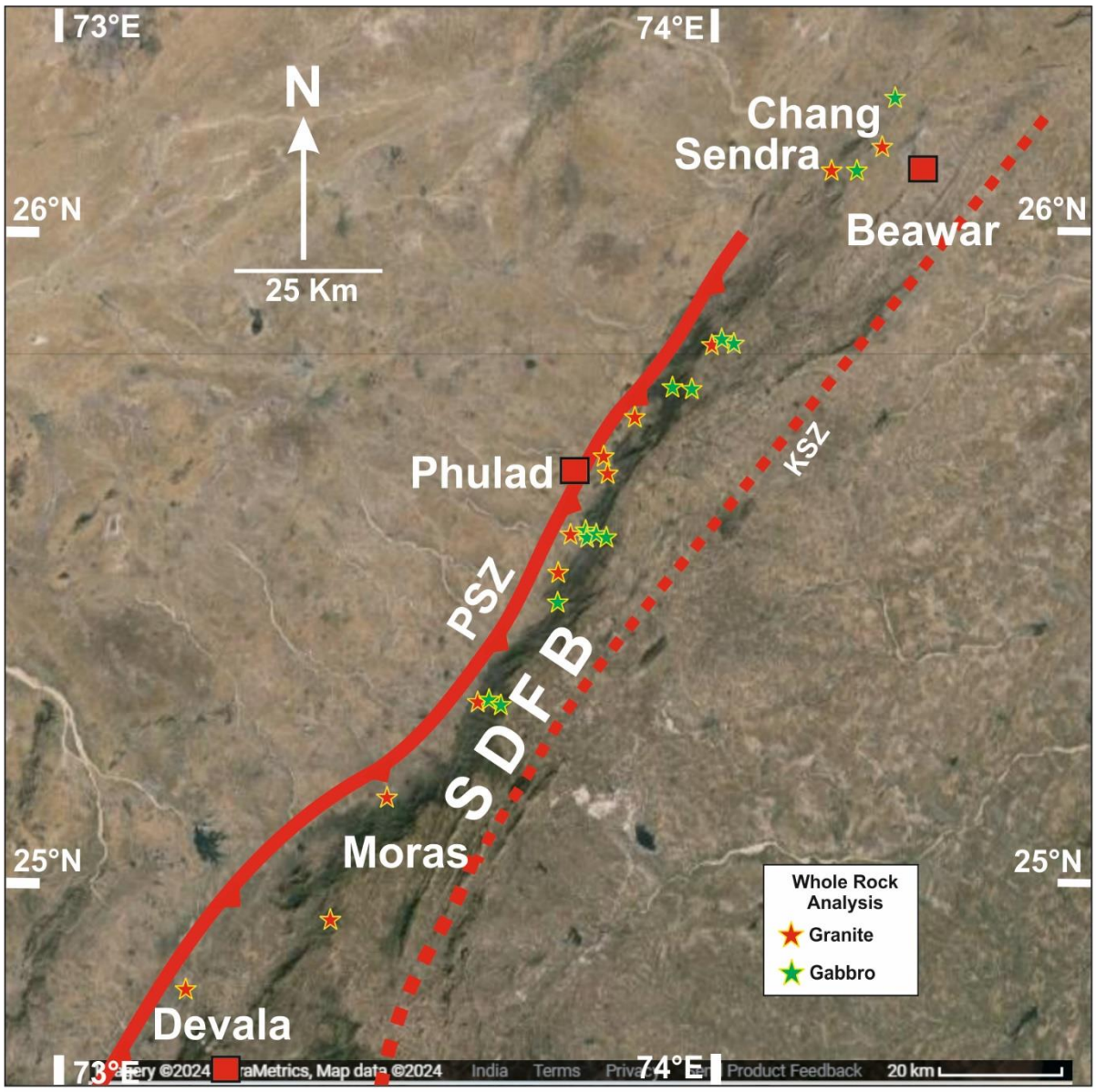

Fig. 4.1. Sample locations for whole rock analysis of the gabbro and granite rocks are shown in satellite image taken from Google imagery, map data © 2024 of the SDFB.

in Canada. The resulting analytical data are presented in Table 3 and have been used to classify the rocks and gain insights into their likely tectonic origins. The geochemical data toolkit version 3.15 (GCDKit) was employed to analyse and present this data.

4.2: Sample Preparation and Analytical Technique:

Fresh samples weighing over 5 kg were crushed using a tungsten carbide jaw crusher for the analysis. The rock samples were then dried within a temperature range of 60°C to 100°C. After cone and quartering, representative portions were finely powdered using an agate ball mill, reducing them to particles smaller than 600µm. The samples were meticulously prepared for XRF and ICP-MS analysis at the ACME Laboratory in Canada. To achieve this, the samples were digested through a process involving lithium metaborate/tetraborate fusion. This fusion method involved mixing the samples with LiBO2/Li2B4O7 flux. Following this partial digestion method, the samples were called "leaches." Partial digestion can vary in strength, from weak to moderate or strong, and in selectivity, either attacking a specific mineral substrate (selective) or all mineral substrates (non-selective). The choice of partial digestion was influenced by the mode of occurrence of the analyte, which provides insights into its source and transport. This method enhances the contrast between anomalous and background values. Two types of partial digestion were employed: water, a weak and selective leach conducted at room temperature to dissolve only water-soluble compounds like salts, and aqua regia, a strong mineral acid (HCl + HNO3) leach conducted at 95°C, liberating elements from salts, exchange sites, carbonates, oxides, hydroxides, sulphides, and more. Aqua regia was added to 0.5 g sample aliquots in test tubes before being subjected to a hot-water bath to improve digestion. For total decomposition, a method chosen to report the absolute abundance of an element or compound within the sample, we utilized the 4-acid digestion (Geochemical digestion)

approach. This involved using nitric, perchloric, and hydrofluoric acids heated until dryness to decompose most minerals, including silicates, into metal salts. These metal salts were then back-leached into either aqua regia or concentrated HCl. Subsequently, we employed ICP-MS to measure the weight percentages of major and minor elements and trace elements. Loss on ignition (LOI), which measures weight loss after igniting a sample split, was also determined. Additionally, total carbon and sulphur content were analyzed using the Leco method, which relies on the detection of atoms striking a target when solutions are aspirated into a plasma operating at 8000°C. Pure solutions of known analyte concentrations were used for calibration. Sample analysis was carried out using an Elan 6000 ICP Mass Spectrometer. The analysis covered 51 elements, including Au, Ag, Al, As, Ba, Be, Bi, C, Ca, Cd, Co, Cr, Cs, Cu, Fe, Ga, Hf, Hg, Si, Sn, Sr, Ta, Th, Ti, Tl, U, V, W, Zn, and Zr. Additionally, optional elements such as K, Mg, Mn, Mo, Na, Nb, Ni, P, Pb, Rb, S, Sb, Sc, Y, La, Ce, Pr, Nd, Sm, Eu, Gd, Tb, Dy, Ho, Er, Tm, Yb, and Lu, including the REE suite, were analyzed. The determination of sample volumes for other elements that may be subject to the nugget effect was of particular importance in this study.

4.3: Whole Rock Geochemistry of the Gabbro:

Out of fifteen samples, twelve samples are primarily classified as gabbro, one as peridotitic gabbro, and two as diorite, on a TAS ($Na_2O + K_2O$ vs. SiO_2) diagram (Middlemost, 1994) Fig. 4.2 a. The gabbro samples exhibit variable oxide contents, including low SiO_2 (47.7–51.36wt%), while the diorite samples show SiO2 content of 58-59 wt.%.

All samples have high Al_2O_3 (12.6–17 wt.%), Na_2O (1.14–3.27wt%) and K_2O (0.15–1.27 wt%) contents, with a total $Na_2O + K_2O$ content of 1.5–4 wt% ($Na_2O > K_2O$) and a low K_2O/ Na_2O ratio of 0.04–0.12. Additionally, all samples have CaO content ranging from 7.44–13.79 wt.%. Geochemical characteristics classify these 15 samples as tholeiitic in nature (Fig. 4.2 b).

The Mg# number (Mg#=100*(Mg/(Mg+Fe^{2+}) vs. major oxides diagrams (Fig. 4.2 c), theAl_2O_3,

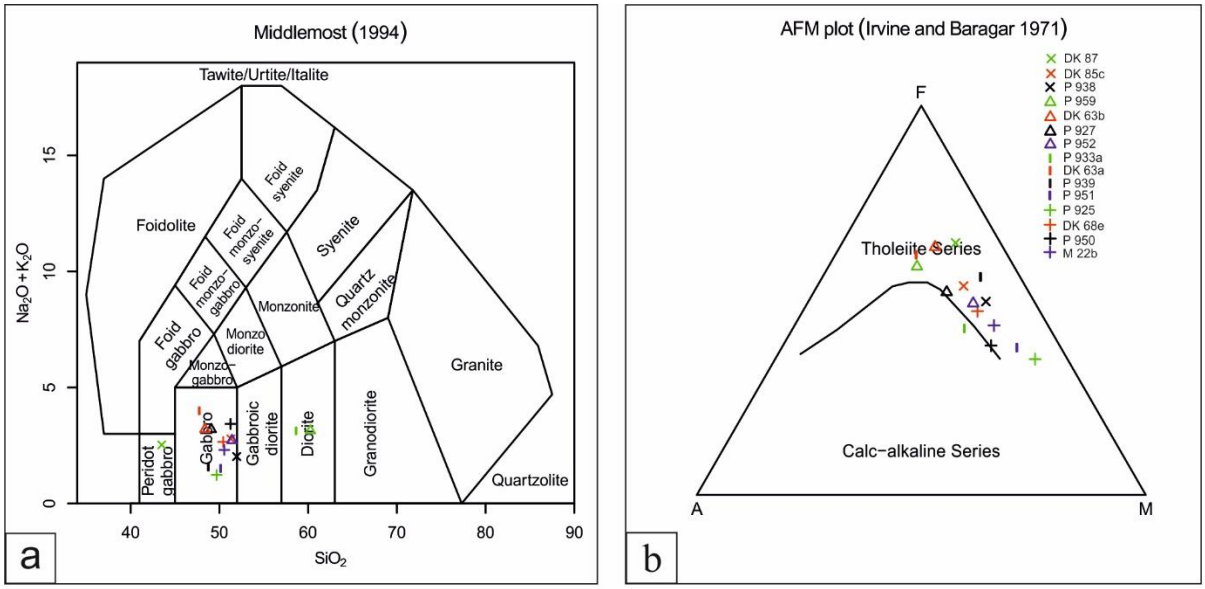

Fig. 4.2. Geochemical classification of the gabbro, (a) Na_2O+K_2O vs. SiO_2 plot (Middlemost 1994) and (b) Tholeiitic character of gabbro shown by Irvine and Baragar (1971) AFM plot.

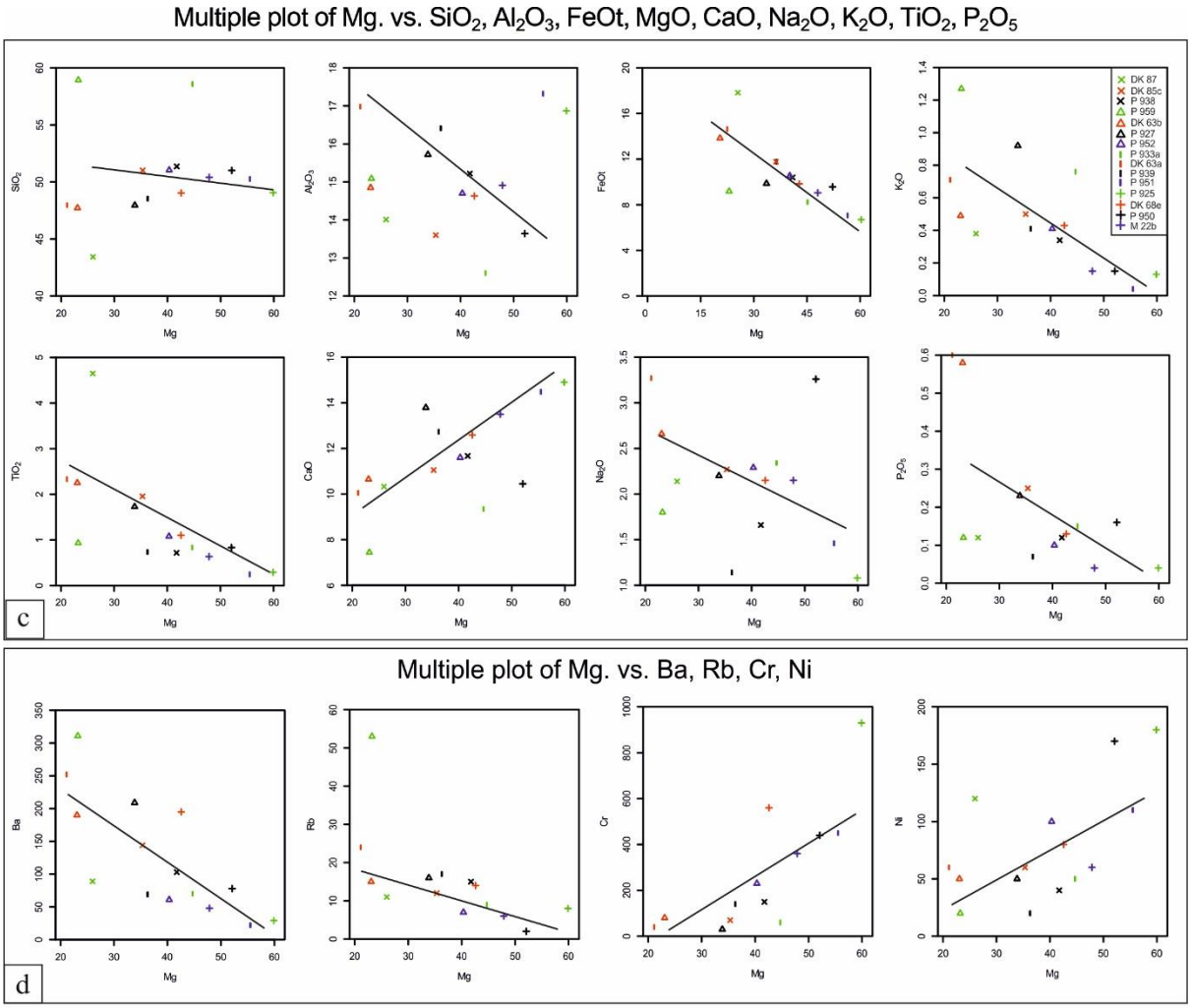

Fig. 4.2. Harkar diagrams of the gabbro, (c) major oxides and (d) trace elements.

FeO^T, K_2O, TiO_2, Na_2O and P_2O_5wt.% of the samples exhibit strong negative correlations with Mg#, while SiO_2 wt.% shows slightly increasing trend with decreasing Mg#. CaO wt.% shows a decreasing trend with decreasing Mg#. In the trace element plot, Ba and Rb contents of the samples exhibit strong negative correlations with Mg#, while Cr and Ni show a slightly positive slope with Mg# (Fig. 4.2 d).

On the Primitive mantle normalized diagram (McDonough and Sun, 1995), all samples show enrichment of incompatible elements (Fig. 4.2 e). These samples exhibit positive Rb, Ba, Th, and Sr anomalies and negative Nb, P, and Ti anomalies (Rudnik 1995, Taylor & Mclennan-1995), indicating geochemical affinity to arc-type igneous rock.

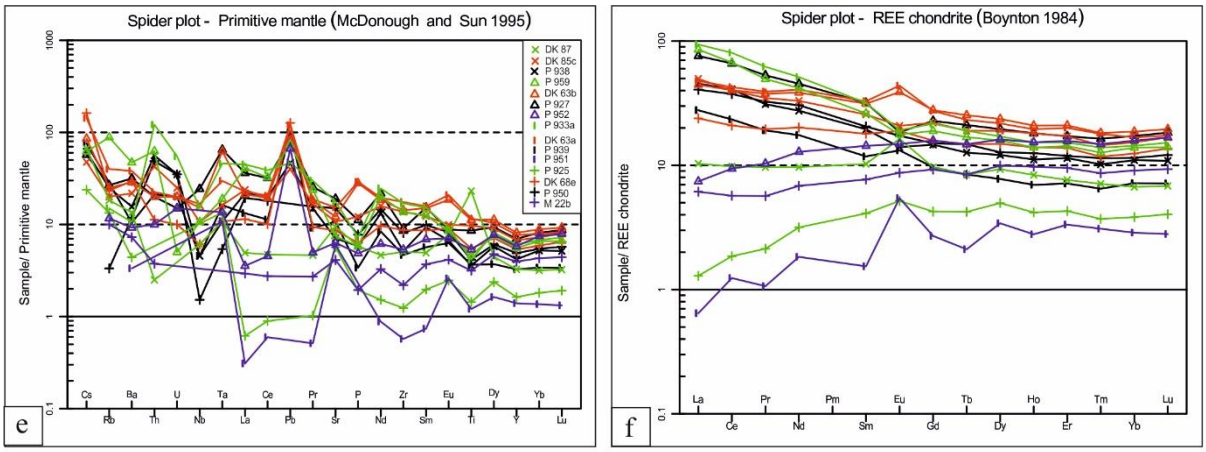

Fig. 4.2. Geochemical classification of the gabbro, (e) Primitive mantle normalized (McDonough and Sun 1995) trace element spider diagrams showing enriched levels for incompatible elements, (f) Chondrite normalized (Boynton, 1984) REE diagram, the REE distribution pattern shows flat HREE trends, whereas LREEs display a wide range of distributions. fractionation between LREEs and HREEs with slight negative to moderate positive Eu anomalies (ranges 0.69-2.67).

In a chondrite normalized (Boynton, 1984) spider diagram, the REE distribution pattern shows fractionation between LREEs and HREEs with low negative to moderate positive Eu anomalies (ranges 0.69-2.67) (Fig. 4.2 f). All the samples show flat HREE trends, whereas LREEs display a wide range of distributions. Most of the samples (Ten) show feeble right-dipping LREE distributions, two samples show left-dipping LREE distributions, and three samples show more or less flat LREE distributions. In this study, $(La/Yb)_N$ vs La(de Wall et al. 2021) and the $(La/Sm)_N$ and La(Wang et al. 2020) concentration plot of gabbro samples shows a positive slope (Fig. 4.2 g). The plot of $(La/Sm)_N$ ratios >1–3 and $(La/Yb)_N$ ratios range from 1.9–6.6

(Fig. 4.2 h). The gabbro samples plot near the spinel-peridotite melting curve, exhibiting various degrees of melting in the Dy/Yb vs. Gd/Yb diagram (Cheng et al., 2020; Tang et al., 2014) (Fig. 4.2 i). The Nb/La vs. La/Yb plot (Abdel-Rahman and Nassar 2004) displays a scatter ranging from the lithospheric mantle to the lower crust composition (Fig. 4.2 j). The

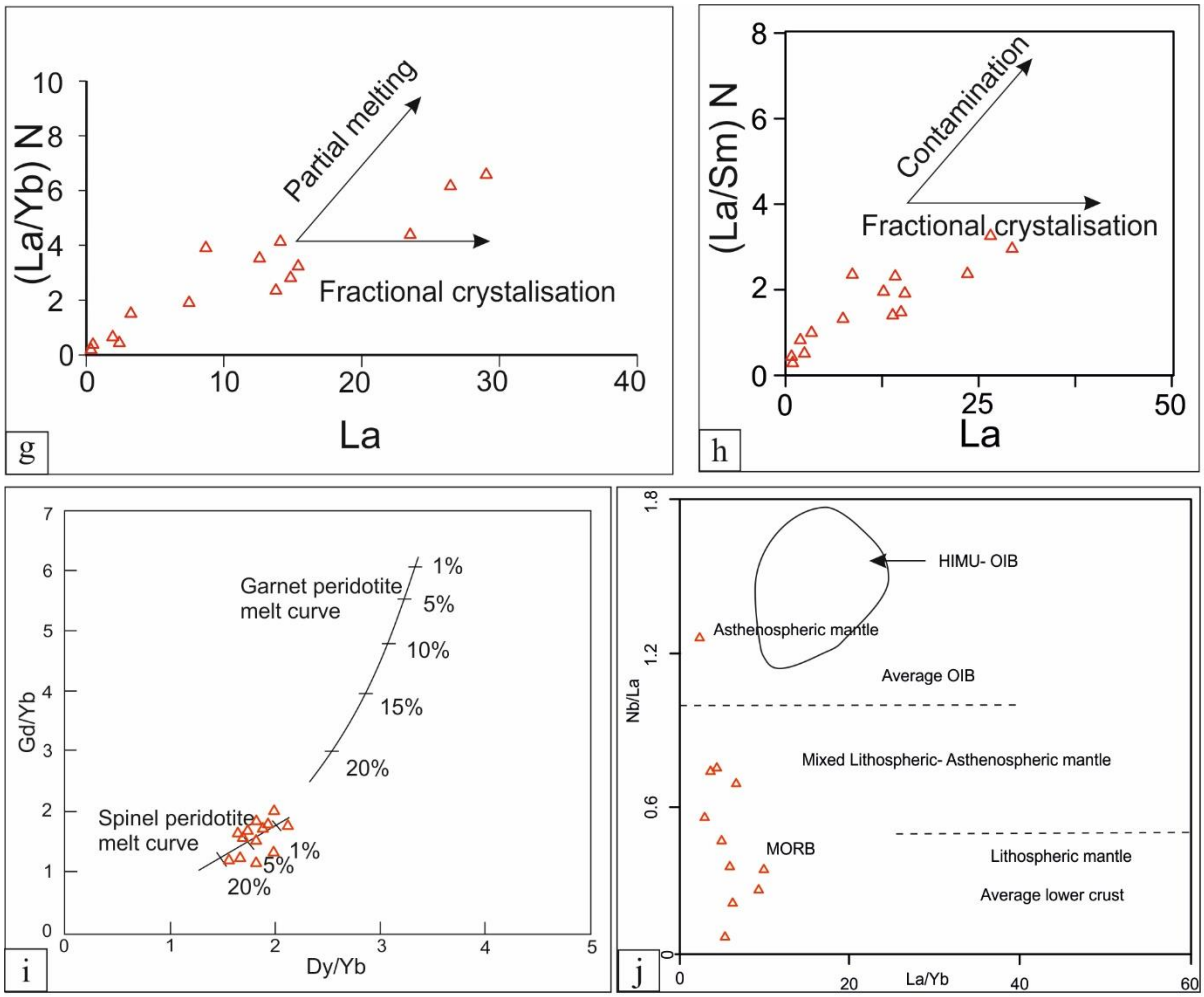

Fig. 4.2. Geochemical classification of the gabbro, (g) $(La/Yb)_N$ vs. La showing magma evolution by partial melting; (de Wall et al. 2021), (h) $(La/Sm)_N$ vs. La shows that the gabbro evolved by fractional crystallization with crustal contamination; (Wang et al. 2020) (i) Gd/Yb vs. Dy/Yb (Tang et al. 2014) showing gabbro melt generated due partial melting of spinel peridotite, (j) Nb/La vs. La/Yb plot (Abdel-Rahman and Nassar 2004) displays a scatter ranging from the lithospheric mantle to the lower crust composition.

Nb/Yb vs Th/Yb projections (Fig. 4.2 k) (Pearce, 2008) reveal a vertical trend from the E-MORB field to the volcanic arc array field, whereas the Nb/Yb vs TiO2/Yb plots reflect the E-MORB field, exhibiting a diagonal trend from OIB (Fig. 4.2 l). In the Th_N vs Nb_N discrimination plot (Saccani, 2015), most samples fall into the back arc, and a few fall into

continental margin volcanic arc fields (Fig. 4.2 m). These mafic rocks display a trend from Within Plate Baslat to MORB in the Zr/Y vs Zr plot (Pearce and Norry, 1979) (Fig. 4.2 n).

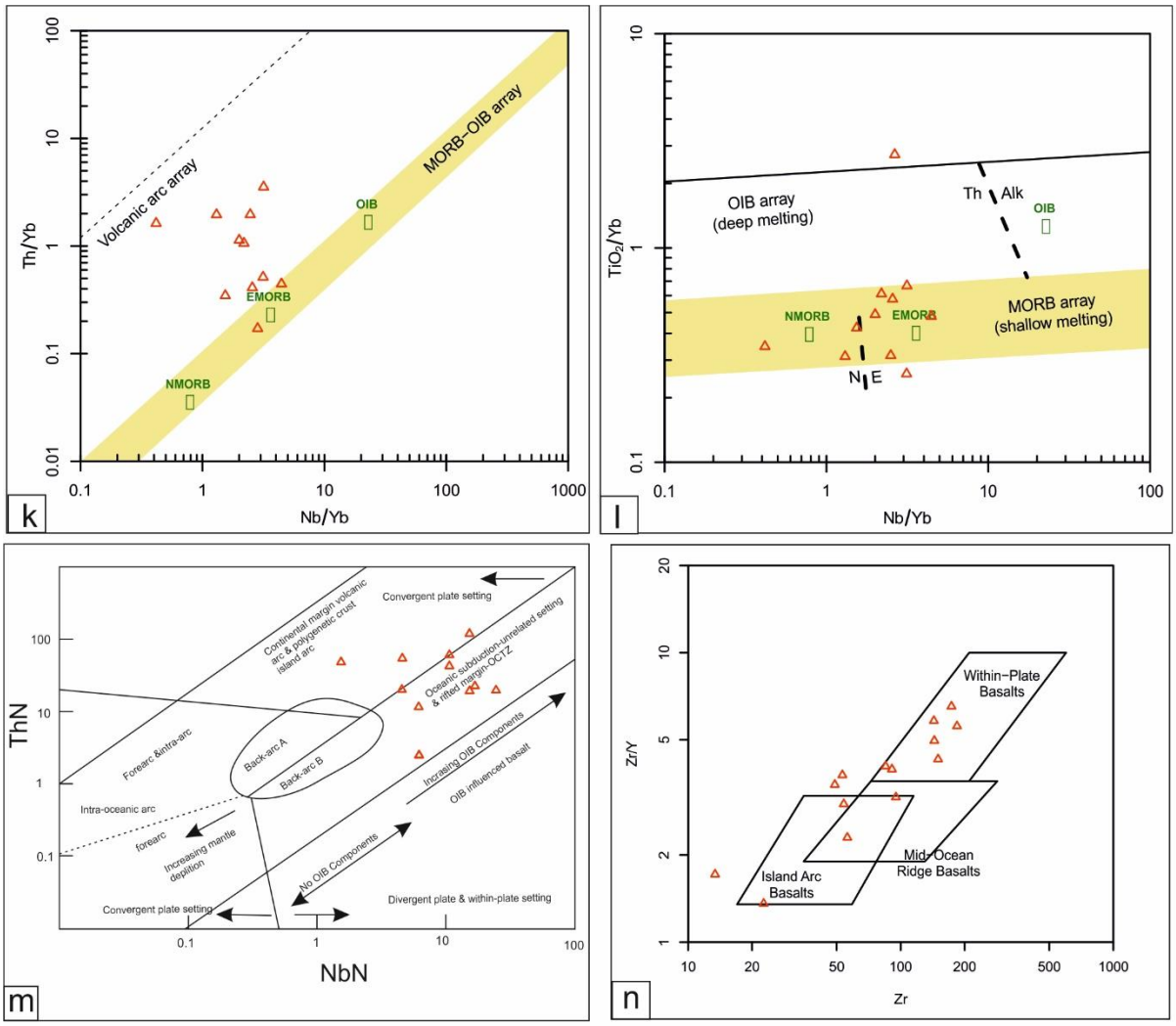

Fig. 4.2. Geochemical classification of the gabbro, (k) The Nb/Yb vs Th/Yb projections (Pearce et al., 2008) reveal a vertical trend from E-MORB field to volcanic arc array field, (l) Nb/Yb vs TiO2/Yb plots reflects the E-MORB field, exhibiting a diagonal trend from OIB (Pearce et al., 2008), (m) ThN vs NbN discrimination plot (Saccani et al., 2015) shows the back-arc affinity of the rocks, (n) Tectonic discrimination showing Within Plate Basalt affinity using the trace element (Zr vs. Zr/Y) diagrams of Pearce and Norry, (1979).

4.3.1: Magma Source and petrogenesis of the gabbro:

Geochemical analysis was conducted on spatially separated gabbro bodies. The overall geochemistry of the gabbro is tholeiitic in nature. The gabbro samples show variable MgO contents ranging from 3.7-10.3 wt.% (average 6.7) and wide Mg# values (20-60), suggesting

that the gabbro experienced a significant degree of fractional crystallization involving mafic silicates (olivine and/or pyroxene), as well as a few plagioclases and apatite. The increasing trends in SiO2, Al2O3, FeOt, K2O, TiO2, Na2O, and P2O5 wt.% with decreasing Mg# suggest that the gabbro experienced a significant differentiation process before emplacement. These trends indicate fractional crystallization involving mafic silicates such as olivine and pyroxene. This is further supported by a clear positive correlation of Cr and Ni concentrations with Mg#. Additionally, the TiO2 values (0.7-2.3 wt.%) reflect the presence of Ti-rich minerals, particularly ilmenite and titanite, in the studied rocks. The negative slope of Ba, Rb trace elements with Mg# no indicates crustal contamination. Positive anomalies of Sr, Ba in trace element spider plot (McDonough and Sun, 1995) of the gabbro samples suggest the presence of plagioclase crystallization where positive Th anomaly indicates crustal contamination. This study finds partially overlapping trace element composition ranges from N-MORB to E-MORB (Boynton 1984). The distribution of geochemical concentration is unlikely to form from the continuous evolution of a single melt. High LREE concentrations with a negative slope indicate an enriched source and a low percentage of partial melting. Flat HREE patterns with slight negative slopes indicate the presence of garnet-bearing melt residues and lower levels of fractional crystallization. For some samples, a few trace-element concentrations are below the detection limit for N-MORB samples. For these samples, elements with concentrations above the detection limit were considered. Positive anomalies of Sr, Ba, Eu and Th in the gabbro indicate plagioclase crystallization and crustal contamination, while negative Nb, P and Ti anomalies suggest the fractionation of Fe-Ti oxides and apatite.

In this study, the (La/Yb)N vs La plot suggests a fractional crystallization trend with a small component of the partial melting component during magma ascent (de Wall et al. 2021) (Fig. 4.2 g). The plot of $(La/Sm)_N$ ratios >1–3, and $(La/Yb)_N$ ratios range from 1.9–6.6 (Fig. 4.2 h). The elevated La/Sm ratio in the magma, influenced by crustal material, are commonly greater

than 3 (Lassiter and DePaolo, 1997; Bulk crust 5.1, Rudnick and Gao, 2003). Petrographic and major-element geochemical analyses suggest that fractional crystallization and accumulation processes played a significant role in the petrogenesis of the gabbro. The $(La/Sm)_N$ and La plot suggests that the gabbro shows evidence of crustal contamination or magma mingling with fractional crystallization components during magma ascent (Wang et al. 2020).

The gabbro samples plot close to the spinel-peridotite melting curve with various degrees of melting in the Dy/Yb vs. Gd/Yb diagram (Fig. 4.2 i). This suggests that the primitive magma for these rocks primarily originated from significant partial melting (5%-10%) of a spinel-bearing mantle source (Cheng et al., 2020; Tang et al., 2014). Generally, the transition from garnet to spinel in the mantle occurs at relatively shallow depths (<85 km; Robinson and Wood, 1998). Therefore, the upwelling of the asthenospheric mantle may be a plausible explanation. The Nb/La vs La/Yb plot displays a scatter spanning from the lithospheric mantle to the lower crust composition (Fig. 4.2 j), indicating that the melt was generated from a mixed lithospheric-asthenospheric mantle, with contributions from lower crustal rocks. In summary, it can be suggested that the gabbro originated from the mafic melt generated due to the partial melting of a spinel peridotites of the mantle. Fractionation crystallization is the most likely a major mechanism for the petrogenesis of the gabbro.

4.3.2: Implication for tectonic setting of the Gabbro:

The span of trace elements suggests a composition range from N-MORB to E-MORB, indicating that these melts were generated from the mantle. Flat HREE patterns in gabbro (chondrite normalized) indicate shallow-depth melting. There can be three possibilities to explain the simultaneous growth of N-MORB and E-MORB rocks (Batiza & Niu, 1992; Jansen et al., 2024; Perfit et al., 1994; Waters et al., 2011**)**.

1. The contemporaneous magmatism of N-MORB and E-MORB suggests that they originate from the melting of a heterogeneous mantle. Perfit et al. (1994) proposed that

E-MORB melts might traverse through the mush zone and intrude shortly afterwards. The significant overlap in trace element compositions between these rock units implies that they were formed during a transitional magmatic event, where the primary phase of crustal accretion was succeeded by "near-axis" magmatism (Jansen et al., 2024).

2. The second model suggests that the geochemical variations arise from mixing enriched and depleted melts during progressive depletion. E-MORB and N-MORB melt form at different times due to periodic heterogeneities in the melting region or shifts in melt transport and storage processes (Batiza & Niu, 1992).
3. E-MORB and N-MORB melts are generated concurrently and stored in a discontinuous melt lens, preventing complete melt homogenization and preserving the E-MORB composition. Periods of diminished melt production would be expected (Waters et al., 2011). Both E-MORB and N-MORB are produced and stored in the shallow mantle or crust without thorough homogenization due to physical discontinuities or melt transport systems.

In the present study, the samples are of the same age, and E-MORB compositional rocks are more prevalent than N-MORB, which contradicts the first hypothesis. Possibly, E-MORB and N-MORB form a continuum of compositions which can be explained by mixing melts derived from a heterogeneous mantle source. Elevated abundances of highly incompatible elements and a shallow HREE slope, common features of E-MORB, are attributed to the melting of spinel peridotite (Donnelly et al., 2004; Waters et al., 2011). As spreading ceases, asthenospheric upwelling and melting also diminish. Lower degrees of melting preferentially enriched mantle components. These melts produced and stored in a discontinuous melt lens, and their reduced homogenization, increases the preservation potential of the enriched compositions.

Various discrimination diagrams were utilized to explore the potential tectonic origin of the gabbro. The Th-Nb/Yb proxy indicates crustal input and non-subduction settings, while the TiO2-Nb/Yb proxy reveals melting depth, mantle temperature, and thickness of the conductive lithosphere. Nb/Yb-Th/Yb projections (Pearce, 2008) reveal melting depth, with variance on the Th/Yb axis explained by garnet residues during melting (Fig. 4.2k), while the Nb/Yb axis reflects source and melting variables. The plots display an E-MORB field with a vertical trend to the volcanic arc array, suggesting high mantle temperature and thin lithospheric units. The samples fall within the E-MORB area, indicating an extensional setting with crustal signatures. Nb/Yb vs TiO2/Yb plots predominantly fall within the E-MORB and N-MORB field, exhibiting a diagonal trend suggesting a shallow melting (Fig. 4.2l). Generally, Th and Nb have similar geochemical properties (Fig. 4.2m). However, Th becomes mobile in subduction-related magmatic processes due to the hydrous fluid's addition from the subducted slab, while Nb remains stable. To understand the tectonic setting of the gabbro, the ThN–NbN discrimination plot has been used (Saccani, 2015). In this plot, some samples fall into the back-arc and continental margin volcanic arc fields, which indicates that the magma was generated in an extensional setup. These mafic rocks display a trend from Within Plate Baslat to MORB in the Zr/Y vs Zr plot (Pearce and Norry, 1979) (Fig. 4.2 n).

4.4: Whole Rock Geochemistry of the Granite:

The granites show high SiO_2 (72-78 wt %) and low concentrations of Fe_2O_3 (<4 wt%) and MgO (<0.5 wt%). The abundance of Na_2O and K_2O individually are comparable in the range (2-5 wt%). The K_2O and Na_2O content varies from 1.58-5.26 wt% and 2.95 -5.18 wt%, respectively, with the Na2O/ K2O ratio varying from 0.56 to 3.10. MgO varies from 0.04 to 0.45 wt%, Al_2O3 from 11.67 to 13.96 wt%, CaO from 0.70 to 2.39 wt%, TiO_2 from 0.10 to 0.26 wt% and F_2O_3 from 1.32-3.27 wt%. The Na_2O+K_2O vs SiO2 plot of Middlemost (1994) shows granitic

composition (Fig. 4.3 a). The granites are geochemically classified as metaluminous to weakly peraluminous (Shand 1943) (Fig. 4.3 b) ferroan and calc-alkalic (Frost et al. 2001) (Fig. 4.3 c).

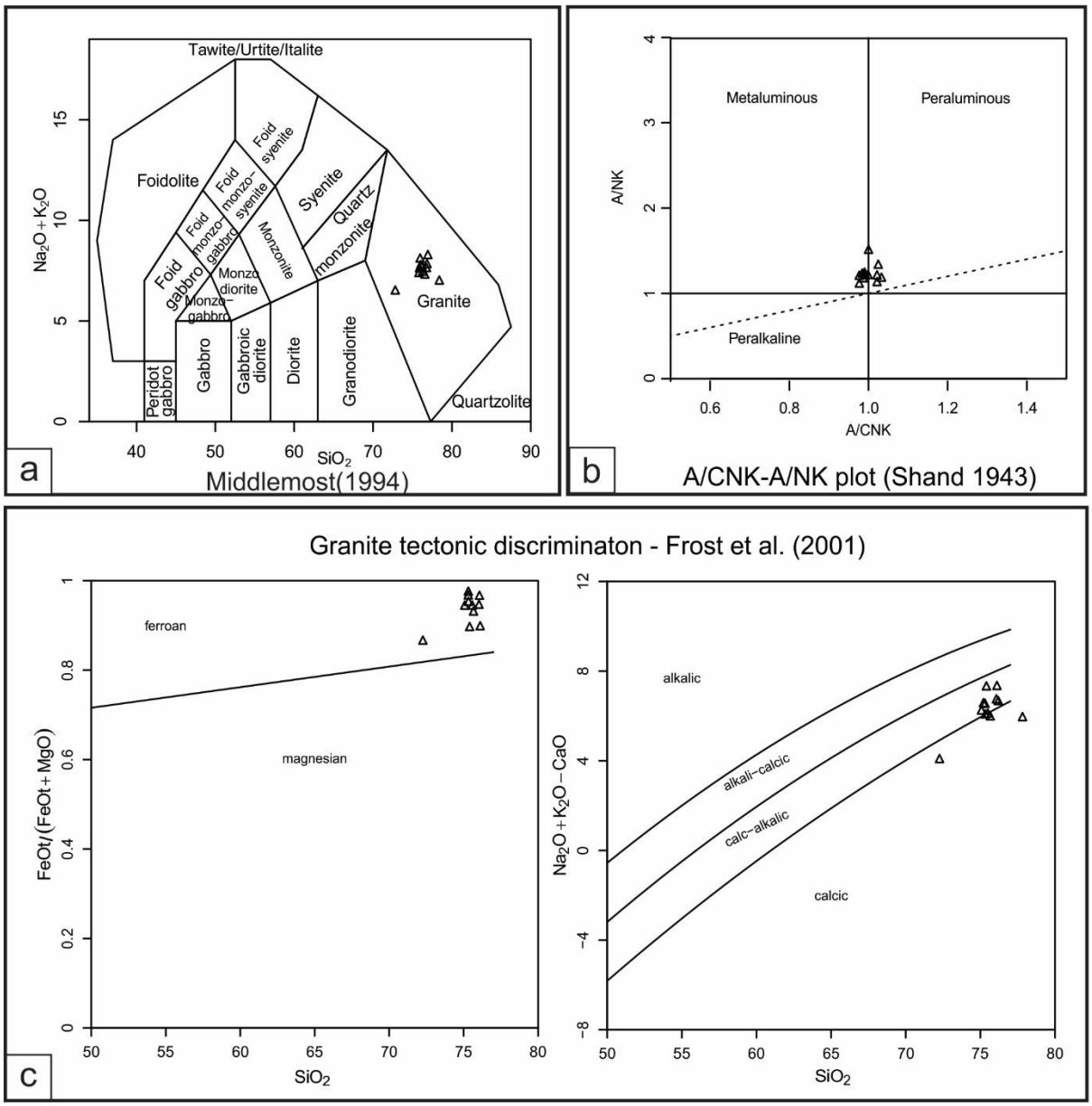

Fig. 4.3. Geochemical classification of the granites, (a) Na_2O+K_2O vs. SiO_2 plot (Middlemost 1994) and (b) Metaluminous to peraluminous character of granites shown by Shand's (1943) index, (c) Ferroan and calc-alkalic character of granites shown by Frost et al. (2001).

These granites show clusters for Al2O3, MgO, and Na2O and decreasing trends for CaO, Fe2O3, and TiO_2 with increasing SiO_2 (Fig. 4.3 d).

Primitive mantle normalized (McDonough and Sun 1995) trace element spider diagrams (Fig. 4.3 e) for the granites show enriched levels for incompatible elements. All the granite samples show pronounced negative Nb, Sr, P and Ti -anomalies and small negative Ba and Zr

anomalies. The REE chondrite normalized (Boynton, 1984) (Fig. 4.3 f) trends for these rocks show LREE enrichment and flat HREE trends for most samples. All the samples show

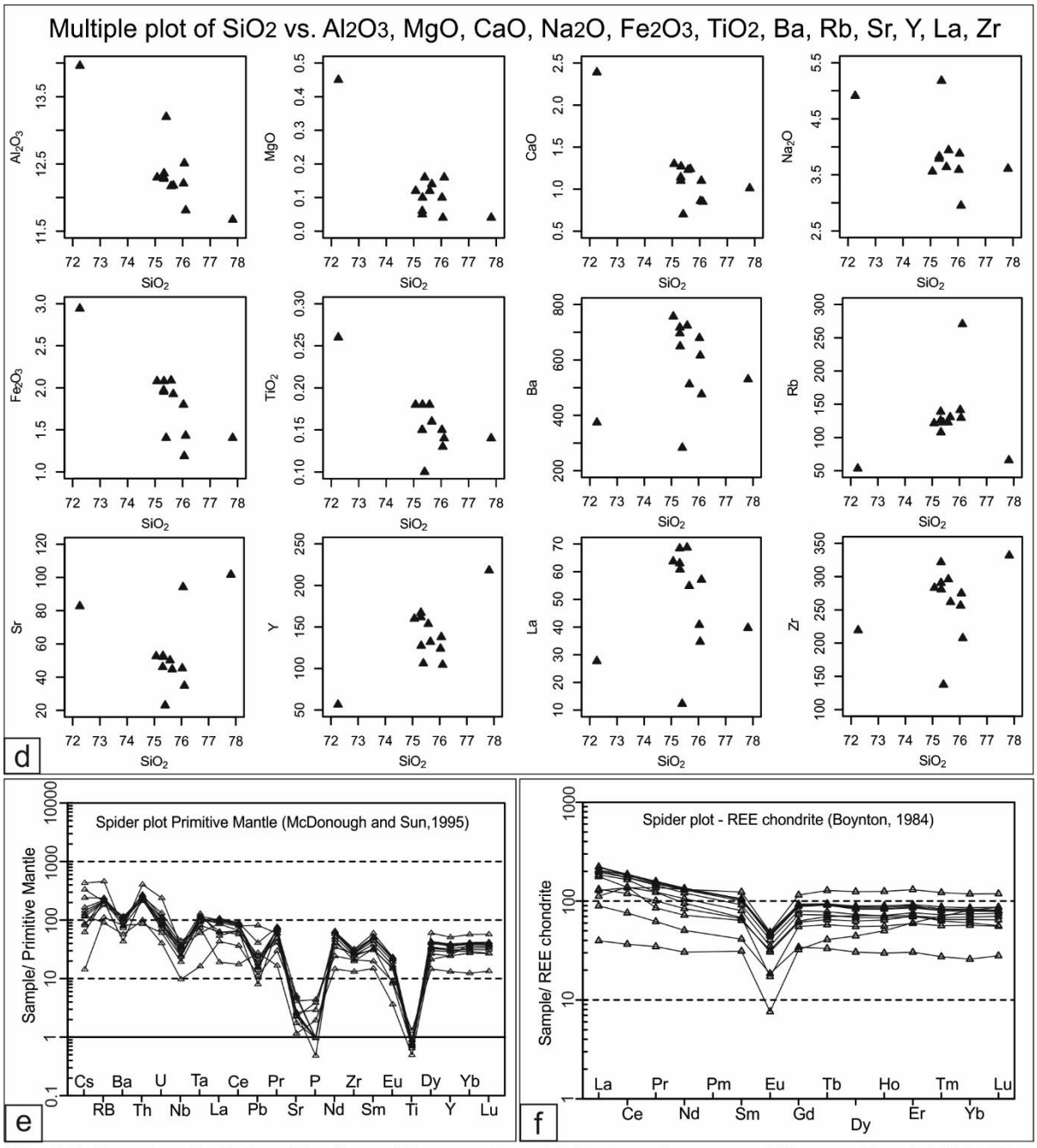

Fig. 4.3. Geochemical classification of the granites, (d) Harkar diagrams of the granites (e) Primitive mantle normalized (McDonough and Sun 1995) trace element spider diagrams showing enriched levels for incompatible elements, (f) Chondrite normalized (Boynton, 1984) REE diagram showing LREE enrichment and flat HREE trends with negative Eu anomaly.

moderate to high negative Eu anomalies [(Eu/Eu*) = 0.24-0.51]. Total REE content ranges between 130 and 450 ppm. The granites show negative correlations of Ba with varying Eu/Eu* concentration (Figs. 4.3 g). The plots of $(La/Sm)_N$ vs. La (Wang et al. 2020) and $(La-Yb)_N$ vs.

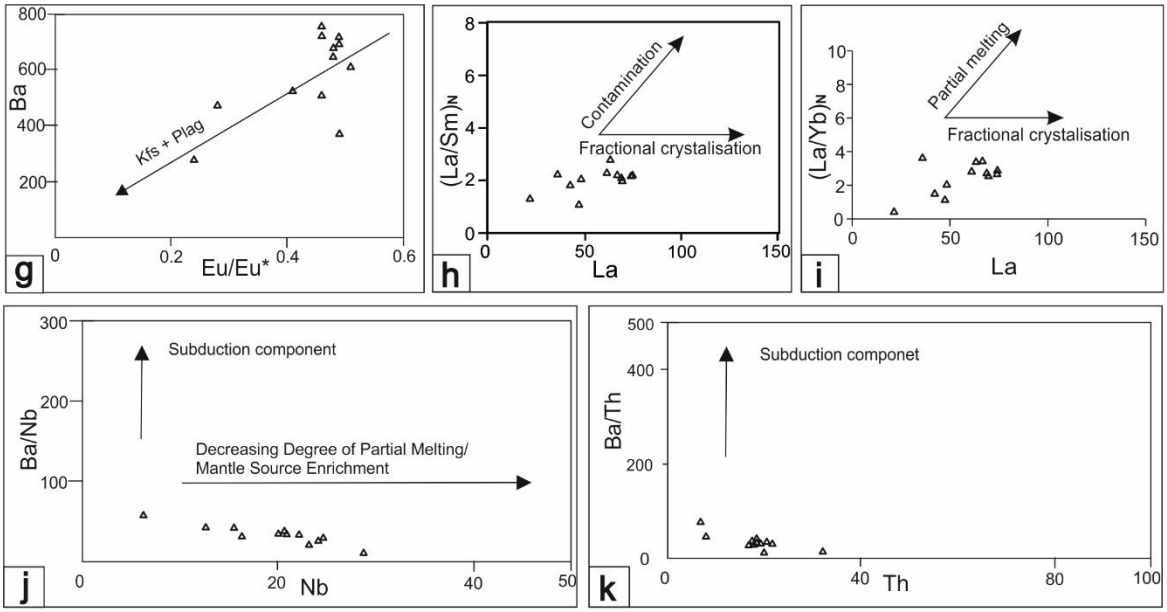

Fig. 4.3. Geochemical classification of the granites, (g) Chemical discrimination diagrams illustrating the mineral fractionation process for the granitic pluton Ba vs. Eu/Eu* (Kamaunji et al. 2020) Abbreviations: Kfs- K-feldspar; Plag- plagioclase. Trace element ratios, (h) $(La/Sm)_N$ vs. La shows that the granite magma evolved by fractional crystallization with some crustal contamination; (Wang et al. 2020) (i) $(La/Yb)_N$ vs. La showing magma evolution by partial melting; (de Wall et al. 2021)(j) Ba/Nb vs. Nb (de Wall et al. 2022) showing mantle source enrichment with decreasing degree of partial melting without any subduction component, (k) Ba/Th vs. Th (Hawkesworth et al. 1997) showing the absence of any subduction component.

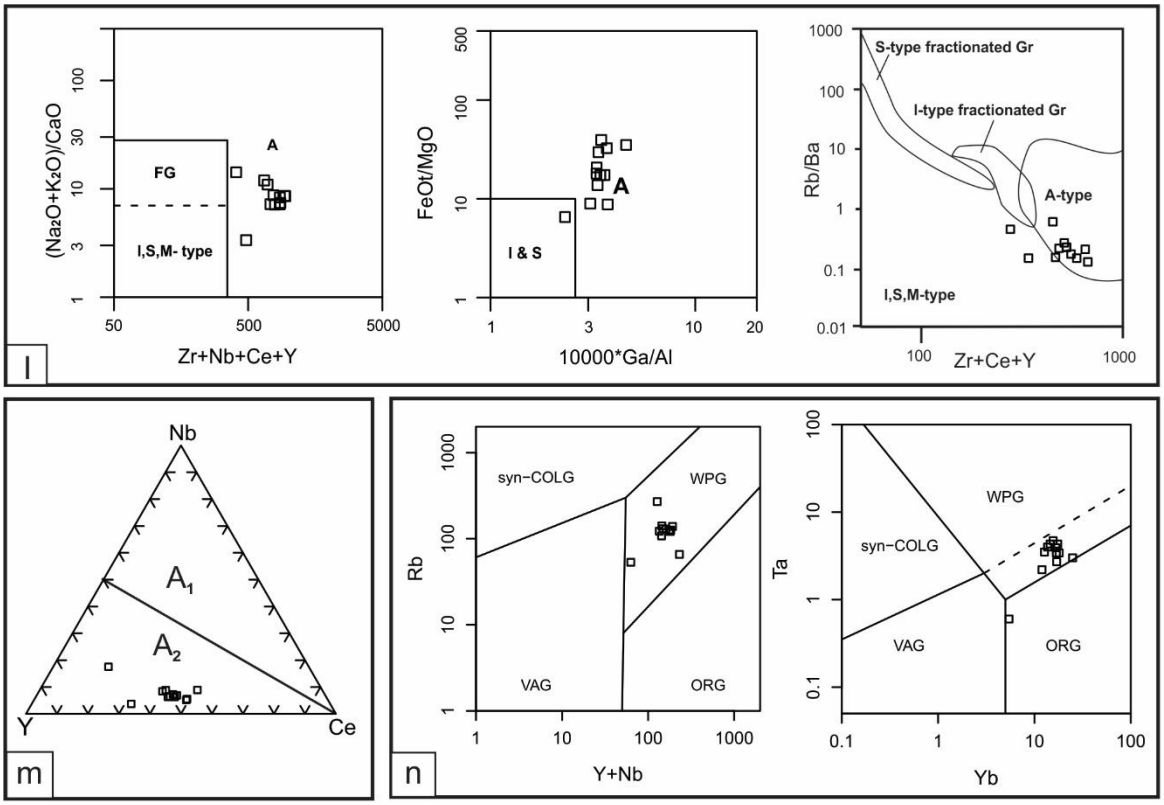

Fig. 4.3. Geochemical classification of the granites, (l) Chemical classification (discrimination) diagrams for A-type granites based on Whalen et al., 1987, (m) Representative plots for distinguishing between A_1 and A_2 granite (Eby 1992). (n) Tectonic discrimination showing Within Plate Granite affinity using the trace element (Rb vs. Y+Nb; Ta vs. Yb) diagrams of Pearce et al., 1984.

La (de Wall et al. 2021) show little variation with increasing La (Figs. 4.3 h, i). The Ba/Nb vs. Nb and Ba/Th vs. Th plots show some decrease in Ba/Nb, Ba/Th ratios with increasing Nb and Th respectively (Figs. 4.3 j, k). The granites plot as A-type in the discrimination diagram of Whalen et al. (1987) (Fig. 4.3 l). These can be further discriminated into the A_2 group of Eby (1992) (Fig. 4.3 m). These granites indicate a predominantly Within Plate Granite (WPG) affinity in the trace element (Rb vs. Y+Nb; Ta vs. Yb) based discrimination diagram of Pearce et al. (1984) (Fig. 4.3 n).

4.4.1: Magma Source and petrogenesis of the Granite:

Geochemical analyses were performed on twelve spatially separated granite plutons, reveal consistent geochemical signatures. In the granites with ferroan and calc-alkalic, metaluminous to weakly peraluminous characterisitics CaO, Fe_2O_3 and TiO_2 decrease with increasing SiO_2 suggest significant fractional crystallization of mafic minerals, accessory minerals (titanite, ilmenite and magnetite) and some plagioclase. The granites display depletion in Eu and Sr, suggesting a similarity to melt derived from partial melting of the lower crust or fractional crystallization of plagioclase from the magma at an earlier stage. In the primitive mantle–normalized trace elements diagram, granites exhibit significant enrichment in large ion lithospheric elements (LILE) such as Rb and Th and REE but depleted in Ba, Sr, P and Ti, while showing slight negative Nb anomalies. The negative Nb and Ti anomalies are believed to result from the fractionation of a Ti-bearing phase, while the negative P anomalies arise from apatite separation. The flat HREE indicates a lower degree of fractionation from melt (Wang et al. 2020). The elevation of HREE contents is the manifestation of the magmatic allanite in the rock (Landenberger and Collins, 1996). Low Eu/Eu* values suggest fractionation of plagioclase, K-feldspar, or both, as corroborated by the Ba vs. Eu/Eu*plot (Kamaunji et al. 2020) (Fig. 4.3 g). The $(La/Sm)_N$ vs. La plot suggests evidence of slight crustal contamination,

along with a strong fractional crystallization component during magma ascent (Wang et al. 2020) (Fig. 4.3 h). The $(La/Yb)_N$ vs. La content plot indicates a partial melting trend with a negligible amount of fractional crystallization component during magma ascent (de Wall et al. 2021) (Fig. 4.3 i). The low $(La/Yb)_N$ ratios (1.14 to 3.64 with an outlier 0.51) suggest an upper-crustal melt source (Rapp et al. 1991). However, the low $(La/Yb)_N$ values with significantly high HREE concentrations are considered to have been formed by the melting of sources in the dry lower crust (Landenberger and Collins, 1996). The samples reveal a trend of decreasing degree of partial melting coupled with mantle source enrichment and the absence of any subduction components, Ba/Nb vs. Nb (de wall et al. 2022), Ba/Th vs. Th (Hawkesworth et al. 1997) (Figs. 4.3 j, k).

4.4.2: Implication for tectonic setting of the Granite:

All the samples unequivocally fit the A-type granite category, with no discernable signatures of I or S-type granite fractions (Fig. 4.3 l). The presence of A-type granite suggests the involvement of mantle-derived melts, as no reports indicate the direct formation of A-type granite from crustal melts. All the data fall within the A_2 granite field in Nb-Y-Ce plot (Eby 1992) (Fig. 4.3 m). Tectonic discrimination diagram (Pearce et al. 1984) primarily suggests a Within Plate Granite (WPG) affinity (Fig. 4.3 n). These geochemical signatures collectively indicate crustal thinning and extension-related or anorogenic within-plate magmatism. The metaluminous to weakly peraluminous character of the samples may be attributed to the partial melting of I-type rocks, resulting in a plagioclase-rich residue at high temperature in the shallow crustal environment. The presence of flat HREE pattern and amphibole in the granite suggests the involvement of some mantle-derived juvenile melts in the formation of this A-type granite (Pearce et al. 1984, 2008). In summary, the geochemical characteristics of these

granites imply that the magma was generated through low partial melting of a lower crust, with some contribution from juvenile mantle materials and extensive fractional crystallization.

Chapter 5

Zircon geochronology

5.1: Introduction:

The U-Pb age dating technique represents a precise and potent means of determining the ages of crystallization and metamorphic events. Zircon, a mineral composed of $ZrSiO_4$, serves as an ideal candidate for age dating due to its remarkable resilience and resistance to subsequent geological processes. Additionally, it often contains substantial quantities of U, Th, and Pb. Advanced in situ microbeam techniques enable the examination of individual growth zones within zircon crystals, providing valuable insights into their growth sequences and the evolution of both the mineral and the surrounding rocks. This study aims to discuss the radiometric age data obtained from the zircon grains of the gabbro and granite rocks and its implications for the tectonics of northwestern India. The resulting analytical data are presented in Table 4. A concise overview of the U-Pb geochronology method is provided below:

The U-Pb dating method relies on the radioactive decay of uranium (U) and thorium (Th) isotopes into stable lead (Pb) isotopes. U naturally occurs as radiogenic isotopes 238U, 235U, and 234U, while Th primarily exists as the radiogenic isotope 232Th. Pb comes in the form of radiogenic isotopes 206Pb, 207Pb, and 208Pb, alongside the non-radiogenic isotope 204Pb, often referred to as common Pb, representing surface contamination on the sample. Each U and Th isotope is indicative of a chain of radiogenic daughter isotopes, all eventually decaying to stable Pb isotopes. For example, 238U decays to 206Pb, 235U to 207Pb, and 232Th to 208Pb. The concentrations of U, Th, and Pb in the Earth's mantle are exceedingly low. During the partial melting of the mantle, U, Th, and Pb preferentially incorporate into the liquid phase, resulting in an enrichment of these elements in the Earth's crust compared to the mantle. While common rock-forming minerals have low U and Th concentrations, accessory minerals, such as zircon, can contain high abundances of these elements. Zircon is a prevalent choice for U-Pb geochronology due to its abundance in most igneous and metamorphic rocks. It boasts exceptional chemical and mechanical resilience and readily incorporates U and Th, but not Pb.

Consequently, zircon contains virtually no Pb at the time of crystallization. As time progresses, the radioactive decay of U and Th produces Pb. By measuring the concentrations of U, Th, and Pb in a zircon sample and determining the isotopic composition of Pb, the age of the zircon can be accurately calculated.

5.2: Analytical Procedure for zircon analysis of gabbro samples:

For the U-Pb zircon geochronology, clean and fresh chunks of two representative gabbro samples (DC-2/P-927 and DK-67b, sample locations are shown in Fig. 5.1) were crushed into small pieces using a hydraulic oil press and powdered by an agate ball mill. Zircon grains were separated from powdered sample using hydraulic elutriation, followed by further separation with a hand-held Nd-magnet. The recovered zircon grains were mounted on a glass slide alongside standard zircon grains YO1 (with a TIMS 206Pb/238U age of 279.3 Ma, leached zircon; Herzig et al., 1997) using epoxy resin. The mounted grains were polished using 1 μm diamond until their major portions of the zircon grains were visible on the surface. Before isotopic analysis, optical and electron microscopic observations were conducted to assess the properties and structure of the separated zircon grains, guiding the selection of analysis points. Key characteristics of the zircon grains, such as size, colour, and shape, were examined using a Nikon Eclipse LV100 POL polarizing microscope. The internal structure of the zircon grains was analysed through backscattered electron (BSE) and cathodoluminescence (CL) images obtained via a JEOL JSM6390A Scanning Electron Microscope (SEM) at the Department of Earth and Planetary Systems Science, Hiroshima University, Japan. The zircon U-Pb isotope analysis was performed using a 213 nm Nd-YAG Laser coupled with a Thermo Fisher X-Series-II inductively coupled plasma ionization mass spectrometer (LA-ICP-MS) at Hiroshima University, Japan.

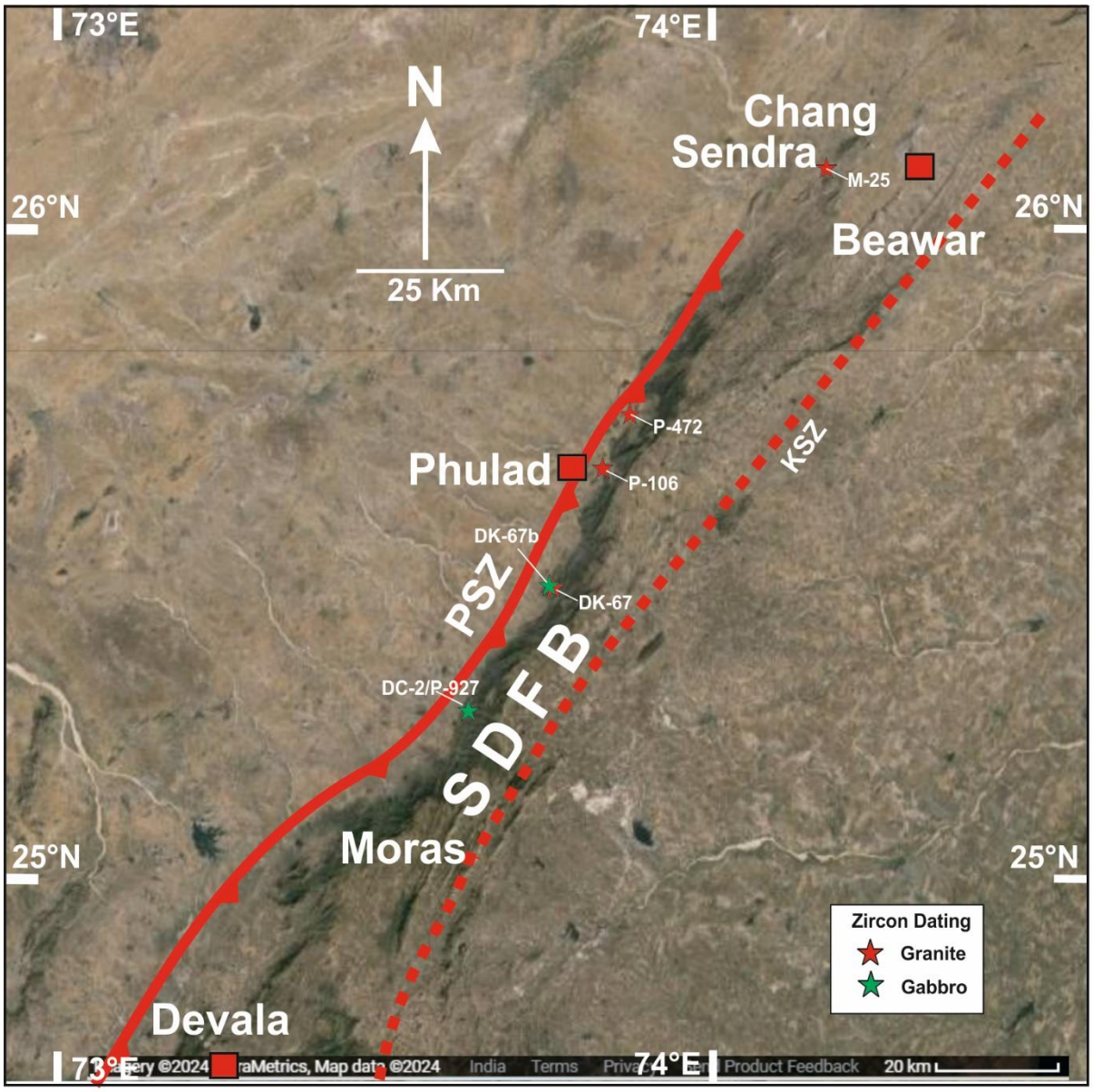

Fig. 5.1. Sample locations for age dating from zircon grains of the gabbro and granite rocks are shown in satellite image, taken from Google imagery, map data © 2024 of the SDFB.

Additional details regarding the analytical procedure, including the laser spot diameter, repetition rate, and the measurement of standard zircon grains to ensure data consistency and raw data processing, are given by Das et al. (2017) and Mavoungo et al. (2022). The age consistency standard of YO1 yielded a weighted average age of 282 ± 7 Ma which is close to its reported age of 279 Ma. The processed data plots were generated using the geochronological toolkit Isoplot/Ex version 3.7 (Ludwig, 2003). Less than 10% discordance is considered near-concordant and used for the age probability density plots for each of the samples. The selection of concordant data and the criteria for defining discordance are discussed by Mavoungo et al.

(2022). The calculation of the youngest zircon population age is performed using a module in Isoplot. In this process, each date is randomly perturbed based on its assigned Gaussian error. The mode, as well as the upper and lower limits on the mode of the sorted youngest dates, are then calculated to provide the best estimate of the youngest age, with the upper and lower limits representing the uncertainties at a 95% confidence level.

5.3: Analytical Procedure for zircon analysis of granite samples:

Zircon grains from four representative granite samples (DK-67, M-25, P-106, P-472, shown in Fig. 5.1) were separated from 3 to 5 kg of rock samples through conventional sieving, magnetic, and heavy liquid techniques as shown in the flow chart (Chart **1**). Thereafter, zircon grains

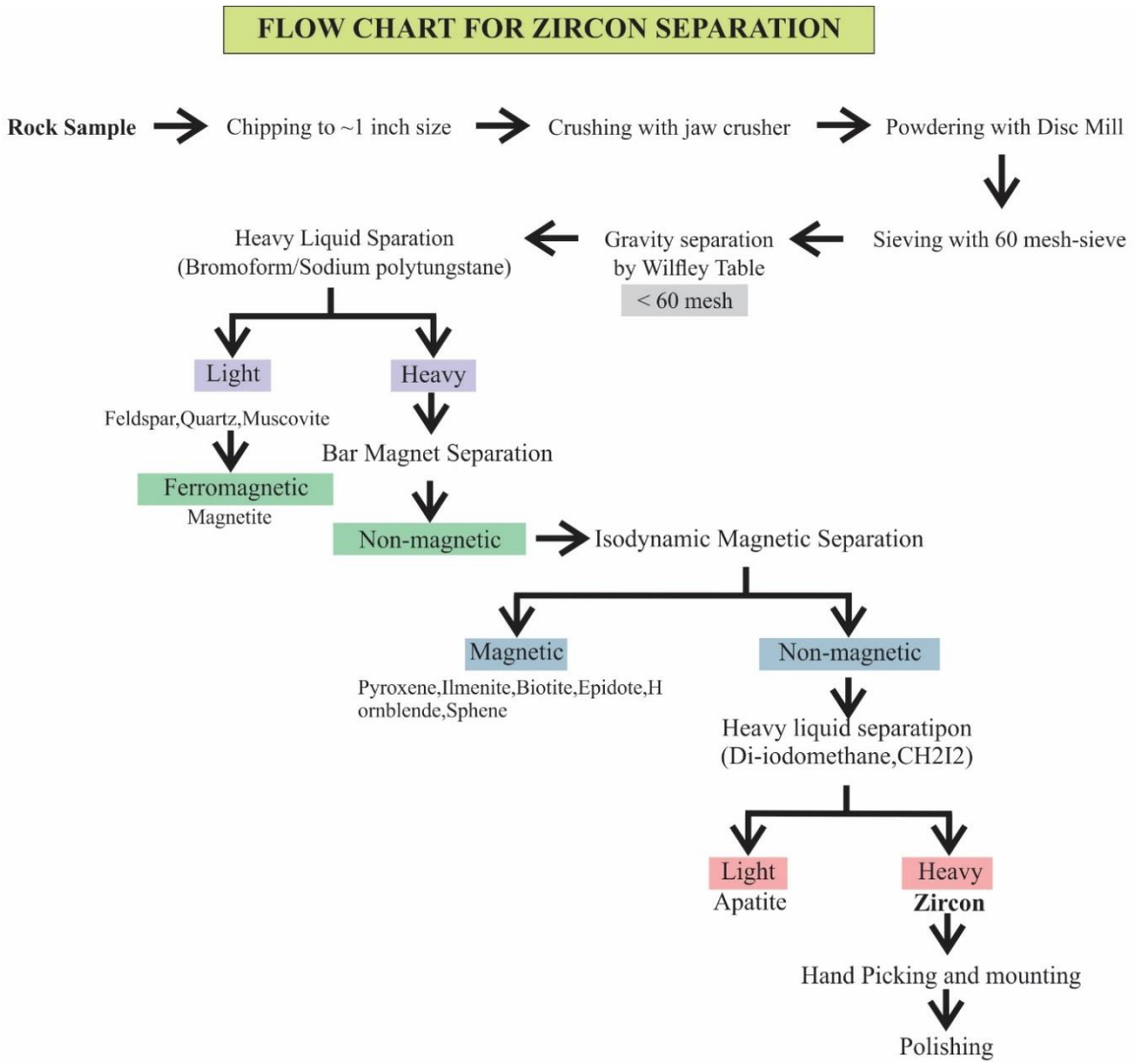

were handpicked using a stereo microscope and zircon grains were mounted in epoxy. The

mounted zircon grains were then polished using 8, 5, 3, 1, and 0.25 μm diamond paste. After polishing, cathodoluminescence (CL) images of the zircon grains were obtained at the Department of Geology and Geophysics, Indian Institute of Technology, Kharagpur, India. U-Pb dates were analyzed using a Resonetics Resolution M-50 series 193 nm excimer laser ablation system equipped with a Laurin Technic Pty S-155 ablation cell at Activation Laboratories, Ancaster, Ontario, Canada. Ablated aerosol from the sample was transported to the ICP-MS via nylon tubing with an in-line 'squid' smoothing device, positioned just before the junction with the ICP-MS torch. Isotope intensities were determined using an Agilent 7700x quadrupole-ICP-MS operating in 'auto' detector mode, with sensitivity and P/A factors fine-tuned by rastering across NIST610 glass prior to each run. To enhance sensitivity, an additional external rotary pump was utilized. The ICP-MS method measured the isotopes ^{90}Zr, ^{202}Hg, ^{204}Pb, ^{206}Pb, ^{207}Pb, ^{208}Pb, ^{232}Th, and ^{238}U, achieving a total quadrupole sweep time of 0.26 seconds. During ablation, the background-corrected 202Hg ion beam was used to peak strip any minor excess ^{204}Hg from the ^{204}Pb signal, using the ^{202}Hg/^{204}Hg ratio obtained from the gas background. Typically, the magnitude of this correction was negligible. The data were standardized against FC1 zircon (1099±2 Ma), which was analyzed at least 16 times per run and distributed evenly throughout the sequence. Each ablation lasted for 30 s and was preceded by 30 s of background collection. Data accuracy was verified using the Plesovice zircon standard (isotope dilution [ID] TIMS ^{206}Pb/^{238}U age = 337.13±0.37 Ma; Sláma et al. 2008). Offline data reduction was performed using VizualAge (Petrus and Kamber 2012) and Iolite v2.5 (Paton et al. 2011), operating as plugins in Wavemetrics Igor Pro 6.23. Concentration data were calculated relative to NIST610 (analysed distributed throughout the sequence) and using the Iolite trace elements "internal standardization" data reduction scheme. All diagrams were produced using the Isoplot V3.0 program (Ludwig 2003). The analytical data are presented in Table 3.

5.4: Results of gabbro zircon analysis:

Zircon grains in the gabbro are subhedral to euhedral, with lengths of 200–300 μm and aspect ratios of 2-3. These zircon grains are optically clear and colourless. CL images show oscillatory zoned (Fig. 5.2 a). The internal structure of the grains suggests an igneous origin. Thus, the

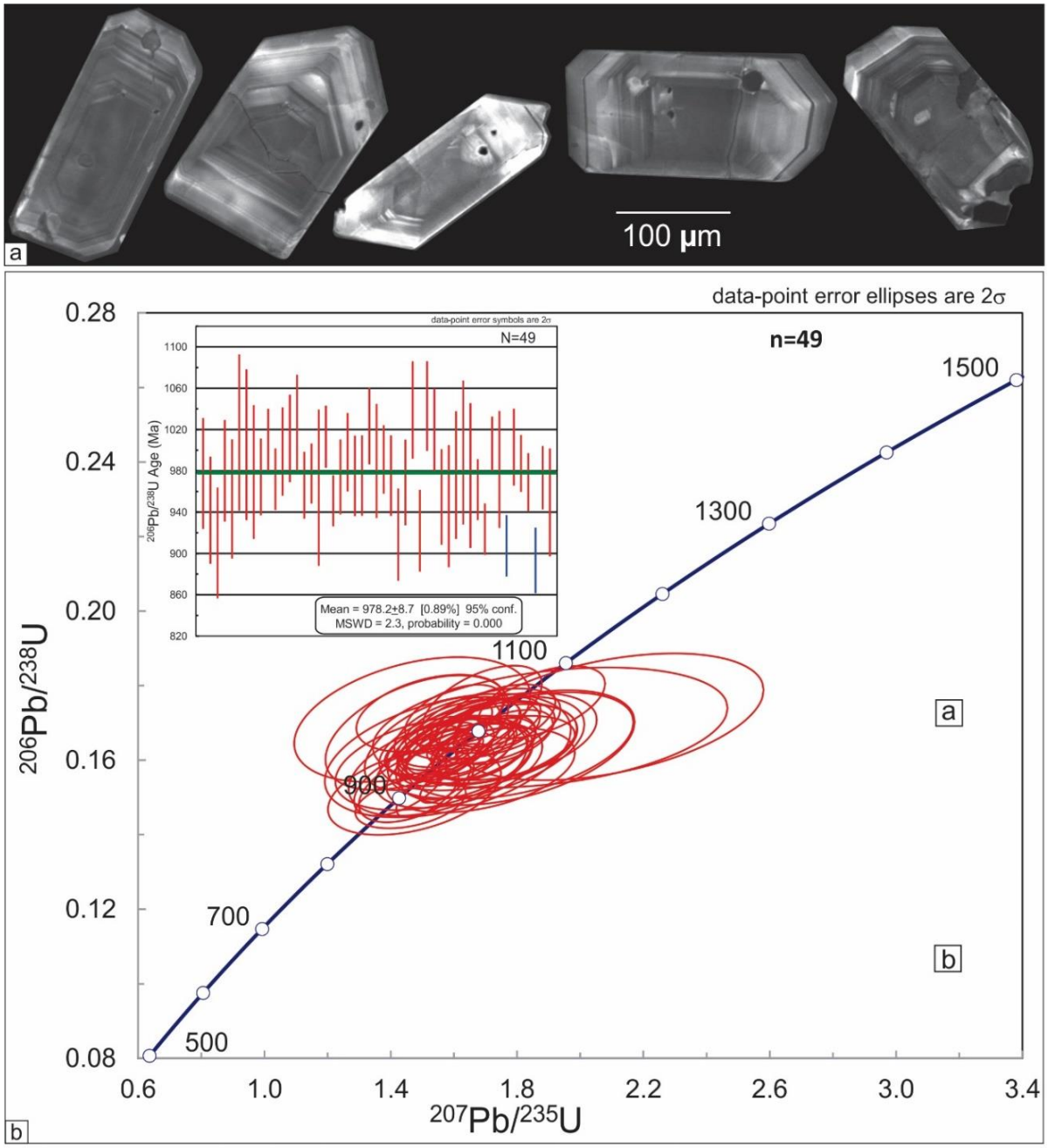

Fig. 5.2. Photomicrographs of Cathodoluminescence image (a) of zircon grains. Concordia and weighted average plots (b) of LA-ICP-MS zircon U-Pb data obtained from magmatic origin (oscillatory zoned cores).

dates obtained from the grains are interpreted to represent the timing of gabbro crystallization.

Data with <10% degree of discordance are considered to be concordant. $^{206}Pb/^{238}U$ and $^{207}Pb/^{235}U$ ratios in zircon grains were plotted in the Concordia diagram. The data obtained from the oscillatory igneous cores shows a cluster in the Concordia, and the data yield a Concordia age of 983.4±6.0Maigneous cores (Fig. 5.2 b). The weighted average age of $^{206}Pb/^{238}U$ age is 978.2±8.7 Ma (**N** = 49, MSWD= 2.3). Th/U values for older data show >0.5, which further suggests magmatic origin (Hoskin and Schaltegger 2003).

5.5: Results of granite zircon analysis:

Zircon grains in the granites are subhedral to euhedral, measuring 100–200 μm in length, with aspect ratios of 2-4. These zircon grains are optically clear and colourless. Cathodoluminescence (CL) images show oscillatory zoned crystals (Figs. 5.3a, b), sometimes with chemically homogeneous overgrowths (Fig. 5.3c). The internal structure of the grains thus

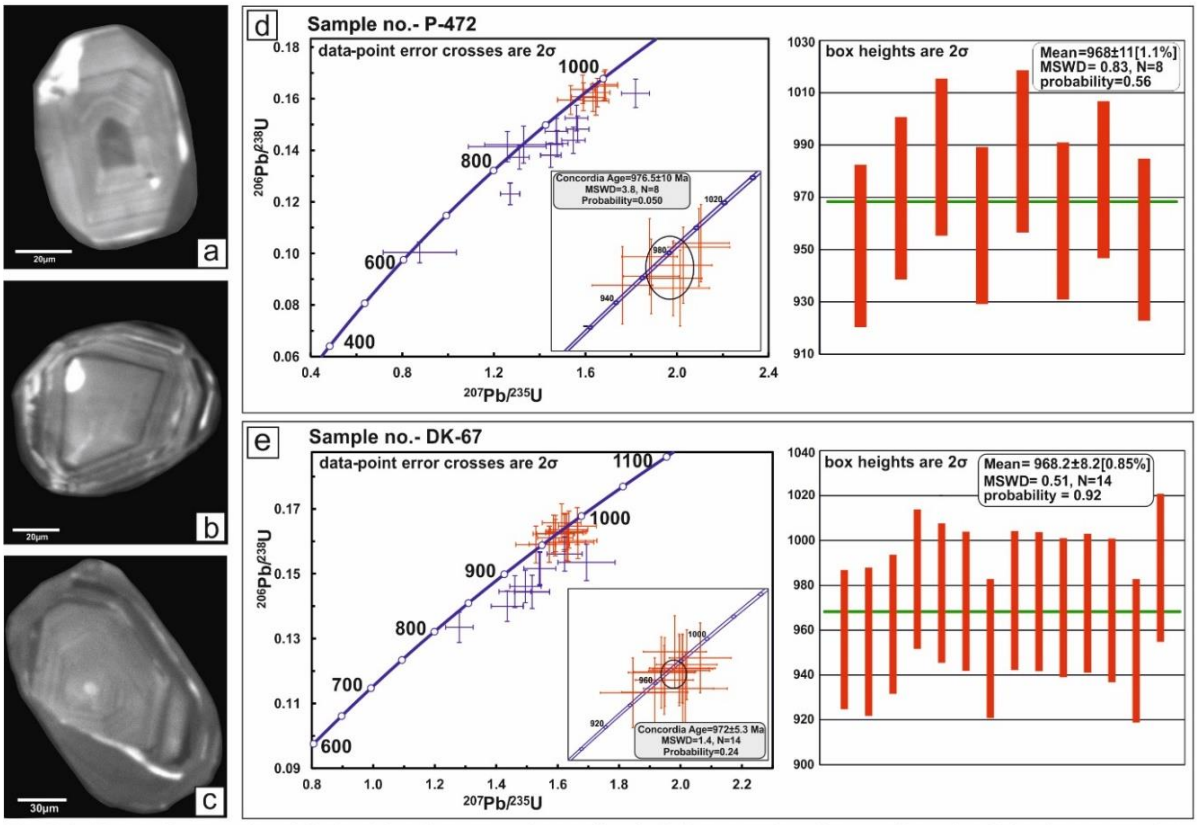

Fig. 5.3. Photomicrographs of Cathodoluminescence image (a–c) of zircon grains. Concordia and weighted average plots (d-e) of LA-ICP-MS zircon U-Pb data obtained from magmatic origin. Concordia plots of LA-ICP-MS zircon U-Pb data obtained from oscillatory zoned cores.

suggests igneous cores with metamorphic rims. Thus, the dates obtained from the igneous cores are interpreted to represent the timing of granite crystallization, while those from the chemically homogeneous overgrowths are seen to represent a later overprinting event. Data with <10% degree of discordance are considered to be concordant. Separate plots of $^{206}Pb/^{238}U$ and $^{207}Pb/^{235}U$ ratios in zircon grains were plotted in the Concordia diagram for four samples obtained from the oscillatory igneous cores (Figs. 5.3d-g). The Concordant dates from four different samples vary from 963.5±5.9 Ma to 976.5±10 Ma, and the weighted average of

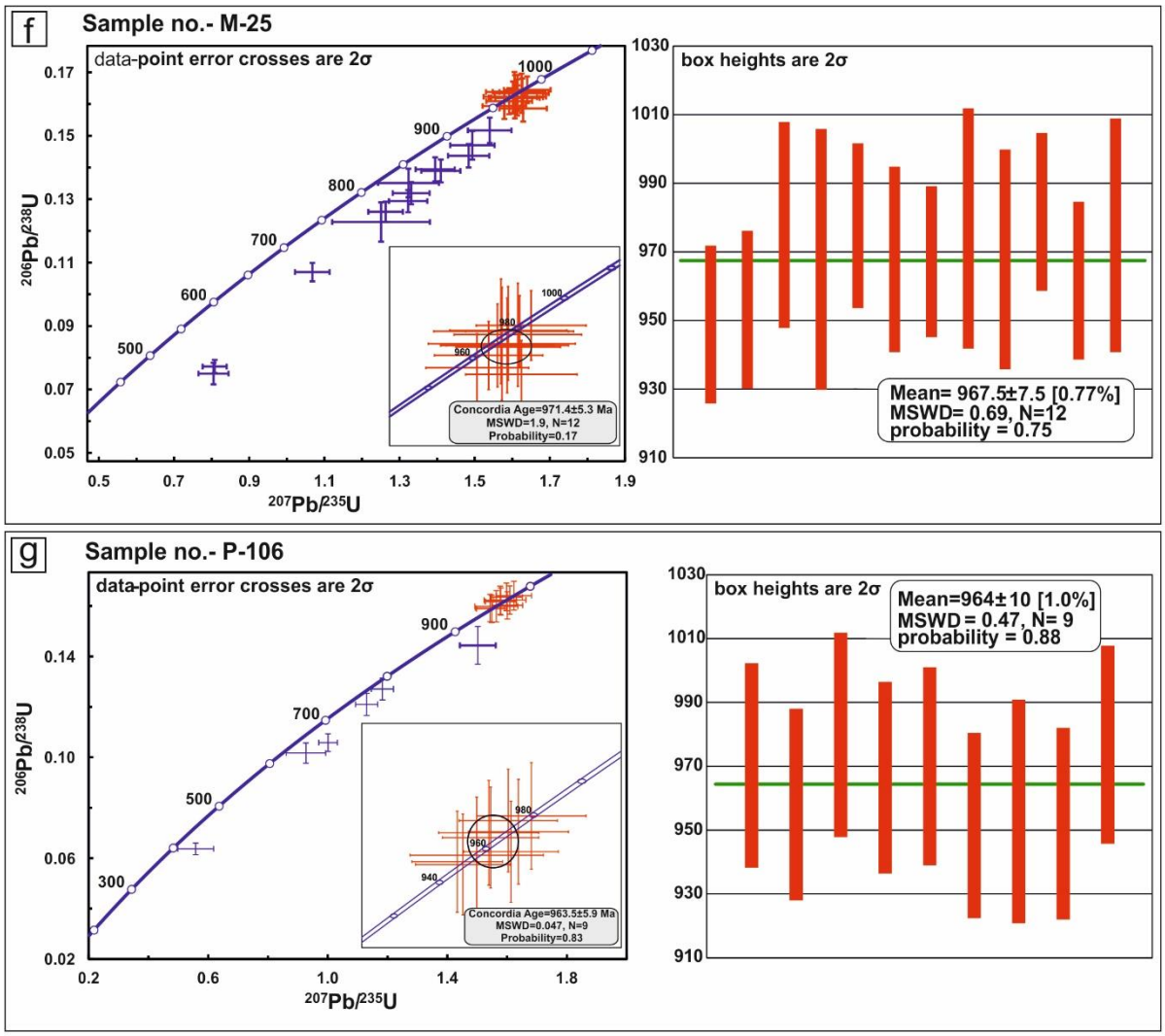

Fig. 5.3. contd. Concordia and weighted average plots (f-g) of LA-ICP-MS zircon U-Pb data obtained from magmatic origin. Concordia plots of LA-ICP-MS zircon U-Pb data obtained from oscillatory zoned cores.

$^{206}Pb/^{238}U$ age for four samples varies from 964±10 Ma to 968.2±8.2 Ma. Combining all the samples, the data yield a Concordia age of 970.7±2.9Ma obtained from the oscillatory igneous

cores (Fig. 5.3h). The weighted average of $^{206}Pb/^{238}U$ age is 967.3±4.4 Ma with MSWD (mean square weighted deviation) = 0.58. Concordant dates from chemically homogenous overgrowth were obtained from two samples only (P-106 and P-472). Data obtained from the chemically homogeneous overgrowths show a concordant age of 826.3±6.9 Ma (Fig. 5.3i). The weighted average of $^{206}Pb/^{238}U$ age is 823.4±8.3 Ma with MSWD = 0.99. Th/U values are plotted against $^{206}Pb/^{238}U$ age for different samples (Fig. 5.3j). Th/U values for older data show >0.5, which

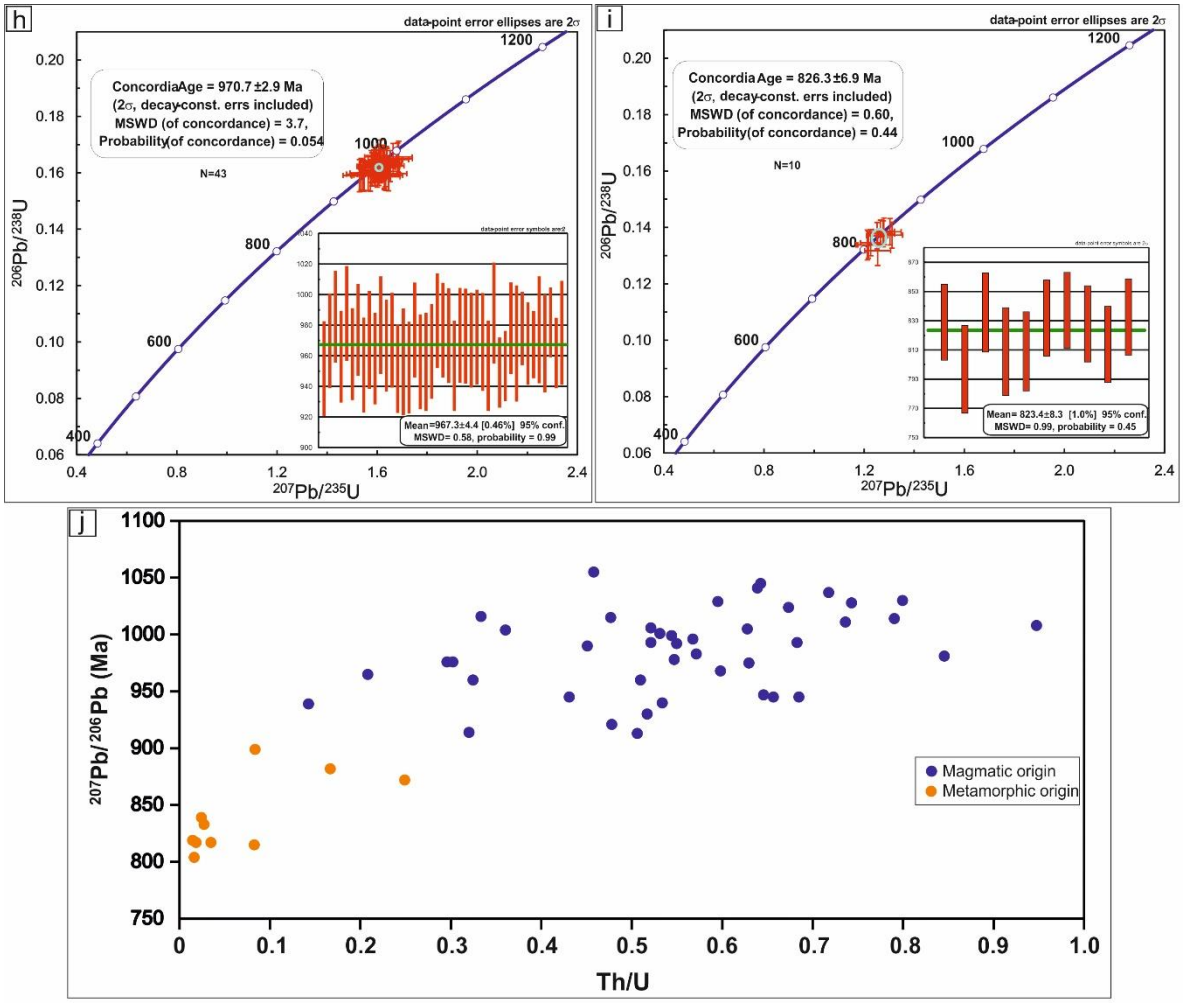

Fig. 5.3. contd. Concordia and weighted average plots of LA-ICP-MS zircon U-Pb data obtained from magmatic origin, oscillatory zoned cores (h) and obtained from metamorphic origin, chemically homogeneous overgrowth rims (i). Th/U vs. $^{207}Pb/^{206}Pb$ age plot of magmatic and metamorphic zircons (j).

further suggests magmatic origin, and younger data show <0.1, suggesting metamorphic origin (Hoskin and Schaltegger 2003).

5.6: Summary:

The geochronological study reveals that the zircon grains in this gabbro rocks and the granite show concordant age ~980-970 Ma which is the crystallization age of the gabbro and granites. In granites, the rimmed overgrowth on zircon represents a metamorphic event with a concordant age of 826.3±6.9 Ma. The metamorphic age observed in these granites can be attributed to reverse shearing age of ~820 Ma within the PSZ.

Chapter 6

Summary and Conclusion

6.1: Summary:

The current study focuses on the examination of gabbro and granite bodies 6-15 km wide, >200km long, located within the SDFB, positioned along a narrow linear zone east of the PSZ. This linear zone runs parallel to the regional strike of the fold belt in a northeast-southwest direction. It is observed that all the separated gabbro and the granite bodies display a consistent orientation, predominantly aligning with the northeast-southwest trend and exhibiting a steep easterly dip with oblique stretching lineation. Detailed field investigations revealed that the orientation of the foliation in the gabbro and granite bodies corresponds to the general trend observed in the SDFB as well as the mylonites found in the PSZ shear zone rocks. The foliation in the gabbro and granite runs parallel to the axial planar fabric of regional F2 folds within the SDFB. Further, strain analysis suggests that the deformation in the gabbro and the granite occurred in a transpressional regime. The development of foliation in gabbro and granite and lineation in these granites exhibit similarity in geometry and style to the structural elements of mylonitic foliation that formed within the PSZ. Thus, field relations indicate that the foliation in the gabbro, granites, mylonites in the shear zone and the regional F2 folding in the SDFB formed under the same stress regime, suggesting that the deformation in all these units is broadly synchronous.

Petrographic analysis was conducted on gabbro and granite bodies throughout the fold belt, revealing a consistent igneous assemblage and metamorphism pattern. The petrographic study of gabbro demonstrates the presence of plagioclase + orthopyroxene + clinopyroxene + Fe-Ti oxides + quartz. The solid-state foliation in the gabbro defined by stretched plagioclase and oriented amphibole grains and in granite defined by stretched quartz-feldspar grains is interpreted as tectonic foliation. The petrographic study demonstrates that the igneous assemblage is followed by a metamorphic imprint in both rocks. In gabbro, amphiboles replaced the primary orthopyroxenes and clinopyroxenes in reaction with plagioclases. Titanite

corona formed around the ilmenite grains. In some samples orthopyroxenes and plagioclases were replaced by garnet. In case of granite the formation of epidote-titanite-quartz symplectitic coronas on amphibole grains and titanite coronas on magnetite and allanite grains are observed. The growth of epidote-titanite-quartz symplectite shows a directional dimension by its formation dominantly along the foliation parallel faces of the amphibole grains. The preferred occurrence of the epidote-titanite-quartz assemblage on amphibole rims aligned with the foliation direction indicates that their development was related to the deformation event. This implies that the reaction was fluid-driven and took place during the fabric forming event, i.e. synchronous with the reverse shearing of the PSZ (Chatterjee et al. 2016, 2017). Titanite coronas form on all sides of the magnetite grains, suggesting post-deformational growth.

Geochemical analysis of this study reveals that the mafic melt originated from partial melting of the lithospheric mantle at relatively shallow depths during the upwelling of the asthenospheric mantle. This magma eventually emplaced in the continental crust, resulting in the melting of the continental crust. Gabbro shows flat HREE patterns, which indicate shallow-depth mantle melting and significantly high HREE concentrations in granite, indicating the melting of sources in the dry lower crust. Both the rocks show within-plate affinity in their respective tectonic discrimination diagram, which collectively indicates crustal thinning and an extension-related magmatism. In summary, the gabbro originated from the partial melting of a spinel peridotite facies of the lithospheric mantle and the granite was formed from the melt generated through low partial melting of a lower crust, with some contribution from juvenile mantle materials and extensive fractional crystallization.

Geochronological study reveals that the zircon grains in this gabbroic rock exhibit magmatic origin as evident from morphology, the internal structure of the grains and their high Th/U value. Thus, the ages obtained are taken to represent the crystallization age of the gabbro. The data plot shows a concordant age of 983.4±6Ma which represents the crystallization age of the

gabbro. The cores of the zircon grains in these granites exhibit magmatic origin, as evident from their morphology, internal grain structure, and high Th/U values. Therefore, the obtained ages are considered to represent the crystallization age of the granite. The data plot displays a concordant age of 970.7±2.9 Ma, representing the crystallization age of the granite. The rimmed overgrowth, unzoned in nature, represents a metamorphic event with a concordant age of 826.3±6.9 Ma. These ages corroborate the established metamorphic and magmatic ages of the SDFB (Chatterjee et al. 2017; Gangopadhyay and Lahiri 1984) and the metamorphic age agrees with the reverse shearing age of 810-820 Ma within the PSZ (Chatterjee et al. 2017, 2020, 2023). Our comprehensive structural analysis suggests that deformation in the granite and the mylonites within the shear zone occurred synchronously. Therefore, the younger age (~820Ma) observed in these granites can be attributed to the reverse shearing event within the PSZ.

6.2: A Tentative Tectonic Model for the gabbro and granitic plutons:

Summarizing the above information, the composition of the gabbro rocks within the SDFB lies from N-MORB to E-MORB (Fig. 4.2f) with flat HREE patterns which simply cannot be derived from either arc or slab-failure rocks. Trace elements data suggest that crustal contamination, with a lower degree of fractionation and partial melting of spinel peridotite, played a pivotal role in the genesis of these gabbro rocks. In the tectonic discrimination diagram, samples displayed the Within Plate Basalt to Continental Arc trend and studied granite formation is attributed to the melting of the lower crust within an extensional regime. In addition, the gabbro rocks are always closely associated with 1Ga granite (A-type). Such bimodal magmatism is a typical feature of magmatic processes within an extensional tectonic regime. The absence of crustal rocks older than 0.88 Ga to the west of the SDFB suggests that this extensional regime was likely induced by slab roll-back of an eastward-dipping subducting

oceanic crust beneath the SDFB. This tectonic process causing crustal thinning would facilitate the upwelling of the mantle lithosphere, leading to the formation of mafic magma (resulting from low partial melting of spinel peridotite). This magma ponds beneath the lower crust and subsequent gabbro formation by emplacement of this mafic magma in the crust and granite formation by melting of the lower crust.

Integrating field relations, petrography, geochemistry and geochronology of the studied gabbroic and granitic rocks, the possible petrogenetic model for the origin of the gabbro and granitic plutons is presented in Figure 8. According to this model, ca. 1Ga, an oceanic plate was subducted eastward beneath the SDFB (Fig. 8a). Subsequently, the oceanic plate began to roll back, causing crustal thinning in the SDFB (Fig. 8b). This tectonic activity likely facilitated the upwelling of the mantle lithosphere, resulting in the formation of mantle-derived basaltic magma from low partial melting of spinel peridotite. This magma accumulates in a large chamber at the lower crust or crust–mantle boundary. The basaltic magma underplated the continental crust, remaining relatively stationary for an extended period. Concurrently, heat flow from the upwelling asthenospheric mantle, along with the heat released by crystallizing mafic phases, induced significant partial melting in the overlying continental crust. This process led to the formation of gabbro through the emplacement of mafic magma in the crust and granite through the melting of the lower crust (Fig. 8c). Previous studies have dated the basement rocks of the Marwar Craton to around 880 to 860 Ma (Chatterjee et al., 2023). It is suggested that this craton was not part of present-day India until approximately 820 Ma (Fig. 8d). Finally, around 820 Ma, the Marwar Craton sutured with the SDFB along the PSZ, forming the greater Indian landmass and leading to the exhumation of the gabbro and granites (Fig. 8e). However, alternative models proposed by early workers suggest that the SDFB developed in a rift setting with westward subducting continental crust (Bhowmik et al. 2010; Ghosh et al. 2022**)**. Such a tectonic setup would demand the presence of older crust across the Marwar

craton-SDFB boundary. However, previous studies have demonstrated that the basement rocks of the Marwar craton date to 880 and 860 Ma (Fig. 8d) (Chatterjee et al., 2023). Additionally, it has been established that the Marwar craton and the SDFB share a common crustal history

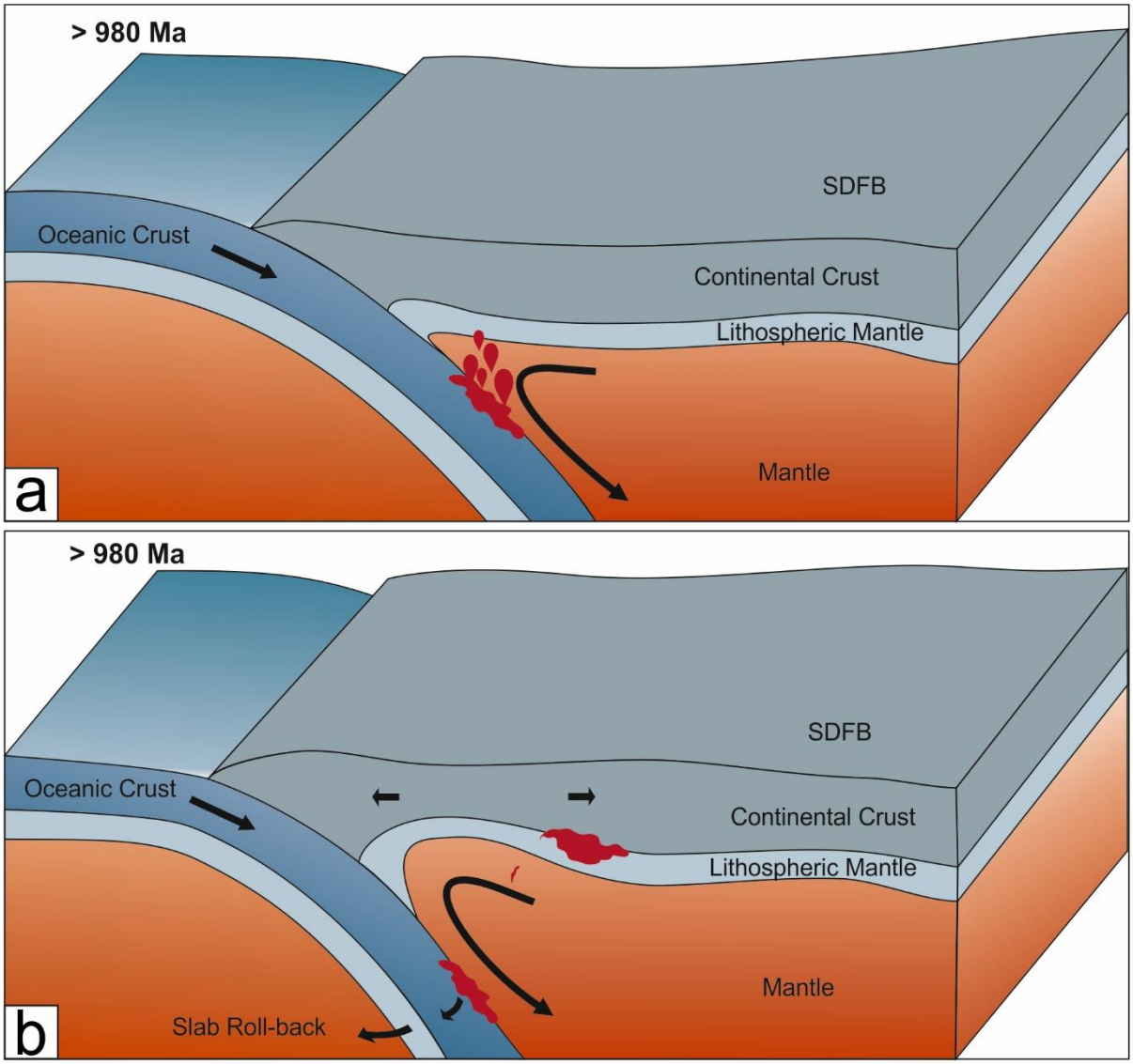

Fig. 8. Schematic model (not to scale) for magmatic evolution in SDFB, NW India and associated magmatic activity; a) shows the situation (oceanic crust subducted eastward beneath the SDFB) before ca. 980Ma, b) subducted oceanic crust starts to roll back, causing extension in the SDFB.

only from periods younger than 0.82 Ga (Chatterjee et al., 2017, 2020, 2023). During the suturing of the Marwar craton with the SDFB along the PSZ, the exhumation of these gabbro and granites occurred at 820 Ma. This process was synchronous with reverse shearing along the PSZ and regional deformation of the SDFB (Fig. 8e).

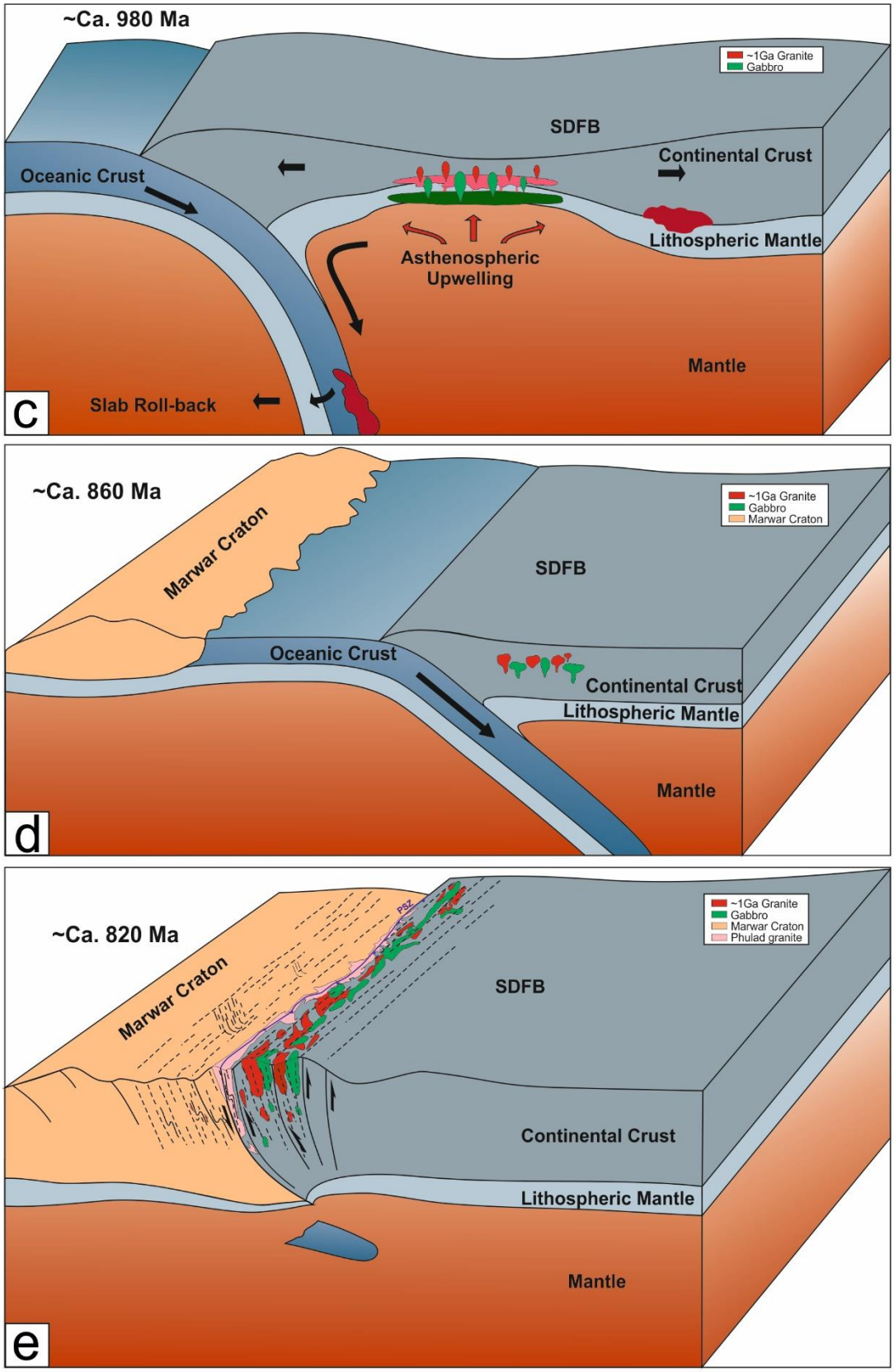

Fig. 8. Contd. Schematic model (not to scale) for magmatic evolution in SDFB, NW India and associated magmatic activity; (c) Gabbro formed through the partial melting of lithospheric mantle due to the upwelling of the mantle lithosphere during crustal thinning and granites formed through the melting of the lower crust due to crustal thinning with the involvement of mantle-derived melt at 980 Ma, (d) The basement rocks of the Marwar Craton to around 880 to 860 Ma (Chatterjee et al., 2023), was not part of present-day India until approximately 820 Ma, (e) Gabbro and granites exhumed in the SDFB at 820 Ma, during the suturing of the Marwar craton with the rest of India to form the Greater India.

6.3: *Regional Implications:*

The PSZ has long been identified as a Proterozoic suture zone (Gupta et al. 1980) that demarcates the boundary between the SDFB to the east and the Marwar craton to the west. The PSZ has been characterized as a terrane boundary along which the Marwar craton accreted to the rest of India to form the Greater India landmass at ~810-820 Ma (Chatterjee et al. 2017, 2020). A recent report of a porphyritic granite (Phulad granite) with ~ 820 Ma magmatic age (Chatterjee et al. 2020) that occurs parallel to the PSZ and intrudes rocks of both the Marwar craton and the SDFB supports this idea (Chatterjee et al. 2020, 2023). Chatterjee et al. (2020) explained the Phulad granite as a stitching pluton that was emplaced syn-tectonically during the suturing of the Marwar craton with the rest of India along the PSZ at 810-820 Ma.

Until now, the occurrences of ~1Ga granites of the SDFB were correlated with the assembly of the Rodinia supercontinent. However, there have been no reports of any collisional fabric at ~1Ga from this area. The present work showed that all the gabbro and ~1Ga granites are restricted to the SDFB and are absent to the west of the PSZ. Furthermore, all the gabbro and ~1Ga granites along the ~200 km stretches exhibit similar field relations, structures, petrography, mineral chemistry and geochemistry respectively. This suggests that these gabbro bodies and spatially separated ~1 Ga granites in the SDFB region formed during a single geological event. The geochemical analysis in the study suggests extension-related magmatism, implying that the gabbro and granite crystallized in an extensional regime (Fig. 8c). In contrast, the assembly of the Rodinia Supercontinent demands a collisional or compressional regime. Additionally, the present study reveals that deformation and metamorphism in the granites occurred at 820 Ma during the suturing of the Marwar craton along the PSZ (Fig. 8e). This fact provides an important constraint on the palaeogeographic reconstruction of the Rodinia supercontinent and the role of northwest India. Furthermore, it

has been proposed that this gabbro formed through the partial melting of spinel peridotite due to the upwelling of the mantle lithosphere and granites formed through the melting of the lower crust due to crustal thinning with the involvement of mantle-derived melt at 970 Ma. Exhumation of these gabbro and granites occurred at 820 Ma, synchronous with reverse shearing along the PSZ and regional deformation of the SDFB during the suturing of the Marwar craton with the rest of India to form the Greater India at 810-820 Ma.

6.4: Conclusions:

1. The U–Pb zircon age shows that the gabbro and granite in the SDFB intruded at ca. 980Ma, indicating a magmatic event in the northwestern section of India.

2. The gabbro is tholeiitic affinity, and its source magma was probably formed due to the lower degree partial melting of the spinel peridotite zone of the lithospheric mantle, and this A-type granite is ferroan to calc-alkaline affinity probably formed due to melting of lower crust, induced by mantle melts which was modified by crustal contamination during magma accent.

3. Both the gabbro and A-type granite were generated in an extensional geodynamic setting, most likely induced by rollback of the paleo-oceanic subducting plate beneath the SDFB.

4. Exhumation of these gabbro and granites occurred at 820 Ma, during the suturing of the Marwar craton with the SDFB to form the Greater India.

References

References:

Abdel-Rahman, A. F. M, and Nassar, P. E. 2004. Cenozoic volcanism in the Middle East: petrogenesis of alkali basalts from northern Lebanon. *Geological Magazine* 141 (5): 545–563. https://doi.org/10.1017/S0016756804009604

Adak, V. and Dutta, U. 2021. Genesis of coronae and implications of an early Neoproterozoic thermal event: a case study from SE Chotanagpur Granite Gneissic Complex, India. Geological Magazine 158, 199–218. doi: 10.1017/ S0016756820000357.

Banerjee. M., Dutta, U., Anand, R. and Atlas, Z. D. 2019. Insights on the process of two-stage coronae formation at olivine-plagioclase contact in mafic dyke from Palghat Cauvery Shear Zone, southern India. Mineralogy and Petrology 113, 625–49.

Batiza, R. and Niu, Y. L. 1992. Petrology and magma chamber processes at the East Pacific Rise ˜9°30'N. Journal of Geophysical Research 97, 6779–6797.

Bhowmik, S. K., Bernhardt, H. J. and Dasgupta S. 2010. Grenvillian age high-pressure upper amphibolite-granulite metamorphism in the Aravalli-Delhi Mobile Belt, Northwestern India: New evidence from monazite chemical age and its implication: Precambrian Research, 178, 168–184.

Bhowmik, S. K., Saha, L., Dasgupta, S. and Fukuoka, M. 2009. Metamorphic phase relations in orthopyroxene-bearing granitoids: implication for high-pressure metamorphism and prograde melting in the continental crust: Journal of Metamorphic Geology, 27, 295-315.

Boynton, W. V. 1984. Geochemistry of Rare Earth Elements: Meteorite Studies. In: Henderson, P., Ed., Rare Earth Element Geochemistry, Elsevier, New York, 63-114. http://dx.doi.org/10.1016/B978-0-444-42148-7.50008-3.

Brey, G. 1984. Subsolidus orthopyroxene-dinopyroxene systematics in the system CaO-MgO-SiO2 to 60 kb: a revaluation of the regular solution modeL *Contr. Miner. Petrol.* 87, 35-42.

Brey, G. P. and Kohler, T. 1990. Geothermobarometry in Four-phase Lherzolites II. New Thermobarometers, and Practical Assessment of Existing Thermobarometers. Journal of Petrology.

Chatterjee, S. M., Roy Choudhury, M. and Das, S. 2016. Reaction enhanced channelized fluid-flux along mid crustal shear zone: An example from Mesoproterozoic Phulad Shear Zone, Rajasthan, India: Journal of Earth System Science, 125(7), 1321-1328.

Chatterjee, S. M., Roy Choudhury, M., Das, S. and Roy, A. 2017. Significance and dynamics of the Neoproterozoic (810 Ma) Phulad Shear Zone, Rajasthan, NW India: Tectonics, 36, 1432-1454.

Chatterjee, S. M., Roy, A. Manna., A. and Sarkar, A. K. 2023. Early Neoproterozoic tectonics in the Marwar Crustal Block (NW India), the relevance of the Phulad Shear Zone, and implications for Rodinia reconstruction: Geosphere, doi: 10.1130/GES02565.1.

Chatterjee, S. M., Sarkar, A. K., Roy, A. and Manna, A. 2020. Mid-Neoproterozoic tectonics of Northwestern India: Evidence of Stitching pluton along 810Ma Phulad Shear Zone: Tectonics, v. 39, e2019TC005902, doi:10.1029/2019TC005902.

Cheng, J. X., Li, W. X., Wang, X. C., Li, X. H. and Pang, C. J. 2020. Petrogenesis of ca. 830 Ma Lushan bimodal volcanic rocks at the southeastern margin of the Yangtze Block, South China: Implications for asthenospheric upwelling and reworking of juvenile crust. Precambr. Res. 342 https://doi.org/10.1016/j.precamres.2020.105673.

Chowdhury, P., Talukdar, M., Sengupta, P., Sanyal, S. and Mukhopadhyay, D. 2013. Controls of PT path and element mobility on the formation of corundum pseudomorphs in Paleoproterozoic high-pressure anorthosite from Sittampundi, Tamil Nadu, India. American Mineralogist 98, 1725–37.

Connolly, J. A. D. 2005. Computation of phase equilibria by linear programming: a tool for geodynamic modeling and its application to subduction zone decarbonation. Earth and Planetary Science Letters 236, 524–41 (updated in 2018).

Das, K., Bose, S., and Ghosh, G. 2017. The Neoarchean-Paleoproterozoic basin development and growth of the Singhbhum Craton, eastern India and its global implications: Insights from detrital zircon U-Pb data. Precambrian Research 298:123-145
DOI: 10.1016/j.precamres.2017.06.008

De Wall, H., Pandit, M.K., Donhauser, I., Schöbel, S., Wang, W. and Sharma, K. K. 2018. Evolution and tectonic setting of the Malani – Nagarparkar Igneous Suite: A Neoproterozoic Silicic-dominated Large Igneous Province in NW India-SE Pakistan: Journal of Asian Earth Sciences, v. 160, p. 136–158. doi:10.1016/j.jseaes.2018.04.016.

de Wall, H., Regelous, A., Schulz, B., Hahn, G., Bestmann, M. & Sharma, K. K. (2021). Neoproterozoic geodynamics in NW India – evidence from Erinpura granites in the South Delhi Fold Belt: International Geology Review, 1 -30.

de Wall, H., Regelous, A., Tomaschek, F., Bestmann, M., Hahn, G. and Sharma, K. K. 2022. Tonian evolution of an active continental margin - a model for Neoproterozoic NW India-SE Pakistan–E Oman linkage: Precambrian Research, 381, 106822.

Deb, M., Thorpe, R. I., Kristic, D., Corfu, F. and Davis, D. W. 2001. Zircon U-Pb and galena Pb isotope evidence for an approximate 1.0 Ga terrane constituting the western margin of the Aravalli-Delhi orogenic belt, northwestern India: Precambrian Research, 108, 195–213.

Dharma Rao, C. V., Santosh, M., Kim, S. W. and Li, S. 2013. Arc magmatism in the Delhi Fold Belt: SHRIMP U-Pb zircon ages of granitoids and implications for Neoproterozoic convergent margin tectonics in NW India: Journal of Asian Earth Science, 78, 83-99.

Donnelly, K. E., Goldsteina, S. L., Langmuir, C. H., and Spiegelman. M. 2004. Origin of enriched ocean ridge basalts and implications for mantle dynamics Kathleen E. Earth and Planetary Science Letters, 226, 347 – 366.

Eby G. N. 1990. The A-type granitoids: A review of their occurrence and chemical characteristics and speculations on their petrogenesis: Lithos, 26, 115-134.

Eby, G. N. 1992. Chemical subdivision of the A-type granitoids: petrogenetic and tectonic implications: Geology, 20, 641–644.

Finnerty, A. A. and Boyd, F. R. 1987. Thermobarometry for garnet peridotites: basis for determination of thermal and compositional structure of the upper mantle. In: Nixon, P. H. (ed.) *Mantle Xenoliths.* New York: John Wiley.

Flinn, D. 1962. On folding during three-dimensional progressive deformation: Quart, Journal of Geological Society, London, 118, 385–433.

Frost, B. R., Barnes, C. G., Collins, W. J., Arculus, R. J., Ellis, D. J. and Frost, C. D. 2001. A Geochemical Classification for Granitic Rocks: Journal of Petrology, 42(11), 2033–2048. doi:10.1093/petrology/42.11.2033.

Fry, N. 1979. Random point distributions and strain measurement in rocks: Tectonophysics, 60, 89-105.

Gangopadhyay, P. K. and Lahiri, A. 1984. Earth's crust and evolution of the Supergroup in central Rajasthan. In: Proceedings of the seminar on Crustal evolution of Indian shield and its bearing on metallogeny, India: Journal of Earth Science, 92–113.

Ghosh, S. K., Hazara, S. and Sengupta, S. 1999. Planar, non-planar and refolded sheath folds in the Phulad Shear Zone, Rajasthan: Journal of Geological Society of India, 21, 1715–1729.

Ghosh, S. K., Sen, G., & Sengupta, S. (2003). Rotation of long tectonic clasts in transpressional shear zones. *Journal of structural geology*, *25*, 1083–1096.

Ghosh, S., D'Souza, J., Goud, B.R. and Prabhakar, N. 2022. A review of the Precambrian tectonic evolution of the Aravalli craton, northwestern India: structural, metamorphic and geochronological perspectives from the basement complexes and supracrustal sequences. Earth Sci. Rev. 232, https://doi.org/10.1016/j.earscirev.2022.104098.

Golani, P. R., Reddy, A. B. and Bhattacharjee, J. 1998. The Phulad Shear Zone in Central Rajasthan and Its Tectonostratigraphic Implications, edited by B. S. Paliwal, 272-278, The Indian Precambrian: Scientific Publishers (India), Jodhpur, India.

Gupta, P., Fareeduddin, R. M. and Mukhopadhyay, K. 1995. Stratigraphy and structure of Delhi Supergroup of rocks in central part of Aravalli Range: Geological Survey of India, *120*(2-8), 12-26.

Gupta, S. N., Arora, Y. K., Mathur, R. K., Iqbaluddin, B. P., Prasad, B., Sahai, T. N. and Sharma, S. B. 1980. Lithostraigraphic map of Aravalli Region, southern Rajasthan and northeastern Gujrat: Geological Survey of India. Hawkesworth, C., Turner, S., Peate, D., McDermott, F. & Van Calsteren, P. 1997. Elemental U and Th variations in island arc rocks: implications for U-series isotopes: Chemical Geology, *139*(1-4), 207-221.

Hawkesworth, C., Turner, S., Peate, D., McDermott, F. and Calsteren, P. V. 1997. Elemental U and Th variations in island arc rocks: implications for U-series isotopes, Chemical Geology, 139, (1–4) 207-221. https://doi.org/10.1016/S0009-2541(97)00036-3.

Heron, A. M. 1953. The geology of central Rajputana: Geological Survey of India Memoir. *79*, 1–389.
Herzig, C. T., Kimbrough, D. L. and Hayasaka, Y. 1997. Early Permian zircon uranium-lead ages for plagiogranites in the Yakuno ophiolite, Asago district, Southwest Japan. *Island Arc*, *6*(4), 396-403.

Holland, T. J. B. and Powell, R. 2011. An improved and extended internally consistent thermodynamic dataset for phases of petrological interest, involving a new equation of state for solids. Journal of Metamorphic Geology 29, 333–83. doi: 10.1111/j.1525-1314.2010.00923.x.

Holland, T. and Blundy, J. 1994. Non-ideal interactions in calcic amphiboles and their bearing on amphibole-plagioclase thermometry. Contributions to Mineralogy and Petrology 116, 433–47.

Holland, T., and Blundy, J., 1990. Calcic amphibole equilibria and a new amphibole-plagioclase geothermometer. Contributions to Mineralogy and Petrology, 111, 264–266.

Hoskin, P. W. and Schaltegger, U. 2003. The composition of zircon and igneous and metamorphic petrogenesis: Review of Mineralogy and Geology, *53*(1), 27-62. https://doi.org/10.1017/S0016756821001345

Hu, R., Li, F., Yu, H. and Yang, J. 2019. Application of ImageJ in the rock thin section image analysis: the separation and quantitative calculation of crystal-glass two phases. Journal of Earth Sciences and Environmental Studies 4, 609–16.

Irvine, T. N., Baragar, W. R. A. 1971. A guide to the chemical classification of the common volcanic rocks. Can. J. Earth Sci. 8, 523–548. https://doi.org/10.1139/e71-055.

Jansen, M. N., MacLeod, C. J., Johan Lissenberg, C., Parkinson, I. J., and Condon, D. J. 2024. Relationship between D- MORB and E-MORB magmatism during crustal accretion at mid-ocean ridges: Evidence from the Masirah ophiolite (Oman). Geochemistry, Geophysics, Geosystems, 25, e2023GC011361. https:// doi.org/10.1029/2023GC011361

Johnson, M. C. and Rutherford, M. J. 1989. Experimental Calibration of the Aluminium in Hornblende Geobarometer with Application to Long Valley Caldera (California) Volcanic Rocks. Geology, 17, 837-841.
https://doi.org/10.1130/00917613(1989)017<0837:ECOTAI>2.3.CO;2

Kamaunji, V. D., Wang, L. X., Ahmed, H. A, Zhu, Y. X., Vincent, V. I. and Girei M. B. 2020. Coexisting A1 and A2 granites of Kudaru Complex: implications for genetic and tectonic diversity of A-type granite in the Younger Granite province, north-central Nigeria: International Journal of Earth Science (Geol Rundsch), 109, 511-535. doi:10.1007/s00531-020-01818-8.

Khan, M. S., Smith, T. E., Raza, M. and Huang, J. 2005. Geology, geochemistry and tectonic significance of mafic-ultramafic rocks of Mesoproterozoic Phulad Ophiolite Suite of South Delhi Fold Belt, NW Indian Shield. Gondwana Research, 8, 553–556.

Khan, M.S., Irshad, R. and Khan, T. 2019. Geochemistry of Mafic–Felsic Rocks of Phulad Ophiolite, in and Around Pindwara-Mount Abu Region, South Delhi Fold Belt, NW Indian

Shield: Implications for Its Tectonic Evolution. Society of Earth Scientists Series Geological Evolution of the Precambrian Indian Shield, 401-441. DOI:10.1007/978-3-319-89698-4_17
Landenberger, B. and Collins, W. J. 1996. Derivation of A-Type Granites from a Dehydrated Charnockitic Lower Crust: Evidence from the Chaelundi Complex, Eastern Australia. Journal of Petrology, 37, 145-170. https://doi.org/10.1093/petrology/37.1.145.

Lang, H. M. and Rice, J. M. 1985. Regression modelling of metamorphic reactions in metapelites, Snow Peak, northern Idaho. Journal of Petrology 26, 857–87.

Lang, H. M., Watcher, A. J., Peterson, V. L. and Ryan, J. G. 2004. Coexisting clinopyroxene/spinel and amphibole/spinel symplectites in metatroctolite from the Buck Creek ultramafic body, North Carolina Blue Ridge. American Mineralogist 89, 20–30.

Lassiter, J. C. and DePaolo, D. J. 1997. Plume/lithosphere interaction in the generation of continental and oceanic flood basalts: chemical and isotopic constraints. In: Mahoney, J.J., Coffin, M.F. (Eds.), Large Igneous Provinces: Continental, Oceanic, and Planetary Flood Volcanism. Geophysical Monograph Series. American

Leake, B. E., Woolley, A. R., Birch, W. D., Burke, E. A. J., Ferraris, G., Grice, J. D., Hawthorne, F. C., Kisch, H. J., Krivovichev, V. G., Schumacher, J. C., Stephenson, N. C. N. and Whittaker, E. J. W. 2004. Nomenclature of amphiboles: Additions and revisions to the International Mineralogical Association's amphibole nomenclature: American Mineralogy, 89, 883-887.

Ludwig, K. R. 2003. Isoplot/Ex version 3.0. A geochronological toolkit for Microsoft Excel. Berkeley, Calif: Berkeley Geochronology Center Special Publication.McDonough, W.F. & Sun, S.S. 1995. The composition of the Earth: Chemical Geology, 120, 3-4, 223-253, doi:10.1016/0009-2541(94)00140-4.

Mavoungo L. N., **Das, K.**, Kawaguchi, K., Hayasaka, Y. and Shibata, T. 2022. Back-arc basin closure at the East Asian margin during Permo-Triassic boundary: Evidence from geochemistry and U-Pb zircon data of sedimentary breccia from Maizuru Terrane, Southwest Japan. Geosystems and Geoenvironment (10.1016/j.geogeo.2022.100080)

McDonough, W. F. and Sun, S. S. 1995. The composition of the earth. Chemical Geology, 120, 223-253.

Meert, J. G., Pandit, M. K., and Kamenov, G. D. 2013. Further geochronological and paleomagnetic constraints on Malani (and pre-Malani) magmatism in NW India: Tectonophysics, v. 608, p. 1254–1267, https://doi.org/10.1016/j.tecto.2013 .06.019.

Middlemost, E. A. K. 1994. Naming Materials in the Magma/Igneous Rock System: Earth Science Review, 37, 215-244.

Nickel, K. G. 1989. Garnet-pyroxene equilibria in the system SMACCr (SiO2-MgO-Al2O3-CaO-Cr2O3): the Crgeobarometer. *Proc. 4th Int. Kimbertite Conf-, Austr. J. Earth Sci.*

Pandit, M. K., Carter, L. M., Ashwal, L. D., Tucker, R. D., Torsvik, T. H., Jamtveit, B. and Bhushan S. K. 2003. Age, petrogenesis and significance of 1Ga granitoids and related rocks from the Sendra area, Aravalli Craton, NW India: Journal of Asian Earth Science, 22, 363-381.

Paton, C., Hellstrom, J., Paul, B., Woodhead, J. and Hergt, J. 2011. Iolite: Freeware for the visualisation and processing of mass spectrometric data: Journal of Analytical Atomic Spectrometry, 26, 12, 2508–2518.

Pearce, J. and Norry, M. 1979. Petrogenetic Implications of Ti, Zr, Y, and Nb Variations in Volcanic Rocks. Contributions to Mineral and Petrology, Vol.69, pp.3-47, ISSN 0010- 7999.

Pearce, J. A. 2008. Geochemical Fingerprinting of Oceanic Basalts with Applications to Ophiolite Classification and the Search for Archean Oceanic Crust: Lithos, 100, 14-48. doi:10.1016/j.lithos.2007.06.016.

Pearce, J. A., Harris, N. B. W. and Tindle, A. G. 1984. Trace Element Discrimination Diagrams for the Tectonic Interpretation of Granitic Rocks: Journal of Petrology, 25: 4, 956–983.

Perfit, M.R., Fornari, D.J., Smith, M. C., Bender, J.F., Langmuir, C.H. and Haymon, R.M. 1994. Small-scale spatial and temporal variations in mid-ocean ridge crest magmatic processes, Geology, 22, 375-379.

Petrus, J. A. and Kamber, B. S. 2012. Vizual Age: A novel approach to laser ablation ICP-MS U-Pb geochronology data reduction: Geostandards and Geoanalytical Research, 36, 247-270, doi:10.1111/j.1751-908X.2012.00158.x.

Rapp, R. P., Watson, E. B. and Miller, C. F. 1991. Partial melting of amphibolite/eclogite and the origin of Archaean trondhjemites and tonalites. Precambrian Research 51, 1–25.

Robinson, J. A. C. and Wood, B. J. 1998. The depth of the spinel to garnet transition at the peridotite solidus. Earth Planet. Sci. Lett. 164, 277–284.

Roy Choudhury, M., Das, S., Chatterjee, S. M. and Sengupta, S. 2016. Deformation of footwall rock of Phulad Shear Zone, Rajasthan: Evidence of transpressional shear zone: Journal of Earth System Science, *125*(5), 1033-1040.

Roy, A. B. and Jakhar, S. R. 2002. Mesoproterozoic Delhi Fold Belts, Geology of Rajasthan (Northwest India) Precambrian to recent India: 205. Jodhpur: Scientific Publishers.

Roy, A. B. and Sharma, K. K. 1999. Geology of the region around Sirohi Town, western Rajasthan-a story of Neoproterozoic evolution of the Aravalli crust. In B. S. Paliwal (Ed.), Geological evolution of the Northwestern India: (pp. 19–33). Jodhpur, India: Scientific Publishers.

Roy, A. B. and Jakhar, S. R. 2002. Geology of Rajasthan (Northwest India) Precambrian to Recent. Jodhpur: Scientific Publishers (India), 421 pp.

Roy, A. B. 1988. Stratigraphic and tectonic framework of the Aravalli Mountain Range, In: A. B. Roy (ed.), Precambrian of the Aravalli Mountain, Rajasthan, India. Mem. Geol. Soc. India, 7, 3-31.

Rudnick, R.L. 1995. Making continental crust. *Nature* 378: 571-578.

Rudnick, R.L. and Gao, S. 2003. The composition of continental crust. In: Rudnick, R.L.
Saccani, E. 2015. A new method of discriminating different types of post-Archean ophiolitic basalts and their tectonic significance using Th-Nb and Ce-Dy-Yb systematics. Geosci. Front. 6, 481–501.

Sengupta, P., Bhui, U. K., Braun, I., Dutta, U. and Mukhopadhyay, D. 2009. Chemical substitutions, paragenetic relations and physical conditions of högbomite in Sittampundi layered anorthosite complex, south India. American Mineralogist 94, 1520–34.

Sengupta, S. and Chatterjee, S. M. 2016. Microstructural variation in quartzofeldspathic mylonites and vorticity analysis using rotating porphyroclasts in Phulad Shear Zone, Rajasthan, India, in Ductile Shear Zones from Micro to Macro-Scales, edited by S. Mukherjee and K. Mulchrone, 128–140, Wiley Blackwell's, London.

Sengupta, S. and Ghosh, S. K. 2004. Analysis of transpressional deformation from geometrical evolution of mesoscopic structures from Phulad shear zone, Rajasthan, India: Journal of Structural Geology, 26, 1961-1976.

Sengupta, S. and Ghosh, S. K. 2007. Origin of striping lineation and transposition of linear structures in shear zones: Journal of Structural Geology, 28, 273-287.

Shand, S. J. 1943. Eruptive Rocks. Their Genesis Composition. Classification, and Their Relation to Ore-Deposits with a Chapter on Meteorite: John Wiley & Sons, New York.

Singh, S., De Waele, B., Shukla, A., Umasankar, B.H. and Biswal, T.K. 2021. Tectonic fabric, geochemistry, and zircon-monazite geochronology as proxies to date an orogeny: Example of South Delhi Orogeny, NW India, and implications for East Gondwana Tectonics. *Frontiers in Earth Science*, *8*, p.594355.

Singh, Y. K., Waele, B. D., Karmakar, S., Sarkar, S., and Biswal, T. K. 2010. Tectonic setting of the Balaram-Kui-Surpagla-Kengora granulites of the South Delhi Terrane of the Aravalli Mobile Belt, NW India and its implication on correlation with the East African Orogen in the Gondwana assembly. *Precambrian Research*, *183*, 669–688.

Sinha Roy, S. 1988. Proterozoic Wilson Cycles in Rajasthan. In: A.B. Roy (cd.) Precambrian of the Aravalli Mountain, Rajasthan, India. *Geological survey of India memorandum, 7*, 95–107.

Sinha-Roy, S., Malhotra, G. and Guha, D. B. 1998. Geology of Rajasthan. Special Publish Geological Society India. Bangalore, *262*.

Sláma, J., Kosler, J., Condon, D.J., Crowley, J.L., Gerdes, A., Hanchar, J.M., Horstwood, M.S.A., Morris, G.A., Nasdala, L., Norberg, N., Schaltegger, U., Schoene, B., Tubrett, M. N. and Whitehouse, M. J. 2008. Plešovice zircon-A new natural reference material for U-Pb and Hf isotopic micro-analysis: Chemical Geology, 249, 1-35.

Sugden, T. J., Deb, M., & Windley, B. F. 1990. The tectonic setting of mineralisation in the Proterozoic Aravalli–Delhi orogenic belt, NW India. In S. M. Naqvi (Ed.), *Precambrian Continental Crust and its Economic Resources* (pp. 367–390). Amsterdam: Elsevier.

Tang, G. J., Chung, S. L., Wang, Q., Wyman, D. A., Dan, W., Chen, H. Y. and Zhao, Z. H. 2014. Petrogenesis of a Late Carboniferous mafic dike–granitoid association in the western Tianshan: response to the geodynamics of oceanic subduction. Lithos 202–203, 85–99

Taylor, S. R. and Mclennan, S. M. 1995. The Geochemical Evolution of the Continental Crust. Reviews in Geophysics, 33, 241-265. https://doi.org/10.1029/95RG00262

Tiwana, J.K., Kaur, P., and Chaudhri, N. 2022. Association of A- and I-type granitoids in the central Aravalli orogen, Rajasthan: Implications for the Neoproterozoic tectonic evolution of north-west India: Geological Journal, v. 57, p. 3267–3291. doi:10.1002/gj.4473.

Tobisch, O. T., Collerson, K. D., Bhattacharya, T. and Mukhopadhyay, D. 1994. Structural relationship and Sm–Nd isotope systematics of polymetamorphic granitic gneisses and granitic rocks from central Rajasthan, India—implications for the evolution of the Aravalli craton: Precambrian Research, 65, 319–339.

Torres-Roldan, R. L., Garcia-Casco, A. and García-Sánchez, P. A. 2000. CSpace: an integrated workplace for the graphical and algebraic analysis of phase assemblages on 32-bit Wintel platforms. Computer Geoscience 26, 779–93. doi: 10.1016/S0098-3004(00)00006-6.

Van Lente, B., Ashwal, L. D., Pandit, M. K., Bowring, S. A. and Torsvik, T. H. 2009. Neoproterozoic hydrothermally altered basaltic rocks from Rajasthan, northwest India: Implications for late Precambrian tectonic evolution of the Aravalli craton. *Precambrian Research*, *170*, 202–222.

Volpe, A. M. and Macdougall, J. D. 1990. Geochemistry and isotopic characteristics of mafic (Phulad ophiolite) and related rocks in the Delhi Supergroup, Rajasthan, India: Implications for rifting in the Proterozoic. *Precambrian Research*, *48*, 167–191.

Wang, W., Pandit, M. K., Zhao, J. H., Chen, W. T. and Zheng, J. P. 2018. Slab break-off triggered lithosphere–asthenosphere interaction at a convergent margin: The Neoproterozoic bimodal magamtism in NW India. *Lithos*, *296–299*, 281–296.

Wang, Y., Yang1, Y. Z., Siebel, W., Zhang, H., Zhang, Y. S. and Chen, F. 2020. Geochemistry and tectonic significance of late Paleoproterozoic A-type granites along the southern margin of the North China Craton: Scientific Report, 10, 86, doi.org/10.1038/s41598-019-56820-1.

Waters, C. L., Sims, K. W. W., Perfit, M. R., Blichert-Toft, J. and Blusztajn, J. 2011. Perspective on the genesis of E-MORB from chemical and isotopic heterogeneity at 9°–10°N East Pacific Rise. Journal of Petrology 52, 565–602.

Wells, P. R. A. 1977. Pyroxene thermometry in simple and complex systems. *Contr. Miner. Petrol.* 62, 129-39

Whalen, J. B. Curie, K. L. and Chappel, B.W. 1987. A-type granites: Geochemical characteristics, discrimination and petrogenesis: Contribution to Mineralogy and Petrology, 95, 407–419.

Whitney, D. L. and Evans, B. W. 2010. Abbreviations for names of rock-forming minerals. American Mineralogist 95, 185–7.

Wood, B. J. and Banno, S. 1973. Garnet-Orthopyroxeneand Orthopyroxene-Clinopyroxene Relationships in Simpleand ComplexSystems. Contribution to Mineralogy and Petrology, 42, 109-124

Zhao, J. H., Pandit, M. K., Wang, W. and Xia, X. P. 2018. Neoproterozoic tectonothermal evolution of NW India: Evidence from geochemistry and geochronology of granitoids: Lithos, 316–317, 330-346.

PUBLICATIONS FROM PRESENT RESEARCH WORK

1. Upama Dutta, Ayan Kumar Sarkar, Sadhana M. Chatterjee, **Anirban Manna**, Alip Roy, and Subhrajyoti Das (2022). Petrological implications of element redistribution during metamorphism: insights from meta-granite of the South Delhi Fold Belt, Rajasthan, India. **Geological Magazine**, 159(5), 735-760. https://doi.org/10.1017/S0016756821001345.

2. Sadhana M. Chatterjee, **Anirban Manna**, Ayan Kumar Sarkar, Alip Roy, Subhrajyoti Das and Upama Dutta (2023). Significance of ~1Ga granites from the South Delhi Fold Belt, NW India: Implication for paleogeographic reconstruction of Rodinia. Journal of Geological society of London (revision submitted)

3. **Anirban Manna**, Sadhana M. Chatterjee, Kaushik Das, Alip Roy and Ayan Kumar Sarkar (2024). Geochemistry and U-Pb zircon geochronology of the gabbroic rocks in the South Delhi Fold Belt: Insights into Rodinia-Age Tectonics in Northwest India. (to be submitted shortly)

OTHER PUBLICATIONS

1. Alip Roy, Sadhana M. Chatterjee, Upama Dutta, Ayan Kumar Sarkar, **Anirban Manna** (2024). Interpretation of multiple reaction textures in quartzo feld spathic rock from south delhi fold belts, rajasthan, india: Constraints from textural modeling and mineral equilibria calculations in ncfmash system. *Geosciences Research Journal (GSRJ), 2(2): 48-54*. **DOI:**10.26480/gsrj.02.2024.48.54

2. **Anirban Manna**, Sadhana M. Chatterjee, Ayan Kumar Sarkar, and Alip Roy (2023). Polyphase deformation in a part of South Delhi Fold Belt, Rajasthan, NW India and its implications. **Journal of scientific research,** 67(3), 18-22. http://dx.doi.org/10.37398/JSR.2023.670303.

3. Ayan Kumar Sarkar, **Anirban Manna**, Sadhana M. Chatterjee, and Alip Roy (2023). Interpretation of deformation microstructures in syn-tectonic granite: insights from Phulad granite, Rajasthan, NW India. **Geosciences Journal**, 27(6), 735-752, doi: 10.1007/s12303023-0028-3.

4. Sadhana M. Chatterjee, Alip Roy, **Anirban Manna**, and Ayan Kumar Sarkar (2023). Early Neoproterozoic tectonics in the Marwar Crustal Block, NW India, the relevance of the Phulad Shear Zone, and implications for Rodinia reconstruction. **Geosphere**, 19(4), 1080–1102, doi: https://doi.org/10.1130/GES02565.1.

5. Sadhana M. Chatterjee, Ayan Kumar Sarkar, Alip Roy, and **Anirban Manna** (2020). Mid-Neoproterozoic tectonics of northwestern India: Evidence of stitching pluton along 810 Ma Phulad Shear Zone. **Tectonics**, 39, e2019TC005902, doi: 10.1029/2019TC005902.

Annexure

Table 1: Representative mineral chemical analysis

Table 1a: Representative mineral chemical analysis of gabbro

Amphibole											
Sample No	**68E**						**63B**				
DataSet/Poi	30 / 1 .	15 / 1 . *	32 / 1 .	35 / 1 .	39 / 1 .	40 / 1 .	4 / 1 .	8 / 1 .	10 / 1 . *	18 / 1 .	20 / 1 .
SiO2	47.40	48.49	50.44	46.95	50.11	50.00	44.84	45.70	43.62	41.96	41.54
TiO2	0.78	0.53	0.43	0.61	0.42	0.33	0.39	0.36	0.19	1.45	1.49
Al2O3	9.06	7.64	5.26	7.92	4.99	3.78	8.86	8.71	11.75	14.08	11.18
Cr2O3	0.17	0.14	0.26	0.05	0.14	0.04	0.04	0.00	0.00	0.20	0.00
MgO	11.94	12.75	13.50	12.69	13.74	14.38	9.76	10.01	8.51	5.78	7.36
FeO	15.12	14.80	12.34	14.40	12.00	12.34	18.77	19.73	19.93	19.83	20.27
CaO	12.05	12.47	15.25	12.04	15.38	13.22	11.37	11.43	11.52	11.05	11.11
MnO	0.19	0.34	0.27	0.20	0.26	0.26	0.20	0.22	0.09	0.17	0.29
Na2O	0.95	0.67	0.56	0.87	0.55	0.39	0.94	0.81	1.11	1.04	1.45
K2O	0.57	0.44	0.30	0.47	0.27	0.29	0.73	0.67	1.06	1.19	1.09
Total	98.22	98.26	98.61	96.18	97.85	95.01	95.90	97.64	97.77	96.74	95.77
Oxygen bas	23.00	23.00	23.00	23.00	23.00	23.00	23.00	23.00	23.00	23.00	23.00
# Si	7.23	7.09	7.64	7.29	7.63	7.84	7.11	7.13	6.78	6.68	6.64
# Ti	0.09	0.06	0.05	0.07	0.05	0.04	0.05	0.04	0.02	0.17	0.18
# Al	1.63	1.32	0.94	1.45	0.90	0.70	1.66	1.60	2.15	2.64	2.11
# Cr	0.02	0.02	0.03	0.01	0.02	0.00	0.00	0.00	0.00	0.02	0.00
# Fe3+	0.00	0.00	0.00	0.00	0.00	0.00	0.00	0.00	0.00	0.00	0.00
# Mg	2.72	2.78	3.05	2.93	3.12	3.36	2.31	2.33	1.97	1.37	1.75
#total Fe	1.93	1.81	1.56	1.87	1.53	1.62	2.49	2.58	2.59	2.64	2.71
# Ca	1.97	1.95	2.47	2.00	2.51	2.22	1.93	1.91	1.92	1.88	1.90
# Mn	0.02	0.04	0.03	0.03	0.03	0.03	0.03	0.03	0.01	0.02	0.04
# Na	0.28	0.19	0.16	0.26	0.16	0.12	0.29	0.25	0.33	0.32	0.45
#K	0.11	0.08	0.06	0.09	0.05	0.06	0.15	0.13	0.21	0.24	0.22
Total	16.00	16.00	16	16	16	16	16	16	16	16	16
Total	Ferro-horn	Mag-hornbl	Mag-hornbl	Ferro-hor	Mag-horn	Mag-horn	Ferro-hor	Ferro-horn	Ferro-horn	Ferro-tsch	Ferro-pargasite

	63B				63b		68e			
	Opx				Cpx					
DataSet/Poi	1 / 1 .	14 / 1 . *	2 / 1 .	6 / 1 .	23 / 1 .	24 / 1 .	38 / 1 .	1 / 1 . *	41 / 1 .	42 / 1 .
SiO2	50.42	50.09	49.16	49.29	51.92	51.54	52.82	52.55	51.88	53.25
TiO2	0.02	0.00	0.02	0.03	0.04	0.00	0.07	0.07	0.26	0.08
Al2O3	0.44	0.47	0.44	0.53	0.73	0.74	0.81	0.94	2.55	1.05
Cr2O3	0.00	0.00	0.00	0.01	0.00	0.11	0.15	0.16	0.46	0.11
MgO	13.55	13.34	13.69	13.53	10.60	10.52	13.12	13.20	13.42	13.43
FeO	34.31	35.72	33.61	32.67	14.09	13.48	8.45	8.97	9.82	9.00
CaO	1.39	0.44	0.44	1.68	22.16	22.10	23.60	23.07	20.19	23.11
MnO	1.38	0.95	1.28	1.13	0.52	0.76	0.45	0.45	0.53	0.49
Na2O	0.05	0.02	0.03	0.02	0.25	0.26	0.26	0.35	0.44	0.24
K2O	0.00	0.00	0.00	0.00	0.00	0.00	0.00	0.07	0.09	0.01
Total	101.56	101.05	98.68	98.89	100.31	99.50	99.73	99.81	99.70	100.80
# Si	1.97	1.97	1.98	1.97	1.98	1.98	1.98	1.97	1.94	1.97
# Ti	0.00	0.00	0.00	0.00	0.00	0.00	0.00	0.00	0.01	0.00
# Al	0.02	0.02	0.02	0.03	0.03	0.03	0.04	0.04	0.11	0.05
# Cr	0.00	0.00	0.00	0.00	0.00	0.00	0.00	0.00	0.01	0.00
# Mg	0.79	0.78	0.82	0.81	0.60	0.60	0.73	0.74	0.75	0.74
# Fe	1.12	1.17	1.13	1.09	0.45	0.43	0.27	0.28	0.31	0.28
# Ca	0.06	0.02	0.02	0.07	0.91	0.91	0.95	0.93	0.81	0.92
# Mn	0.05	0.03	0.04	0.04	0.02	0.02	0.01	0.01	0.02	0.02
# Na	0.00	0.00	0.00	0.00	0.02	0.02	0.02	0.03	0.03	0.02
#K	0.00	0.00	0.00	0.00	0.00	0.00	0.00	0.00	0.00	0.00

	68e						63b				
	Plagioclase										
DataSet/Poi	34 / 1 .	14 / 1 . *	17 / 1 . *	43 / 1 .	44 / 1 .	54 / 1 .	1 / 1 .	2 / 1 .	11 / 1 . *	8 / 1 .	9 / 1 .
SiO2	52.87	52.15	55.31	54.15	54.97	51.98	57.75	57.10	55.50	54.10	54.71
TiO2	0.07	0.01	0.04	0.00	0.00	0.00	-0.02	-0.01	0.02	0.04	0.03
Al2O3	28.71	29.91	27.12	28.58	27.92	29.03	27.69	26.84	27.26	29.39	28.82
Cr2O3	0.00	0.04	0.05	0.00	0.00	0.02	-0.03	-0.03	0.00	-0.02	0.01
MgO	0.03	0.01	0.00	0.00	0.00	0.00	0.01	0.01	0.11	0.04	0.01
FeO	0.10	0.29	0.00	0.01	0.14	0.09	0.00	0.36	0.50	0.46	0.06
CaO	12.05	13.10	10.42	11.45	10.65	12.47	8.70	8.22	9.86	11.10	10.78
MnO	0.00	0.00	0.04	0.00	0.04	0.01	-0.06	0.02	0.06	0.04	-0.10
Na2O	5.02	4.34	5.99	5.28	5.48	4.67	6.39	6.60	5.70	5.39	5.63
K2O	0.08	0.09	0.12	0.05	0.08	0.07	0.18	0.20	0.40	0.17	0.11
Total	98.93	99.93	99.08	99.62	99.27	98.34	100.63	99.33	99.43	100.74	100.07
# Si	2.42	2.37	2.52	2.46	2.50	2.40	2.57	2.58	2.51	2.43	2.47
# Ti	0.00	0.00	0.00	0.00	0.00	0.00	0.00	0.00	0.00	0.00	0.00
# Al	1.55	1.60	1.46	1.53	1.49	1.58	1.45	1.43	1.45	1.56	1.53
# Cr	0.00	0.00	0.00	0.00	0.00	0.00	0.00	0.00	0.00	0.00	0.00
# Mg	0.00	0.00	0.00	0.00	0.00	0.00	0.00	0.00	0.01	0.00	0.00
# Fe	0.00	0.01	0.00	0.00	0.01	0.00	0.00	0.01	0.02	0.02	0.00
# Ca	0.59	0.64	0.51	0.56	0.52	0.62	0.41	0.40	0.48	0.53	0.52
# Mn	0.00	0.00	0.00	0.00	0.00	0.00	0.00	0.00	0.00	0.00	0.00
# Na	0.45	0.38	0.53	0.46	0.48	0.42	0.55	0.58	0.50	0.47	0.49
#K	0.00	0.00	0.01	0.00	0.00	0.00	0.01	0.01	0.02	0.01	0.01

	63b			63b			68e			
	Grt			Ilm					Sphene	
DataSet/Poi	9 / 1 . *	12 / 1 .	15 / 1 .	113	114	116	8 / 1 . *	28 / 1 .	9 / 1 . *	29 / 1 .
SiO2	36.98	36.78	37.64	0.22	0.01	0.04	0.06	0.03	30.61	30.65
TiO2	0.00	0.01	0.00	51.29	53.88	53.45	52.51	52.21	39.32	38.65
Al2O3	20.74	20.95	21.32	0.07	0.01	0.00	0.12	0.15	0.84	1.02
Cr2O3	0.06	0.06	0.00	0.00	0.09	0.02	0.22	0.22	0.00	0.01
MgO	2.20	2.64	2.84	0.06	0.40	0.34	0.62	0.56	0.01	0.00
FeO	31.53	30.61	30.77	43.65	45.23	45.47	44.10	44.59	0.23	0.20
CaO	6.28	6.50	6.75	0.44	0.03	0.10	0.04	0.02	29.39	28.43
MnO	2.58	1.95	1.79	2.02	0.77	0.93	2.01	1.93	0.12	0.05
Na2O	0.05	0.00	0.02	0.00	0.00	0.06	0.00	0.05	0.00	0.01
K2O	0.00	0.02	0.00	0.01	0.00	0.00	0.01	0.02	0.00	0.00
Total	100.46	99.51	101.16	97.86	100.59	100.49	99.70	99.77	100.53	99.02
# Si	2.97	2.97	2.98	0.01	0.00	0.00	0.00	0.00	1.00	1.01
# Ti	0.00	0.00	0.00	0.99	1.01	1.01	0.99	0.99	0.96	0.96
# Al	1.96	1.99	1.99	0.00	0.00	0.00	0.00	0.00	0.03	0.04
# Cr	0.00	0.00	0.00	0.00	0.00	0.00	0.00	0.00	0.00	0.00
# Mg	0.26	0.32	0.34	0.00	0.01	0.01	0.02	0.02	0.00	0.00
# Fe	2.12	2.06	2.04	0.94	0.94	0.95	0.93	0.94	0.01	0.01
# Ca	0.54	0.56	0.57	0.01	0.00	0.00	0.00	0.00	1.02	1.00
# Mn	0.18	0.13	0.12	0.04	0.02	0.02	0.04	0.04	0.00	0.00
# Na	0.01	0.00	0.00	0.00	0.00	0.00	0.00	0.00	0.00	0.00
#K	0	0.00	0	0.00	0	5E-05	0.00	0.00	0	0

Table 1b: Representative mineral chemical analysis of granites														
Amphibole														
Sample No	**P-491**			**P-106**			**P- 225b z**				**P-104**	**P- 245a z.**	**P-199**	
DataSet/Point	70 / 1 .	59 / 1 .	61 / 1 .	1 / 1 .	2 / 1 .	8 / 1 .	6*	18	19	68 / 1 .	97 / 1 .	74 / 1 .	79 / 1 .	80 / 1 .
SiO2	38.46	36.64	36.69	39.62	38.52	39.85	38.21	36.82	37.28	37.28	36.17	37.93	37.18	37.43
TiO2	0.68	0.50	0.46	1.14	1.01	1.06	0.77	0.22	0.47	0.48	0.49	0.43	0.43	0.58
Al2O3	11.75	13.50	13.67	12.94	13.15	13.65	11.48	13.60	13.42	12.64	12.57	12.16	13.02	13.20
Cr2O3	0.00	0.00	0.01	0.00	0.05	0.03	0.02	0.00	0.11	0.02	0.03	0.01	0.01	0.00
FeO	31.62	30.18	30.22	25.22	25.65	25.67	30.30	29.76	30.53	30.07	30.73	31.17	31.49	30.78
MnO	0.72	0.83	0.60	0.31	0.41	0.34	0.76	0.77	0.75	0.66	0.85	0.94	0.79	0.71
NiO	0.00	0.00	0.00	0.00	0.00	0.00	0.00	0.00	0.00	0.00	0.00	0.00	0.00	0.00
MgO	1.24	1.03	0.98	4.33	3.95	4.30	1.37	1.40	1.41	1.20	0.81	1.00	1.03	0.92
CaO	10.69	11.00	11.05	11.52	11.42	11.52	10.55	10.10	10.32	10.80	10.58	10.60	10.84	10.71
BaO	0.07	0.00	0.00	0.00	0.02	0.00	0.00	0.00	0.00	0.00	0.00	0.01	0.00	0.08
Na2O	1.40	1.19	1.21	1.25	1.18	1.14	1.34	1.30	1.21	1.23	1.35	1.44	1.35	1.34
K2O	1.87	1.95	1.96	1.94	2.02	1.99	2.01	2.02	1.87	1.89	2.13	1.84	2.00	2.05
P2O5	0.00	0.03	0.00	0.07	0.01	0.07	0.12	0.24	0.17	0.15	0.05	0.19	0.08	0.10
Total	98.50	96.86	96.85	98.34	97.38	99.61	96.93	96.23	97.54	96.42	95.76	97.72	98.22	97.9
Oxygen basis	23	23	23	23	23	23	23	23	23	23	23	23	23	23
Si	6.16	5.94	5.95	6.18	6.08	6.12	6.22	6.10	5.97	6.08	5.98	6.13	5.97	6.03
Al (IV)	1.84	2.06	2.05	1.82	1.92	1.88	1.78	1.90	2.03	1.92	2.02	1.87	2.03	1.97
Ti	0.00	0.00	0.00	0.00	0.00	0.00	0.00	0.00	0.00	0.00	0.00	0.00	0.00	0.00
Sum T	8.00	8.00	8.00	8.00	8.00	8.00	8.00	8.00	8.00	8.00	8.00	8.00	8.00	8.00
Al (VI)	0.37	0.52	0.56	0.56	0.53	0.60	0.42	0.25	0.51	0.51	0.43	0.44	0.43	0.54
Ti	0.08	0.06	0.06	0.13	0.12	0.12	0.09	0.09	0.06	0.06	0.06	0.05	0.05	0.07
Cr +3	0.00	0.00	0.00	0.00	0.01	0.00	0.00	0.02	0.01	0.00	0.00	0.00	0.00	0.00
Fe +3	0.67	0.73	0.68	0.30	0.44	0.41	0.51	0.76	0.88	0.63	0.72	0.67	0.81	0.62
Mg	0.30	0.25	0.24	1.01	0.93	0.98	0.33	0.35	0.34	0.29	0.20	0.24	0.25	0.22
Fe +2	3.56	3.37	3.42	2.99	2.95	2.88	3.62	3.51	3.21	3.47	3.53	3.54	3.41	3.53
Mn	0.02	0.07	0.04	0.01	0.02	0.00	0.03	0.03	0.00	0.04	0.06	0.05	0.04	0.03

Amphibole														
Sample No	**P-491**			**P-106**			**P- 225b z**				**P-104**	**P- 245a z.**	**P-199**	
Li	0.00	0.00	0.00	0.00	0.00	0.00	0.00	0.00	0.00	0.00	0.00	0.00	0.00	0.00
Sum C	5.00	5.00	5.00	5.00	5.00	5.00	5.00	5.00	5.00	5.00	5.00	5.00	5.00	5.00
Mg	0.00	0.00	0.00	0.00	0.00	0.00	0.00	0.00	0.00	0.00	0.00	0.00	0.00	0.00
Fe +2	0.00	0.00	0.00	0.00	0.00	0.00	0.00	0.00	0.01	0.00	0.00	0.00	0.00	0.00
Mn	0.08	0.04	0.04	0.03	0.03	0.04	0.08	0.09	0.10	0.05	0.06	0.08	0.06	0.07
Li	0.00	0.00	0.00	0.00	0.00	0.00	0.00	0.00	0.00	0.00	0.00	0.00	0.00	0.00
Ca	1.83	1.91	1.92	1.93	1.93	1.90	1.84	1.82	1.77	1.89	1.87	1.83	1.86	1.85
Na	0.09	0.05	0.04	0.04	0.04	0.06	0.09	0.10	0.12	0.06	0.07	0.09	0.07	0.08
Sum B	2.00	2.00	2.00	2.00	2.00	2.00	2.00	2.00	2.00	2.00	2.00	2.00	2.00	2.00
Ca	0.00	0.00	0.00	0.00	0.00	0.00	0.00	0.00	0.00	0.00	0.00	0.00	0.00	0.00
Na	0.35	0.33	0.34	0.34	0.32	0.28	0.34	0.39	0.25	0.33	0.37	0.36	0.35	0.34
K	0.38	0.40	0.41	0.39	0.41	0.39	0.42	0.41	0.38	0.39	0.45	0.38	0.41	0.42
Sum A	0.73	0.73	0.74	0.72	0.73	0.67	0.75	0.80	0.64	0.72	0.81	0.74	0.76	0.76
Total	15.73	15.73	15.74	15.72	15.73	15.67	15.75	15.80	15.64	15.72	15.81	15.74	15.76	15.76
Groups	CG	CG	CG	CG	CG	CG	CG	CG	CG	CG	CG	CG	CG	CG
Name	HG	HG	HG	FP	FP	FP	HG	HG	HG	HG	HG	HG	HG	HG

CG=Calcic Group FP=Ferropargasite MH=Magnesiohastingsite HG=Hastingsite

Biotite														
Sample No	**P- 225 bz**				**P-106**		**P- 104**		**P- 245 a Z**	**M21**	**P-491**			
DataSet/Poin	7 / 1 .	8 / 1 .	36 / 1 .	39 / 1 .	45 / 1 .	49 / 1 .	64/ 1 .	73 / 1 .	96 / 1 .	60 / 1 .	25 / 1 .	28 / 1 .	49 / 1 .	50 / 1 .
SiO2	33.05	32.82	33.55	32.66	34.51	34.45	32.23	32.65	33.53	34.39	33.40	33.02	32.35	33.20
TiO2	2.09	2.07	2.08	1.90	3.28	3.65	1.75	1.97	2.18	3.23	2.63	2.29	2.51	2.51
Al2O3	14.84	15.35	15.67	14.97	15.47	15.44	15.35	15.79	15.57	15.97	15.31	15.28	14.83	15.14
Cr2O3	0.06	0.13	0.00	0.00	0.00	0.18	0.45	0.18	0.00	0.00	0.00	0.00	0.00	0.01
FeO	30.99	32.07	32.75	32.53	27.26	27.12	32.19	32.74	31.53	30.37	33.18	31.65	31.96	32.02
MnO	0.62	0.66	0.56	0.56	0.26	0.38	0.58	0.53	0.56	0.41	0.59	0.57	0.69	0.58
NiO	0.00	0.00	0.00	0.00	0.00	0.00	0.00	0.00	0.00	0.00	0.00	0.00	0.00	0.00
MgO	2.94	2.42	2.44	2.61	5.80	5.86	2.22	1.94	1.62	1.71	1.77	1.89	1.83	1.77
CaO	0.09	0.14	0.09	0.11	0.00	0.00	0.36	0.04	0.17	0.05	0.01	0.15	0.04	0.05
BaO	0.11	0.00	0.17	0.12	0.00	0.00	0.00	0.00	0.00	0.05	0.11	0.08	0.03	0.03
Na2O	0.32	0.21	0.11	0.12	0.14	0.09	0.13	0.19	0.19	0.15	0.03	0.07	0.05	0.03
K2O	8.94	8.72	8.97	9.02	9.53	9.48	8.22	9.10	8.72	9.12	8.82	8.25	8.81	8.94
P2O5	0.05	0.00	0.00	0.01	0.00	0.00	0.00	0.00	0.00	0.00	0.02	0.01	0.01	0.00
Total	94.1	94.59	96.39	94.61	96.25	96.65	93.48	95.13	94.07	95.45	95.85	93.26	93.10	94.28
Oxygen basis	22	22	22	22	22	22	22	22	22	22	22	22	22	22
Si4+	5.48	5.43	5.45	5.43	5.45	5.42	5.40	5.39	5.54	5.55	5.46	5.51	5.45	5.51
Ti4+	0.26	0.26	0.25	0.24	0.39	0.43	0.22	0.24	0.27	0.39	0.32	0.29	0.32	0.31
Al3+	2.90	2.99	3.00	2.94	2.88	2.86	3.03	3.08	3.03	3.04	2.95	3.01	2.95	2.96
Cr3+	0.01	0.02	0.00	0.00	0.00	0.02	0.06	0.02	0.00	0.00	0.00	0.00	0.00	0.00
Fe2+	4.30	4.44	4.45	4.52	3.60	3.57	4.51	4.52	4.36	4.10	4.54	4.42	4.51	4.44
Mn2+	0.09	0.09	0.08	0.08	0.03	0.05	0.08	0.07	0.08	0.06	0.08	0.08	0.10	0.08
Ni2+	0.00	0.00	0.00	0.00	0.00	0.00	0.00	0.00	0.00	0.00	0.00	0.00	0.00	0.00
Mg2+	0.73	0.60	0.59	0.65	1.37	1.37	0.55	0.48	0.40	0.41	0.43	0.47	0.46	0.44
Ca2+	0.02	0.02	0.02	0.02	0.00	0.00	0.06	0.01	0.03	0.01	0.00	0.03	0.01	0.01
Ba2+	0.01	0.00	0.01	0.01	0.00	0.00	0.00	0.00	0.00	0.00	0.01	0.01	0.00	0.00
Na+	0.10	0.07	0.03	0.04	0.04	0.03	0.04	0.06	0.06	0.05	0.01	0.02	0.02	0.01
K+	1.89	1.84	1.86	1.91	1.92	1.90	1.76	1.92	1.84	1.88	1.84	1.76	1.90	1.89
P5+	0.01	0.00	0.00	0.00	0.00	0.00	0.00	0.00	0.00	0.00	0.00	0.00	0.00	0.00
Total	15.79	15.76	15.74	15.84	15.70	15.67	15.73	15.80	15.62	15.50	15.66	15.58	15.71	15.65

Feldspar															
Sample No	**P-106**		**M-21**	**P-472**	**P-491**					**P-225bz**					
	Plag	Plag	K-flds	K-flds	K-flds	Plag	K-flds	Plag	Plag	Plag	Plag	Plag	K-flds	K-flds
DataSet/Poin	3 / 1 .	6 / 1 .	59 / 1 .	37 / 1 .	52 / 1 .	53 / 1 .	55 / 1 .	8 / 1 .	63 / 1 .	22 / 1 .	3*	25 / 1 .	26 / 1 .	28 / 1 .
SiO2	60.65	58.71	64.98	64.06	62.81	64.93	63.22	69.51	65.98	67.99	65.58	67.93	63.98	62.47
TiO2	0.00	0.00	0.00	0.02	0.01	0.01	0.01	0.00	0.00	0.00	0.00	0.00	0.00	0.01
Al2O3	23.67	24.91	18.13	18.24	17.76	21.66	17.79	20.25	19.12	19.42	21.56	19.48	18.09	17.82
Cr2O3	0.00	0.05	0.00	0.09	0.00	0.06	0.00	0.01	0.08	0.00	0.00	0.03	0.06	0.04
FeO	0.12	0.42	0.10	0.21	0.06	0.26	0.13	0.11	0.35	0.15	0.09	0.00	0.04	1.04
MnO	0.00	0.17	0.00	0.00	0.07	0.01	0.04	0.06	0.00	0.01	0.00	0.00	0.00	0.00
MgO	0.00	0.00	0.01	0.00	0.00	0.00	0.00	0.01	0.00	0.00	0.03	0.00	0.00	0.10
CaO	6.01	7.35	0.00	0.00	0.00	3.23	0.00	0.50	0.71	0.64	2.42	0.26	0.00	0.00
BaO	0.11	0.00	0.18	0.15	0.40	0.00	0.63	0.04	0.00	0.00	0.00	0.00	0.00	0.00
Na2O	5.74	7.33	0.57	0.03	0.77	10.38	0.77	12.04	11.54	10.81	10.13	11.72	0.74	0.82
K2O	3.92	0.15	15.68	16.31	15.76	0.12	15.48	0.05	0.07	0.04	0.17	0.25	16.40	15.40
P2O5	0.00	0.02	0.00	0.00	0.00	0.00	0.00	0.00	0.03	0.07	0.00	0.07	0.08	0.06
Total	100.22	99.10	99.64	99.11	97.62	100.66	98.08	102.58	97.88	99.14	99.98	99.8	99.39	97.84
Oxygen basis	8	8	8	8	8	8	8	8	8	8	8	8	8	8
Si4+	2.73	2.65	3.01	2.99	2.99	2.85	2.99	2.97	2.96	2.99	2.88	2.98	2.99	2.97
Ti4+	0.00	0.00	0.00	0.00	0.00	0.00	0.00	0.00	0.00	0.00	0.00	0.00	0.00	0.00
Al3+	1.26	1.33	0.99	1.01	1.00	1.12	0.99	1.02	1.01	1.01	1.12	1.01	1.00	1.00
Cr3+	0.00	0.00	0.00	0.00	0.00	0.00	0.00	0.00	0.00	0.00	0.00	0.00	0.00	0.00
Fe2+	0.00	0.02	0.00	0.01	0.00	0.01	0.01	0.00	0.01	0.01	0.00	0.00	0.00	0.04
Mn2+	0.00	0.01	0.00	0.00	0.00	0.00	0.00	0.00	0.00	0.00	0.00	0.00	0.00	0.00
Ni2+	0.00	0.00	0.00	0.00	0.00	0.00	0.00	0.00	0.00	0.00	0.00	0.00	0.00	0.00
Mg2+	0.00	0.00	0.00	0.00	0.00	0.00	0.00	0.00	0.00	0.00	0.00	0.00	0.00	0.01
Ca2+	0.29	0.36	0.00	0.00	0.00	0.15	0.00	0.02	0.03	0.03	0.11	0.01	0.00	0.00
Ba2+	0.00	0.00	0.00	0.00	0.01	0.00	0.01	0.00	0.00	0.00	0.00	0.00	0.00	0.00
Na+	0.50	0.64	0.05	0.00	0.07	0.88	0.07	1.00	1.00	0.92	0.93	1.00	0.07	0.08
K+	0.22	0.01	0.93	0.97	0.96	0.01	0.93	0.00	0.00	0.00	0.00	0.01	0.98	0.93
P5+	0.00	0.00	0.00	0.00	0.00	0.00	0.00	0.00	0.00	0.00	0.00	0.00	0.00	0.00
Total	5.01	5.01	4.98	4.99	5.03	5.03	5.01	5.02	5.03	4.96	5.05	5.02	5.03	5.03

Plag=Plagioclase K-flds=K-feldspar

Garnet														
Sample No	**P-106**		**P-104**		**P-225bz**		**P-199**		**P-491**					**P-472**
DataSet/Point	22 / 1 .	23 / 1 .	57 / 1 .	58 / 1 .	14*	1	77 / 1 .	78 / 1 .	1 / 1 .	23 / 1 .	24 / 1 .	31 / 1 .	32 / 1 .	42 / 1 .
SiO2	36.09	36.28	36.67	36.91	36.82	36.58	36.99	36.47	36.74	37.08	37.41	37.05	37.05	36.64
TiO2	0.02	0.19	0.15	0.00	0.04	0.09	0.04	0.01	0.08	0.03	0.05	0.06	0.07	0.04
Al2O3	20.00	20.61	19.92	19.98	20.12	20.18	20.25	20.31	20.48	20.76	20.76	20.87	20.69	20.67
Cr2O3	0.02	0.01	0.00	0.00	0.00	0.05	0.00	0.00	0.09	0.00	0.08	0.01	0.00	0.00
Fe2O3	1.92	1.18	1.52	1.40	1.21	1.35	1.30	1.39	0.54	0.65	0.68	0.04	0.99	0.43
FeO	23.03	23.11	21.49	21.61	18.17	18.65	20.99	20.78	17.96	20.17	20.33	22.21	20.58	19.39
MnO	6.23	6.33	10.81	10.96	10.90	12.25	11.38	11.17	13.35	11.37	11.05	12.46	11.59	11.95
MgO	0.68	0.72	0.16	0.13	0.08	0.11	0.00	0.00	0.04	0.10	0.07	0.13	0.09	0.00
CaO	11.33	11.12	9.41	9.23	11.91	10.63	9.77	10.04	9.97	10.18	10.55	7.20	9.97	9.99
Total	99.32	99.55	100.13	100.22	99.32	99.90	100.72	100.17	99.26	100.35	100.97	100.03	101.03	99.11
Oxygen basis	12	12	12	12	12	12	12	12	12	12	12	12	12	12
Si	2.94	2.94	2.97	2.99	2.99	2.96	2.98	2.96	2.99	2.98	2.99	3.00	2.97	2.98
Al iv	0.06	0.06	0.03	0.01	0.01	0.04	0.02	0.04	0.01	0.02	0.01	0.00	0.03	0.02
Al vi	1.86	1.91	1.89	1.90	1.91	1.90	1.91	1.90	1.95	1.95	1.95	1.99	1.93	1.97
Ti	0.00	0.01	0.01	0.00	0.00	0.01	0.00	0.00	0.00	0.00	0.00	0.00	0.00	0.00
Cr	0.00	0.00	0.00	0.00	0.00	0.00	0.00	0.00	0.01	0.00	0.00	0.00	0.00	0.00
Fe3+	0.12	0.07	0.09	0.09	0.07	0.08	0.08	0.08	0.03	0.04	0.04	0.00	0.06	0.03
Fe2+	1.57	1.56	1.46	1.46	1.23	1.26	1.41	1.41	1.22	1.36	1.36	1.50	1.38	1.32
Mn	0.43	0.43	0.74	0.75	0.75	0.84	0.78	0.77	0.92	0.77	0.75	0.85	0.79	0.82
Mg	0.08	0.09	0.02	0.02	0.01	0.01	0.00	0.00	0.00	0.01	0.01	0.02	0.01	0.00
Ni	0.00	0.00	0.00	0.00	0.00	0.00	0.00	0.00	0.00	0.00	0.00	0.00	0.00	0.00
Zn	0.00	0.00	0.00	0.00	0.00	0.00	0.00	0.00	0.00	0.00	0.00	0.00	0.00	0.00
Ca	0.99	0.96	0.82	0.80	1.03	0.92	0.84	0.87	0.87	0.88	0.90	0.62	0.86	0.87
Total	8.05	8.04	8.03	8.02	8.02	8.03	8.02	8.04	8.01	8.02	8.01	8.00	8.02	8.01
Almandine	48.93	49.42	46.88	47.53	39.94	40.05	45.64	44.56	39.97	44.22	44.49	50.06	44.32	43.16
Andradite	6.00	3.66	4.69	4.29	3.72	4.18	3.97	4.30	1.65	1.98	2.04	0.13	3.02	1.32
Grossular	27.57	29.15	22.81	22.50	30.94	26.80	24.33	25.20	27.14	27.44	27.92	20.70	25.81	27.90
Pyrope	2.81	2.96	0.65	0.53	0.32	0.45	0.00	0.00	0.17	0.38	0.27	0.52	0.35	0.00
Spessartine	14.62	14.78	24.97	25.15	25.08	28.37	26.06	25.94	30.79	25.98	25.03	28.56	26.50	27.62

Titanite														
Sample no	**P-472**						**P-225bz**				**P-106**	**P-491**		
DataSet/Poi	35 / 1 .	36 / 1 .	40 / 1 .	41 / 1 .	46 / 1 .	47 / 1 .	15 / 1 .	37 / 1 . *	58 / 1 .	66 / 1 . *	17 / 1 .	9 / 1 .	18 / 1 .	26 / 1 .
SiO2	29.45	31.02	29.83	28.90	28.57	28.56	30.15	30.82	30.29	30.05	30.85	30.24	31.12	31.24
TiO2	28.67	27.75	30.96	29.52	30.13	30.54	27.79	29.20	29.45	29.81	36.30	25.71	26.11	26.68
Al2O3	5.45	8.20	4.77	4.91	4.82	4.63	8.15	5.62	5.55	5.06	2.59	8.83	9.25	9.07
Cr2O3	0.04	0.06	0.00	0.05	0.00	0.00	0.17	0.00	0.08	0.00	0.00	0.00	0.00	0.00
FeO	2.44	1.30	1.91	2.62	3.08	2.90	1.01	1.99	2.22	2.52	1.20	1.43	1.01	0.83
MnO	0.34	0.01	0.23	0.32	0.27	0.35	0.25	0.29	0.28	0.23	0.20	0.18	0.11	0.28
MgO	0.07	0.00	0.00	0.03	0.02	0.01	0.00	0.01	0.09	0.06	0.00	0.03	0.01	0.00
CaO	25.23	28.84	26.99	25.44	26.20	26.04	28.38	26.03	25.21	24.50	28.26	27.52	28.58	28.69
BaO	0.00	0.00	0.00	0.00	0.00	0.00	0.00	0.00	0.00	0.00	0.00	0.00	0.00	0.00
Na2O	0.13	0.02	0.06	0.10	0.07	0.12	0.08	0.07	0.05	0.07	0.01	0.05	0.00	0.03
K2O	0.00	0.00	0.00	0.00	0.00	0.01	0.02	0.00	0.02	0.01	0.01	0.00	0.04	0.00
P2O5	0.00	0.00	0.00	0.00	0.00	0.00	0.21	0.47	0.37	0.38	0.00	0.00	0.00	0.00
Total	92.00	97.38	95.03	92.00	93.43	93.41	96.20	94.51	93.61	92.69	99.85	94.15	96.33	97.08
Oxygen basis	5	5	5	5	5	5	5	5	5	5	5	5	5	5
Si4+	1.04	1.03	1.03	1.03	1.01	1.01	1.01	1.05	1.04	1.04	1.01	1.04	1.04	1.04
Ti4+	0.76	0.69	0.80	0.79	0.80	0.81	0.70	0.75	0.76	0.78	0.90	0.66	0.66	0.67
Al3+	0.23	0.32	0.19	0.21	0.20	0.19	0.32	0.23	0.22	0.21	0.10	0.36	0.36	0.36
Cr3+	0.00	0.00	0.00	0.00	0.00	0.00	0.00	0.00	0.00	0.00	0.00	0.00	0.00	0.00
Fe3+	0.00	0.00	0.00	0.00	0.00	0.00	0.03	0.05	0.06	0.07	0.03	0.04	0.03	0.02
Mn2+	0.01	0.00	0.01	0.01	0.01	0.01	0.01	0.01	0.01	0.01	0.01	0.01	0.00	0.01
Mg2+	0.00	0.00	0.00	0.00	0.00	0.00	0.00	0.00	0.00	0.00	0.00	0.00	0.00	0.00
Ca2+	0.96	1.03	0.99	0.97	0.99	0.98	1.02	0.95	0.93	0.91	0.99	1.01	1.02	1.02
Ba2+	0.00	0.00	0.00	0.00	0.00	0.00	0.00	0.00	0.00	0.00	0.00	0.00	0.00	0.00
Na+	0.01	0.00	0.00	0.01	0.00	0.01	0.01	0.00	0.00	0.00	0.00	0.00	0.00	0.00
K+	0.00	0.00	0.00	0.00	0.00	0.00	0.00	0.00	0.00	0.00	0.00	0.00	0.00	0.00
P5+	0.00	0.00	0.00	0.00	0.00	0.00	0.01	0.01	0.01	0.01	0.00	0.00	0.00	0.00
Total	3.01	3.08	3.02	3.01	3.01	3.01	3.10	3.05	3.04	3.03	3.05	0.00	0.00	0.00

Magnetite									
Sample no	**M-21**	**P-472**			**P-225bz**				
DataSet/Poin	58 / 1 .	39 / 1 .	45 / 1 .	48 / 1 .	34 / 1 .	36 / 1 .	49 / 1 .	52 / 1 .	59 / 1 . *
SiO2	0.10	0.01	0.00	0.02	0.06	0.04	0.04	0.26	0.16
TiO2	0.03	0.09	0.11	0.13	0.13	0.55	0.47	0.18	0.21
Al2O3	0.05	0.09	0.12	0.17	0.09	0.28	0.36	0.36	0.09
Cr2O3	0.02	0.00	0.06	0.05	0.00	0.01	0.00	0.00	0.00
FeO	92.22	91.43	92.50	94.32	94.68	94.48	93.23	92.65	93.73
MnO	0.02	0.10	0.16	0.02	0.22	0.19	0.00	0.62	0.08
NiO	0.00	0.00	0.00	0.00	0.05	0.24	0.16	0.13	0.00
MgO	0.06	0.06	0.02	0.06	0.00	0.01	0.08	0.00	0.02
CaO	0.02	0.00	0.02	0.04	0.00	0.00	0.02	0.25	0.21
BaO	0.00	0.00	0.00	0.00	0.00	0.00	0.00	0.00	0.00
Na2O	0.04	0.00	0.02	0.00	0.00	0.00	0.06	0.00	0.02
K2O	0.03	0.00	0.01	0.00	0.02	0.00	0.06	0.00	0.00
P2O5	0.00	0.00	0.00	0.00	0.00	0.00	0.04	0.00	0.01
Total	92.58	91.79	93.05	94.82	95.24	95.8	94.53	94.44	94.53
Oxygen basis	4	4	4	4	4	4	4	4	4
Si4+	0.00	0.00	0.00	0.00	0.00	0.00	0.00	0.01	0.01
Ti4+	0.00	0.00	0.00	0.00	0.00	0.02	0.01	0.01	0.01
Al3+	0.00	0.00	0.01	0.01	0.00	0.01	0.02	0.02	0.00
Cr	0.00	0.00	0.00	0.00	0.00	0.00	0.00	0.00	0.00
Fe+3	2.99	2.99	2.98	2.98	2.65	2.62	2.62	2.61	2.64
Mn2+	0.00	0.00	0.01	0.00	0.01	0.01	0.00	0.02	0.00
Ni2+	0.00	0.00	0.00	0.00	0.00	0.01	0.00	0.00	0.00
Mg2+	0.00	0.00	0.00	0.00	0.00	0.00	0.00	0.00	0.00
Ca2+	0.00	0.00	0.00	0.00	0.00	0.00	0.00	0.01	0.01
Ba2+	0.00	0.00	0.00	0.00	0.00	0.00	0.00	0.00	0.00
Na2+	0.00	0.00	0.00	0.00	0.00	0.00	0.00	0.00	0.00
K+	0.00	0.00	0.00	0.00	0.00	0.00	0.00	0.00	0.00
P5+	0.00	0.00	0.00	0.00	0.00	0.00	0.00	0.00	0.00
Total	8.34	5.34	5.33	5.34	2.67	2.67	2.67	2.67	2.67

Ilmenite		
Sample n	**P-225bz**	
DataSet/P	33 / 1 .	35 / 1 . *
SiO2	0.00	0.02
TiO2	49.82	49.57
Al2O3	0.00	0.03
Fe2O3(T)	0.00	0.00
FeO(T)	43.76	43.54
MnO	5.90	5.97
MgO	0.03	0.00
CaO	0.00	0.00
Na2O	0.05	0.05
K2O	0.00	0.00
Cr2O3	0.02	0.00
BaO	0.00	0.00
ZnO	0.00	0.00
Total	99.58	99.18
Oxygen bas	3	3
Si	0.00	0.00
Ti	0.95	0.95
Al	0.00	0.00
Fe+3	0.11	0.11
Fe+2	0.82	0.82
Mn	0.13	0.13
Mg	0.00	0.00
Ca	0.00	0.00
Na	0.00	0.00
K	0.00	0.00
Cr	0.00	0.00
Ba	0.00	0.00
Zn	0.00	0.00
Total	2.00	2.00

Epidote													
Sample no	**P-225bz**							**M-21**	**M-25**	**P-491**			
DataSet/Poi	9/1.	10/1.	16/1.*	21/1.	23/1.	50/1.	55/1.	61 / 1 .	64 / 1 .	2 / 1 .	5 / 1 .	6 / 1 .	11 / 1 .
SiO2	37.59	36.86	36.97	48.25	51.61	36.70	49.62	37.16	38.21	37.85	39.41	37.39	38.55
TiO2	0.05	0.01	0.93	0.09	0.33	0.07	0.13	0.08	0.08	0.07	0.11	0.06	0.15
Al2O3	23.51	22.56	23.28	20.51	18.65	22.95	20.92	23.15	23.59	24.34	22.09	23.94	24.35
Cr2O3	0.00	0.19	0.09	0.00	0.10	0.00	0.00	0.07	0.00	0.00	0.00	0.00	0.00
FeO	11.46	12.26	11.19	9.35	8.53	12.27	8.17	10.80	12.35	11.28	11.73	11.93	10.74
MnO	0.53	0.75	0.50	0.43	0.39	2.40	0.39	0.24	0.49	0.74	0.89	0.77	0.62
MgO	0.00	0.00	0.00	0.01	0.00	0.07	0.00	0.04	0.02	0.00	0.02	0.03	0.01
CaO	22.86	20.38	22.66	19.27	17.59	17.77	15.07	22.42	23.05	21.97	18.85	20.86	22.40
BaO	0.00	0.00	0.00	0.00	0.00	0.00	0.00	0.00	0.00	0.00	0.00	0.00	0.00
Na2O	0.00	0.04	0.02	0.02	0.03	0.00	2.42	0.02	0.00	0.02	0.00	0.00	0.02
K2O	0.00	0.10	0.00	0.03	0.00	0.01	0.03	0.02	0.01	0.02	0.02	0.00	0.00
P2O5	0.33	0.18	0.20	0.20	0.30	0.22	0.18	0.00	0.00	0.00	0.00	0.00	0.00
Total	96.34	93.33	95.84	98.17	97.53	92.46	96.93	94.01	97.79	96.33	93.15	95.00	96.84
Oxygen bas	12.5	12.5	12.5	12.5	12.5	12.5	12.5	12.5	12.5	12.5	12.5	12.5	12.5
Si4+	3.02	3.06	2.99	3.66	3.88	3.07	3.76	3.25	3.23	3.23	3.44	3.24	3.26
Ti4+	0.00	0.00	0.06	0.01	0.02	0.00	0.01	0.01	0.00	0.00	0.01	0.00	0.01
Al3+	2.23	2.21	2.22	1.83	1.65	2.26	1.87	2.38	2.35	2.45	2.27	2.44	2.42
Cr3+	0.00	0.01	0.01	0.00	0.01	0.00	0.00	0.01	0.00	0.00	0.00	0.00	0.00
Fe3+	0.69	0.77	0.68	0.53	0.48	0.77	0.47	0.79	0.87	0.80	0.86	0.86	0.76
Mn2+	0.04	0.05	0.03	0.03	0.02	0.17	0.03	0.02	0.03	0.05	0.07	0.06	0.04
Mg2+	0.00	0.00	0.00	0.00	0.00	0.01	0.00	0.01	0.00	0.00	0.00	0.00	0.00
Ca2+	1.97	1.81	1.97	1.56	1.42	1.59	1.22	2.10	2.09	2.01	1.76	1.93	2.03
Ba2+	0.00	0.00	0.00	0.00	0.00	0.00	0.00	0.00	0.00	0.00	0.00	0.00	0.00
Na+	0.00	0.01	0.00	0.00	0.00	0.00	0.36	0.00	0.00	0.00	0.00	0.00	0.00
K+	0.00	0.01	0.00	0.00	0.00	0.00	0.00	0.00	0.00	0.00	0.00	0.00	0.00
P5+	0.02	0.01	0.01	0.01	0.02	0.02	0.01	0.00	0.00	0.00	0.00	0.00	0.00
Total	7.98	7.94	7.98	7.64	7.50	7.89	7.72	8.56	8.59	8.52	0.00	0.00	0.00

Table 2a. Compositional matrices used in SVD analysis for reaction modelling: matrix used for garnet and amphibole reaction in gabbro

Phase	Si	Ti	Al	Mg	Fetotal	Ca	Na	K	Mn	O	H	
Grt(9)		2.958	0.000	1.954	0.262	2.108	0.538	0.000	0.000	0.175	12	0
Plag(11)		2.513	0.001	1.455	0.008	0.019	0.478	0.501	0.023	0.002	8	0
Opx(14)		1.969	0.000	0.022	0.782	1.175	0.019	0.002	0.000	0.032	6	0
Fe-Hbl(10)		6.608	0.022	2.098	1.923	2.525	1.870	0.326	0.204	0.011	24	2
Mn		0	0	0	0	0	0	0	0	1	0	0
O2		0	0	0	0	0	0	0	0	0	2	0
AqSiO2		1	0	0	0	0	0	0	0	0	2	0
H2O		0	0	0	0	0	0	0	0	0	1	2
K		0	0	0	0	0	0	0	1	0	0	0
Na		0	0	0	0	0	0	1	0	0	0	0
Ca		0	0	0	0	0	1	0	0	0	0	0
Fe		0	0	0	0	1	0	0	0	0	0	0
Mg		0	0	0	1	0	0	0	0	0	0	0
Al		0	0	1	0	0	0	0	0	0	0	0
Ti		0	1	0	0	0	0	0	0	0	0	0

Table 2b. Compositional matrices used in SVD analysis for reaction modelling: matrix used for amphibole reaction in gabbro

Phase	Si	Ti	Al	Mg	Fetotal	Ca	Na	K	O	H	
Plag(14)		2.365	0.000	1.599	0.001	0.011	0.637	0.382	0.005	8	0
Cpx(1)		1.967	0.002	0.041	0.737	0.281	0.925	0.025	0.003	6	0
Amph(15)		7.398	0.061	1.374	2.898	1.888	2.038	0.197	0.086	24	2
O2		0	0	0	0	0	0	0	0	2	0
AqSiO2		1	0	0	0	0	0	0	0	2	0
H2O		0	0	0	0	0	0	0	0	1	2
K		0	0	0	0	0	0	0	1	0	0
Na		0	0	0	0	0	0	1	0	0	0
Ca		0	0	0	0	0	1	0	0	0	0
Fe		0	0	0	0	1	0	0	0	0	0
Mg		0	0	0	1	0	0	0	0	0	0
Al		0	0	1	0	0	0	0	0	0	0
Ti		0	1	0	0	0	0	0	0	0	0

Table 2c. Compositional matrices used in SVD analysis for reaction modelling: matrix used for titanite reaction in gabbro

Phase	Si	Ti	Al	Mg	Fetotal	Ca	Na	K	O	H	
Plag(17)		2.507	0.001	1.449	0	0	0.506	0.526	0.007	8	0
Ilm(8)		0.001	0.994	0.004	0.023	0.929	0.001	0	0.000	3	0
Ttn(9)		0.988	0.954	0.032	0.001	0.006	1.016	6E-05	0	5	0
O2		0	0	0	0	0	0	0	0	2	0
AqSiO2		1	0	0	0	0	0	0	0	2	0
H2O		0	0	0	0	0	0	0	0	1	2
K		0	0	0	0	0	0	0	1	0	0
Na		0	0	0	0	0	0	1	0	0	0
Ca		0	0	0	0	0	1	0	0	0	0
Fe		0	0	0	0	1	0	0	0	0	0
Mg		0	0	0	1	0	0	0	0	0	0
Al		0	0	1	0	0	0	0	0	0	0
Ti		0	1	0	0	0	0	0	0	0	0

Table 2d. Compositional matrices used in SVD analysis for reaction modelling: matrix used for epidote–quartz–titanite reaction in granite

Phase	Si	Ti	Al	Fetotal	Mn	Mg	Ca	Na	K	O	H	
Amp(4)		6.314	0.096	2.236	4.187	0.106	0.337	1.868	0.429	0.424	24	2
Ep(3)		2.979	0.056	2.211	0.754	0.034	0	1.956	0.003	0	13	1
Ttn(7)		1.034	0.771	0.205	0.072	0.007	0.003	0.903	0.005	0	5	0
Qz		1	0	0	0	0	0	0	0	0	2	0
Ti		0	1	0	0	0	0	0	0	0	0	0
Al		0	0	1	0	0	0	0	0	0	0	0
Fetotal		0	0	0	1	0	0	0	0	0	0	0
Mn		0	0	0	0	1	0	0	0	0	0	0
Mg		0	0	0	0	0	1	0	0	0	0	0
Ca		0	0	0	0	0	0	1	0	0	0	0
Na		0	0	0	0	0	0	0	1	0	0	0
K		0	0	0	0	0	0	0	0	1	0	0
O2		0	0	0	0	0	0	0	0	0	2	0
H2O		0	0	0	0	0	0	0	0	0	1	2

Table 2e. Compositional matrices used in SVD analysis for reaction modelling: matrix used for garnet reaction in granite

Phase	Si	Ti	Al	Fetotal	Mn	Mg	Ca	Na	K	O	H
Amp(4)	6.314	0.096	2.236	4.187	0.106	0.337	1.868	0.429	0.424	24	2
Pl(3)	2.884	0	1.118	0.003	0	0.002	0.114	0.864	0.010	8	0
Grt(3)	2.970	0.002	1.914	1.299	0.745	0.010	1.030	0.003	0.023	12	0
Qz	1	0	0	0	0	0	0	0	0	2	0
Ti	0	1	0	0	0	0	0	0	0	0	0
Al	0	0	1	0	0	0	0	0	0	0	0
Fetotal	0	0	0	1	0	0	0	0	0	0	0
Mn	0	0	0	0	1	0	0	0	0	0	0
Mg	0	0	0	0	0	1	0	0	0	0	0
Ca	0	0	0	0	0	0	1	0	0	0	0
Na	0	0	0	0	0	0	0	1	0	0	0
K	0	0	0	0	0	0	0	0	1	0	0
O2	0	0	0	0	0	0	0	0	0	2	0
H2O	0	0	0	0	0	0	0	0	0	1	2

Table 2f. Compositional matrices used in SVD analysis for reaction modelling: matrix used for titanite reaction in granite

Phase	Si	Ti	Al	Fetotal	Mn	Mg	Ca	Na	K	O
Mag(5)	0.006	0.006	0.004	2.97	0.003	0.001	0.009	0.001	0	4
Ilm(2)	0.001	0.945	0.001	0.923	0.128	0	0	0.002	0	3
Pl(3)	2.884	0	1.118	0.003	0	0.002	0.114	0.864	0.01	8
Ttn(5)	1.035	0.737	0.222	0.056	0.008	0.001	0.936	0.005	0	5
Qz	1	0	0	0	0	0	0	0	0	2
Ti	0	1	0	0	0	0	0	0	0	0
Al	0	0	1	0	0	0	0	0	0	0
Fetotal	0	0	0	1	0	0	0	0	0	0
Mn	0	0	0	0	1	0	0	0	0	0
Mg	0	0	0	0	0	1	0	0	0	0
Ca	0	0	0	0	0	0	1	0	0	0
Na	0	0	0	0	0	0	0	1	0	0
K	0	0	0	0	0	0	0	0	1	0
O2	0	0	0	0	0	0	0	0	0	2

Table 3a: Whole-rock chemical composition for SDFB Gabbro

Analyte Sym	P-939	P-925	P-927	P-933a	DK-87	P-950	P-951	P-952	P-938	DK-63a	DK-63b	P-959	DK-68e	DK-85c	M-22b
SiO2	48.53	49.06	47.95	58.58	43.43	51.01	50.26	51.04	51.36	47.96	47.72	58.94	49.03	51.01	50.4
Al2O3	16.41	16.87	15.72	12.6	14.01	13.64	17.32	14.7	15.22	16.98	14.85	15.09	14.63	13.6	14.91
Fe2O3(T)	11.84	6.51	9.87	8.03	18.18	9.51	6.92	10.67	10.26	13.9	14.78	9.26	9.75	12.03	9.25
MnO	0.185	0.114	0.245	0.151	0.211	0.153	0.129	0.17	0.168	0.219	0.243	0.165	0.174	0.198	0.165
MgO	6.83	9.72	5.05	6.57	6.38	10.34	8.74	7.21	7.35	3.79	4.43	2.8	7.23	6.57	8.49
CaO	12.73	14.9	13.79	9.34	10.33	10.45	14.48	11.6	11.67	10.05	10.65	7.44	12.59	11.05	13.5
Na2O	1.14	1.08	2.2	2.34	2.14	3.26	1.46	2.29	1.66	3.27	2.66	1.8	2.15	2.27	2.15
K2O	0.41	0.13	0.92	0.76	0.38	0.15	0.04	0.41	0.34	0.71	0.49	1.27	0.43	0.5	0.15
TiO2	0.734	0.289	1.727	0.834	4.649	0.833	0.243	1.078	0.717	2.331	2.253	0.932	1.101	1.956	0.634
P2O5	0.07	0.04	0.23	0.15	0.12	0.16	< 0.01	0.1	0.12	0.6	0.58	0.12	0.13	0.25	0.04
LOI	1.65	1.27	0.85	0.97	0.59	1.06	0.83	0.95	0.84	0.74	0.63	0.63	1.18	1.21	0.87
Total	100.5	99.98	98.53	100.3	100.4	100.6	100.4	100.2	99.72	100.5	99.29	98.44	98.4	100.6	100.6
Sc	42	45	60	16	39	36	41	44	38	32	42	31	46	45	53
Be	< 1	< 1	2	2	< 1	< 1	< 1	< 1	1	1	1	2	< 1	1	< 1
V	233	154	208	96	490	206	161	302	216	177	168	191	230	290	234
Ba	69	29	209	70	89	78	22	61	103	252	190	311	195	144	48
Sr	213	113	379	353	189	300	120	126	141	304	242	148	171	213	82
Y	14	7	30	26	14	21	6	25	18	33	35	24	23	29	17
Zr	49	13	95	178	53	85	6	56	54	184	150	144	91	144	23
Cr	140	930	30	60	< 20	440	450	230	150	40	80	< 20	560	70	360
Co	52	60	55	49	68	76	58	60	56	44	44	46	46	51	47
Ni	20	180	50	50	120	170	110	100	40	60	50	20	80	60	60
Cu	20	80	60	20	60	50	30	60	20	30	30	40	50	30	80
Zn	90	< 30	90	100	90	80	50	80	90	150	150	90	80	90	70
Ga	16	12	17	16	18	13	12	15	16	20	18	17	15	16	14
Ge	2	1	2	2	1	1	1	1	2	1	2	1	2	2	2
As	< 5	< 5	< 5	< 5	< 5	< 5	< 5	< 5	< 5	< 5	< 5	< 5	< 5	< 5	< 5
Rb	17	8	16	9	11	2	< 2	7	15	24	15	53	14	12	6
Nb	3	< 1	16	10	4	1	< 1	< 1	3	11	10	7	4	7	< 1
Mo	< 2	< 2	< 2	< 2	< 2	< 2	< 2	< 2	< 2	< 2	< 2	< 2	< 2	< 2	< 2

Table 3a: Whole-rock chemical composition for SDFB Gabbro

Analyte Sym	P-939	P-925	P-927	P-933a	DK-87	P-950	P-951	P-952	P-938	DK-63a	DK-63b	P-959	DK-68e	DK-85c	M-22b
Ag	< 0.5	< 0.5	< 0.5	< 0.5	< 0.5	< 0.5	< 0.5	< 0.5	< 0.5	< 0.5	< 0.5	< 0.5	< 0.5	< 0.5	< 0.5
In	< 0.2	< 0.2	< 0.2	< 0.2	< 0.2	< 0.2	< 0.2	< 0.2	< 0.2	< 0.2	< 0.2	< 0.2	< 0.2	< 0.2	< 0.2
Sn	< 1	< 1	2	2	< 1	1	< 1	< 1	1	1	1	2	< 1	1	< 1
Sb	< 0.5	< 0.5	< 0.5	< 0.5	< 0.5	< 0.5	< 0.5	< 0.5	< 0.5	< 0.5	< 0.5	< 0.5	0.6	< 0.5	< 0.5
Cs	1.6	0.5	1.2	< 0.5	1.4	< 0.5	< 0.5	< 0.5	1.3	3	1.8	1.3	3.4	1	< 0.5
La	8.6	0.4	23.5	29.1	3.2	12.6	0.2	2.3	14.1	14.8	13.8	26.5	7.4	15.4	1.9
Ce	18.9	1.5	53.4	65	7.9	30.3	1	7.6	33	34.4	32.5	54.3	16.9	32.4	4.6
Pr	2.33	0.26	6.47	7.58	1.18	3.96	0.13	1.26	3.79	4.78	4.6	6.04	2.38	4.25	0.69
Nd	10.5	1.9	27.2	30.8	5.8	18.3	1.1	7.7	16.5	24.4	23.1	25.1	12.1	19.8	4.1
Sm	2.3	0.8	6.2	6.2	2	4	0.3	2.8	3.8	6.4	6.1	5.1	3.5	5	1.5
Eu	0.97	0.38	1.36	1.41	1.2	1.27	0.4	1.09	1.03	3.22	2.86	1.3	1.39	1.53	0.64
Gd	2.5	1.1	5.9	5.6	2.5	3.9	0.7	4.1	3.8	7.1	7.2	4.9	4.1	5.7	2.4
Tb	0.4	0.2	1	0.9	0.4	0.7	0.1	0.7	0.6	1.1	1.2	0.8	0.7	0.9	0.4
Dy	2.5	1.6	6.3	5.5	3	4.1	1.1	5.2	3.9	7	7.6	5.1	4.8	6.1	3.2
Ho	0.5	0.3	1.3	1.1	0.6	0.9	0.2	1.1	0.8	1.4	1.5	1	1	1.3	0.7
Er	1.5	0.9	3.6	3.2	1.6	2.5	0.7	3.3	2.4	4.2	4.4	3	2.9	3.6	2
Tm	0.21	0.12	0.53	0.45	0.23	0.37	0.1	0.48	0.33	0.58	0.59	0.41	0.38	0.47	0.28
Yb	1.5	0.8	3.6	3	1.4	2.4	0.6	3.3	2.3	3.5	3.9	2.9	2.6	3.2	1.9
Lu	0.23	0.13	0.59	0.49	0.22	0.39	0.09	0.54	0.35	0.56	0.63	0.45	0.44	0.54	0.3
Hf	1.3	0.5	3.1	5.4	1.6	2.7	< 0.2	2	1.7	4.6	4	4.2	2.6	4	0.9
Ta	0.6	0.5	2.4	1.7	0.4	0.2	0.4	0.5	0.4	1.1	2.3	0.7	0.4	0.6	< 0.1
W	159	177	176	312	70	129	152	173	181	139	149	257	118	127	89
Tl	< 0.1	< 0.1	< 0.1	< 0.1	< 0.1	< 0.1	< 0.1	< 0.1	< 0.1	< 0.1	< 0.1	0.1	< 0.1	< 0.1	< 0.1
Pb	15	< 5	12	7	< 5	< 5	< 5	10	7	18	14	11	19	6	< 5
Bi	< 0.4	< 0.4	< 0.4	< 0.4	< 0.4	< 0.4	< 0.4	< 0.4	< 0.4	< 0.4	< 0.4	< 0.4	< 0.4	< 0.4	< 0.4
Th	1.7	< 0.1	1.6	9.7	0.2	3.9	< 0.1	0.8	4.5	1.8	1.6	5	0.9	3.4	0.3
U	0.4	< 0.1	0.3	1.1	< 0.1	0.7	< 0.1	0.3	0.7	0.4	0.4	0.1	0.2	0.5	< 0.1

Table 3b: Whole-rock chemical composition for SDFB granite

Sample	P-814	P-106	P-472	P-697	M-21	M-25	P-176	P-212A	P-225B	P-245A	P-300	P-321
Rock Type	Granite	Granite	Granite	Granite	Granite	Granite	Granite	Granite	Granite	Granite	Granite	Granite
SiO2	77.82	75.58	75.31	75.4	76.11	72.26	75.31	75.32	75.07	76.06	75.66	76.03
Al2O3	11.67	12.17	12.3	13.2	11.81	13.96	12.28	12.36	12.3	12.51	12.18	12.21
Fe2O3	1.56	2.32	2.17	1.56	1.59	3.27	2.19	2.31	2.31	1.32	2.14	2
MgO	0.04	0.12	0.06	0.16	0.16	0.45	0.05	0.1	0.12	0.04	0.14	0.1
CaO	1.01	1.23	1.1	0.7	0.85	2.39	1.14	1.27	1.3	1.1	1.24	0.86
Na2O	3.61	3.64	3.79	5.18	2.95	4.91	3.79	3.83	3.56	3.88	3.94	3.59
K2O	3.37	3.73	3.87	2.86	5.26	1.58	3.9	3.53	4	3.89	3.3	4.02
TiO2	0.14	0.18	0.15	0.1	0.14	0.26	0.15	0.18	0.18	0.13	0.16	0.15
P2O5	0.02	0.02	0.01	0.04	0.02	0.09	0.02	0.06	0.02	0.02	0.02	0.08
MnO	0.02	0.06	0.05	0.06	0.02	0.07	0.05	0.06	0.06	0.03	0.04	0.04
Ba	530	724	696	283	476	374	717	649	757	616	512	679
Sc	2	6	5	2	3	12	5	6	7	5	5	5
LOI	0.4	0.6	0.8	0.5	0.8	0.6	0.7	0.6	0.7	0.7	0.8	0.5
Sum	99.26	99.05	98.81	99.26	98.91	99.24	98.88	99.02	98.92	98.98	98.82	99.08
Be	1	3	2	3	6	1	2	4	2	4	5	3
Co	118.9	106.6	109	66	92.9	66.4	141.2	136.4	147.8	139.5	158.4	152.3
Cs	0.3	2.7	1.7	6.9	8.9	2.5	3	1.8	2.4	1.3	3.4	5
Ga	28.4	23.2	24.1	26.1	19.2	17.1	22.6	21.6	22.4	22.3	21.5	21.3
Hf	14.9	11.3	12.8	8.6	7.5	6.7	11	10.4	10.6	11.2	9.9	10.1
Nb	12.7	22.2	24.7	28.8	23.2	6.4	20.9	15.6	20.7	24.2	16.4	20.1
Rb	65.7	122.7	138.8	122.5	270.5	53.3	125.7	107.7	121.5	129.6	130.5	141.4
Sn	3	5	6	5	5	3	4	4	5	8	5	5
Sr	101.7	50.1	52.2	23	34.8	82.7	46.1	52.8	52.6	94.2	44.7	45.3
Ta	3	3.4	3.4	2.7	2.2	0.6	3.9	3.5	4.3	4.7	4	4.3
Th	6.8	20.5	21.5	19.9	32	7.9	18.3	17.8	18.2	19.2	16.8	17.6
U	1.2	1.7	2.2	2.6	4.7	0.8	2.1	1.4	1.4	1.7	1.9	1.6
V	<8	<8	<8	<8	<8	12	<8	<8	<8	<8	<8	<8
W	989.7	897.6	938.8	585	788	578.5	1235	1134.5	1241.9	1219.2	1324.4	1325

Table 3b: Whole-rock chemical composition for SDFB granite

Sample	P-814	P-106	P-472	P-697	M-21	M-25	P-176	P-212A	P-225B	P-245A	P-300	P-321
Zr	331.8	296	321.7	137.5	207.5	219.3	290.6	280.7	283.2	274.9	261.8	256.5
Y	218	153.6	167.1	106.1	104.5	56.5	161.7	127.3	159.9	137.8	132.1	123.9
La	39.7	68.7	68.4	12.3	57.1	27.7	63	60.8	63.7	34.7	54.8	40.8
Ce	109	145.1	149.7	29.3	132.1	60.7	138.8	138.4	146.7	111.1	110.3	95.4
Pr	16.58	19.13	19.21	4.21	14.91	7.54	18.18	17.56	18.53	10.36	14.97	12.21
Nd	78.6	80.4	79.2	18.2	56.9	30.2	77.6	72.3	78.4	43	63.3	50.2
Sm	23.96	20.29	20.38	6.04	13.2	8	19.53	17.76	20.55	12.35	15.54	12.91
Eu	3.57	3.26	3.53	0.56	1.27	1.36	3.42	2.99	3.33	2.35	2.58	2.25
Gd	29.92	23.09	24.17	8.38	14.36	8.89	23.77	20.7	24.15	16.35	19.01	15.92
Tb	6.06	4.33	4.42	1.93	2.73	1.57	4.31	3.7	4.44	3.3	3.42	3.07
Dy	40.15	26.87	28.74	14.3	17.78	9.82	27.89	23.62	28.17	22.91	21.97	20.24
Ho	8.92	5.93	6.36	3.57	3.98	2.12	6.15	5.05	6.39	5.09	4.83	4.58
Er	27.33	17.92	19.32	12.64	12.44	6.37	18.55	14.94	18.84	15.96	14.52	14.77
Tm	3.96	2.63	2.84	2.28	1.83	0.89	2.59	2.05	2.71	2.36	2.12	2.21
Yb	24.87	16.89	18.05	17	11.99	5.45	16.73	12.7	17.48	15.63	13.7	14.54
Lu	3.86	2.56	2.82	2.82	1.81	0.91	2.58	1.83	2.63	2.44	2.1	2.28
Mo	0.5	0.6	0.8	0.1	0.1	0.2	1.1	0.7	0.7	0.5	1.2	1.4
Cu	0.5	0.2	0.5	1.1	0.7	16.6	0.9	0.8	0.5	1	1.3	7.2
Pb	1.2	2.1	6.1	4.1	12.1	1.7	2.7	3.2	2.3	3.7	2.4	3.2
Zn	23	103	97	141	41	60	113	96	106	33	100	98
Ni	1.8	1.5	1.2	1.3	1.4	1.5	1.7	1.9	1.9	2.5	2	2.7
As	<0.5	<0.5	<0.5	<0.5	<0.5	<0.5	<0.5	<0.5	<0.5	<0.5	<0.5	<0.5
Sb	<0.1	<0.1	<0.1	<0.1	<0.1	<0.1	<0.1	<0.1	<0.1	<0.1	<0.1	<0.1
Bi	<0.1	<0.1	<0.1	<0.1	<0.1	1	<0.1	<0.1	<0.1	<0.1	<0.1	<0.1
Ag	<0.1	<0.1	<0.1	<0.1	<0.1	<0.1	<0.1	<0.1	<0.1	<0.1	<0.1	<0.1
Tl	<0.1	0.2	<0.1	0.3	0.4	0.3	0.2	0.2	0.2	<0.1	0.3	0.2
(La/Sm)N	1.071	2.188	2.1691	1.3162	2.7955	2.2375	2.085	2.2125	2.0035	1.8156	2.2791	2.0423
(La/Yb)N	1.1455	2.919	2.7195	0.5191	3.4174	3.6489	2.702	3.4356	2.6148	1.5934	2.8705	2.0139
(Eu/Eu*)N	0.41	0.46	0.49	0.24	0.28	0.49	0.49	0.48	0.46	0.51	0.46	0.48
(La)N	128.06	221.6	220.65	39.68	184.19	89.35	203.2	196.13	205.48	111.94	176.77	131.61
(Gd/Yb)N	0.9708	1.103	1.0806	0.3978	0.9664	1.316	1.147	1.3151	1.1148	0.8442	1.1198	0.8836

Table 4a: LA-ICP-MS U-Pb Zircon Age data in Gabbro (DK-67b, DC-2/P-927).

Sample no	U	Th	$^{207}Pb/^{206}Pb$	±2σ	$^{207}Pb/^{235}U$	±2σ	$^{206}Pb/^{238}U$	±2σ	$^{207}Pb/^{206}Pb$	±2σ	$^{207}Pb/^{235}U$	±2σ	$^{206}Pb/^{238}U$	±2σ	% degree of discordance	
	ppm		Ratio & error						U-Pb age (Ma)							Th/U
DC2-1a			0.074	0.010	1.677	15.3	0.164	5.9	1050	314	1000.0	102.3	977.4	53.7	2.3%	0.446
DC2-1b			0.078	0.010	1.685	14.5	0.157	5.9	1139	288	1002.8	96.9	941.8	51.9	6.5%	0.586
DC2-1c			0.081	0.009	1.697	13.0	0.151	5.8	1230	247	1007.3	86.6	908.4	49.3	10.9%	0.386
DC2-1d			0.071	0.010	1.475	15.2	0.152	6.3	944	312	920.2	96.4	910.2	53.7	1.1%	0.715
DC2-2a			0.086	0.010	1.968	13.1	0.166	5.3	1339	252	1104.5	92.3	989.4	48.8	11.6%	0.559
DC2-2b			0.076	0.009	1.713	13.2	0.164	5.4	1087	261	1013.5	88.4	980.0	49.3	3.4%	0.463
DC2-2c			0.070	0.011	1.537	16.6	0.159	6.5	928	351	945.4	107.6	952.7	57.8	-0.8%	0.374
DC2-2d			0.062	0.012	1.468	20.8	0.171	8.0	685	474	917.3	134.1	1017.1	75.7	-9.8%	0.370
DK67-3a			0.096	0.017	2.102	19.2	0.159	8.1	1551	368	1149.6	141.5	948.8	71.9	21.2%	0.346
DK67-3b			0.082	0.019	1.905	24.1	0.169	7.8	1242	527	1082.8	174.7	1005.3	73.0	7.7%	0.505
DK67-3c			0.080	0.012	1.809	16.2	0.164	7.1	1198	319	1048.7	111.9	978.7	64.8	7.2%	0.482
DK67-3d			0.088	0.015	2.090	19.2	0.172	8.1	1389	377	1145.5	141.2	1021.1	76.9	12.2%	0.532
DK67-4a			0.076	0.005	1.698	7.8	0.163	4.1	1082	138	1007.9	51.1	974.1	37.2	3.5%	0.900
DK67-4b			0.071	0.004	1.665	7.0	0.169	3.4	967	130	995.4	45.4	1008.3	31.8	-1.3%	0.948
DK67-4c			0.067	0.004	1.510	7.0	0.163	3.3	847	135	934.4	43.7	971.9	29.8	-3.9%	0.849
DK67-4d			0.070	0.006	1.612	10.2	0.168	4.6	922	199	975.0	66.0	998.6	42.7	-2.4%	0.684
DK67-5a			0.073	0.007	1.710	10.9	0.170	4.5	1014	215	1012.3	72.4	1011.4	42.3	0.1%	0.785
DK67-5b			0.064	0.007	1.526	12.6	0.173	4.9	746	266	941.0	80.4	1026.3	46.7	-8.3%	0.631
DK67-6a			0.076	0.004	1.695	6.7	0.162	3.6	1097	119	1006.7	43.7	966.0	32.4	4.2%	0.926
DK67-6b			0.069	0.004	1.560	6.7	0.164	3.2	901	127	954.3	42.3	977.4	29.1	-2.4%	0.861
DK67-7a			0.071	0.013	1.581	20.1	0.161	8.4	961	427	962.7	133.4	963.6	75.6	-0.1%	0.439
DK67-7b			0.074	0.004	1.739	6.4	0.170	3.2	1045	115	1023.2	42.1	1013.1	30.1	1.0%	1.024
DK67-8a			0.074	0.003	1.618	5.5	0.159	2.8	1036	98	977.1	35.1	951.0	24.8	2.7%	0.950
DK67-8b			0.069	0.006	1.556	8.9	0.163	4.0	905	174	953.0	56.6	974.1	36.3	-2.2%	0.708
DK67-9a			0.075	0.006	1.723	9.3	0.167	4.1	1058	179	1017.1	61.6	998.0	38.0	1.9%	0.770
DK67-9b			0.078	0.008	1.755	10.6	0.163	4.3	1146	206	1029.1	71.0	975.0	39.0	5.5%	0.777
DK67-10a			0.075	0.005	1.695	7.9	0.163	4.3	1075	139	1006.6	51.7	975.4	39.0	3.2%	0.656
DK67-10b			0.067	0.005	1.601	7.9	0.172	3.9	853	150	970.5	50.6	1023.2	37.0	-5.2%	0.832

Sample no	U	Th	$^{207}Pb/^{206}Pb$	±2σ	$^{207}Pb/^{235}U$	±2σ	$^{206}Pb/^{238}U$	±2σ	$^{207}Pb/^{206}Pb$	±2σ	$^{207}Pb/^{235}U$	±2σ	$^{206}Pb/^{238}U$	±2σ	% degree of discordance	
	ppm		Ratio & error						U-Pb age (Ma)							Th/U
DK67-11a			0.076	0.010	1.736	14.9	0.166	6.0	1093	300	1022.2	100.9	989.5	55.3	3.3%	0.587
DK67-11b			0.077	0.005	1.759	7.2	0.166	3.6	1115	129	1030.4	47.7	991.0	33.2	4.0%	0.934
DK67-12a			0.071	0.006	1.610	9.6	0.163	4.3	971	186	973.9	62.0	975.3	39.0	-0.1%	0.807
183Dc1a			0.070	0.006	1.481	10.0	0.153	5.2	933	187	922.6	62.5	918.2	44.7	0.5%	0.306
184Dc1b			0.072	0.006	1.607	9.3	0.162	4.6	983	174	973.0	59.9	968.8	41.5	0.4%	0.500
185Dc1c			0.070	0.005	1.690	9.1	0.175	4.9	931	167	1004.7	59.8	1038.9	47.2	-3.3%	0.498
186Dc1d			0.067	0.005	1.430	8.4	0.154	4.6	852	153	901.6	51.5	921.9	39.6	-2.2%	0.557
187Dc2a			0.078	0.006	1.878	8.7	0.176	4.5	1136	157	1073.2	59.3	1042.7	43.5	2.9%	0.395
188Dc2b			0.073	0.006	1.732	9.0	0.171	4.4	1025	166	1020.4	59.7	1018.2	41.6	0.2%	0.451
189Dc2c			0.074	0.007	1.639	10.5	0.160	5.2	1054	195	985.3	68.5	954.7	46.3	3.2%	0.431
190Dc2d			0.084	0.008	1.894	10.3	0.163	4.4	1294	193	1079.1	70.9	976.0	40.0	10.6%	0.428
193DK1a			0.071	0.009	1.549	14.9	0.158	6.7	960	299	950.1	96.4	945.8	59.2	0.5%	0.461
194DK1b			0.076	0.010	1.702	14.9	0.163	6.8	1083	293	1009.3	100.1	975.8	61.9	3.4%	0.452
195DK1c			0.064	0.009	1.483	16.0	0.167	7.5	750	330	923.5	102.0	997.7	69.7	-7.4%	0.431
196DK1d			0.080	0.012	1.794	17.2	0.163	7.7	1189	339	1043.3	118.8	975.4	70.1	7.0%	0.387
197DK2a			0.071	0.004	1.565	6.1	0.161	3.3	944	108	956.3	38.5	961.8	29.6	-0.6%	0.851
198DK2b			0.074	0.002	1.573	4.2	0.154	2.9	1044	62	959.6	26.4	923.4	25.0	3.9%	1.015
199DK2c			0.070	0.002	1.638	4.2	0.169	2.9	939	63	984.8	26.8	1005.4	27.1	-2.0%	1.100
200DK3a			0.068	0.007	1.533	11.5	0.164	6.2	857	216	943.7	73.3	981.3	56.7	-3.8%	0.477
201DK3b			0.078	0.006	1.530	8.3	0.142	3.7	1151	154	942.4	52.3	855.7	29.7	10.1%	0.807
204DK4a			0.073	0.003	1.516	5.3	0.151	3.5	1007	83	936.9	33.0	907.4	29.7	3.3%	0.773
205DK5			0.072	0.007	1.660	10.5	0.168	4.0	972	212	993.2	68.8	1002.9	37.3	-1.0%	0.544
206DK6			0.071	0.003	1.610	4.8	0.165	3.0	945	80	974.1	30.5	987.2	27.5	-1.3%	0.847
207DK7			0.070	0.004	1.571	6.3	0.162	3.1	936	117	959.0	39.9	969.1	28.0	-1.0%	0.769
208DK8			0.071	0.006	1.463	9.8	0.149	3.8	968	195	915.1	60.9	893.3	31.8	2.4%	0.692
209DK9a			0.074	0.003	1.661	5.6	0.163	3.4	1040	92	993.9	36.1	973.3	30.8	2.1%	0.831
210DK9b			0.074	0.009	1.616	13.4	0.159	5.9	1038	263	976.3	87.7	949.3	52.3	2.8%	0.370

Table 4b: LA-ICP-MS U-Pb Zircon Age data in granite (P-472,P-106,DK-67 and M-25).

Sample no	U	Th	$^{207}Pb/^{206}Pb$	±2σ	$^{207}Pb/^{235}U$	±2σ	$^{206}Pb/^{238}U$	±2σ	$^{207}Pb/^{206}Pb$	±2σ	$^{207}Pb/^{235}U$	±2σ	$^{206}Pb/^{238}U$	±2σ	% degree of discordance	
	ppm		Ratio & error						U-Pb age (Ma)							
								Concordant								Th/U
P-472 - 3	893	409	0.075	0.001	1.65	0.056	0.159	0.006	1055	33	988	22	951.6	31	9.80	0.458
P-472 - 25	227.1	145.1	0.074	0.002	1.65	0.055	0.162	0.006	1041	44	990	21	969.8	31	6.84	0.639
P-472 - 13	298	191.4	0.074	0.002	1.68	0.059	0.165	0.006	1045	43	1003	23	985.5	30	5.69	0.642
P-472 - 15	448	354	0.073	0.001	1.63	0.055	0.161	0.005	1014	38	982	21	959.4	30	5.38	0.790
P-472 - 2_1	558	332	0.074	0.001	1.69	0.054	0.166	0.006	1029	37	1002.5	20	987.7	31	4.01	0.595
P-472 - 1	440	91.6	0.072	0.001	1.59	0.053	0.161	0.005	965	40	965	21	961.1	30	0.40	0.208
P-472 - 14	239.2	163.8	0.071	0.002	1.59	0.053	0.164	0.006	945	42	964.4	21	976.9	30	-3.38	0.685
P-472 - 16	251	127	0.070	0.001	1.54	0.058	0.160	0.006	913	44	947	24	954	31	-4.49	0.506
P-472 - 12	879	73.5	0.069	0.001	1.31	0.042	0.137	0.005	899	38	851.4	19	829.2	26	7.76	0.084
								Discordant								
P-472 - 11	1065	458	0.094	0.002	0.88	0.160	0.100	0.004	891	130	632	89	616.4	24	30.82	0.430
P-472 - 26	1400	728	0.075	0.001	1.27	0.042	0.123	0.004	1066	34	833.9	18	748.3	24	29.80	0.520
P-472 - 17	1071	360	0.076	0.001	1.45	0.045	0.138	0.005	1093	32	909.8	19	833.7	27	23.72	0.336
P-472 - 23	336.1	205.6	0.082	0.002	1.82	0.061	0.162	0.006	1245	42	1052	22	968.3	31	22.22	0.612
P-472 - 9	402	308	0.076	0.002	1.55	0.051	0.144	0.005	1106	55	948.3	21	866.5	29	21.65	0.766
P-472 - 19	691	323	0.076	0.002	1.48	0.048	0.143	0.005	1087	41	920.3	20	859	29	20.98	0.467
P-472 - 21	736	1070	0.102	0.003	1.33	0.170	0.142	0.007	1060	130	850	73	856	41	19.25	1.454
P-472 - 5	1246	803	0.076	0.001	1.57	0.050	0.148	0.005	1097	33	955.9	20	890.7	29	18.81	0.644
P-472 - 22	679	710	0.078	0.002	1.26	0.170	0.141	0.006	999	97	813	79	854	33	14.51	1.046
P-472 - 18	521	470	0.074	0.001	1.56	0.050	0.153	0.005	1046	36	956.5	19	915.6	29	12.47	0.902
P-472 - 7	452	308	0.072	0.002	1.47	0.049	0.147	0.005	988	41	918	20	886.2	28	10.30	0.681

Concordant

P-106 - 38	556	178	0.070	0.001	1.58	0.054	0.162	0.006	914	40	960	21	970.4	32	-6.17	0.320
P-106 - 24	439	276.4	0.072	0.001	1.60	0.051	0.160	0.005	975	37	969.8	20	958.2	30	1.72	0.630
P-106 - 29	309	91.4	0.072	0.002	1.62	0.059	0.164	0.006	976	46	978	23	980	32	-0.41	0.296
P-106 - 28	595	193	0.071	0.001	1.58	0.052	0.162	0.005	960	37	962	21	966.6	30	-0.69	0.324
P-106 - 23	432	220.1	0.071	0.001	1.61	0.054	0.162	0.006	960	37	973.7	20	970.2	31	-1.06	0.509
P-106 - 4	623	332.5	0.070	0.002	1.55	0.051	0.159	0.005	940	42	949.4	20	951.6	29	-1.23	0.534
P-106 - 9	179	25.5	0.070	0.003	1.56	0.072	0.160	0.006	939	73	952	28	956	35	-1.81	0.142
P-106 - 36	522	269.8	0.070	0.001	1.54	0.049	0.159	0.005	930	41	948.2	19	952.2	30	-2.39	0.517
P-106 - 25	534	230	0.070	0.001	1.60	0.053	0.164	0.006	945	36	968.4	21	976.9	31	-3.38	0.431
P-106 - 15	577	96.2	0.069	0.001	1.25	0.052	0.132	0.005	882	38	822	24	797	30	9.64	0.167
P-106 - 32	442	110	0.068	0.001	1.30	0.045	0.139	0.005	872	43	848	20	835.8	27	4.15	0.249
P-106 - 3	1335	24.4	0.066	0.001	1.21	0.045	0.134	0.005	817	41	806	21	809	30	0.98	0.018
P-106 - 17	1048	36.5	0.067	0.001	1.22	0.042	0.134	0.005	817	43	808	20	809.2	27	0.95	0.035
P-106 - 13	680	16.5	0.067	0.002	1.28	0.045	0.138	0.005	839	50	835	20	832	26	0.83	0.024
P-106 - 34	646	17.6	0.067	0.001	1.28	0.042	0.139	0.005	833	40	835.7	19	837.2	26	-0.50	0.027
P-106 - 14	770	11.2	0.066	0.001	1.25	0.042	0.137	0.005	819	44	824.1	19	828	26	-1.10	0.015
P-106 - 1_1	1146	18.6	0.066	0.001	1.23	0.040	0.135	0.005	804	41	812	18	813.9	26	-1.23	0.016
P-106 - 33	991	82	0.066	0.001	1.27	0.041	0.138	0.005	815	36	829.4	18	832.7	26	-2.17	0.083

Discordant

P-106 - 16	1052	759	0.075	0.0022	1.502	0.060	0.1444	0.008	1072	59	930	24	869	42	18.937	0.721
P-106 - 10	1780	246	0.071	0.0011	1.355	0.043	0.1389	0.005	952	33	869	19	838.2	27	11.954	0.138
P-106 - 18	2070	3410	0.086	0.0017	0.558	0.060	0.0637	0.002	852	130	446	41	398	14	53.286	1.647
P-106 - 8	1939	1021	0.068	0.0012	1.001	0.031	0.1058	0.004	876	36	705	16	648.4	20	25.982	0.527
P-106 - 6	1424	1450	0.074	0.0012	0.927	0.066	0.1017	0.004	834	100	666	35	624	23	25.18	1.018
P-106 - 7	1357	604	0.068	0.0011	1.13	0.037	0.121	0.004	863	33	768.2	17	736	25	14.716	0.445
P-106 - 5	1580	143	0.068	0.0011	1.183	0.037	0.1271	0.004	863	34	792.1	17	771.2	24	10.637	0.091

Concordant

DK-67 - 14	94.6	67.9	0.074	0.002	1.63	0.062	0.160	0.006	1037	59	982	24	956	31	7.81	0.718
DK-67 - 12	55.4	37.3	0.074	0.003	1.63	0.084	0.160	0.006	1024	87	981	31	955	33	6.74	0.673
DK-67 - 6	176	83.9	0.073	0.002	1.59	0.058	0.161	0.006	1015	49	966	23	962.8	31	5.14	0.477
DK-67 - 2	163	130.3	0.074	0.002	1.66	0.062	0.165	0.006	1030	51	994	24	982.9	31	4.57	0.799
DK-67 - 1	171	57	0.073	0.002	1.64	0.061	0.164	0.006	1016	52	985	23	976.7	31	3.87	0.333
DK-67 - 25	163	120	0.073	0.002	1.62	0.059	0.163	0.006	1011	50	979	23	973.1	31	3.75	0.736
DK-67 - 10	84.3	46.1	0.072	0.002	1.57	0.066	0.159	0.006	978	68	960	25	952	31	2.66	0.547
DK-67 - 22	118	64.2	0.072	0.002	1.63	0.066	0.163	0.006	999	60	977	26	973.4	31	2.56	0.544
DK-67 - 30	160.4	109.5	0.072	0.002	1.63	0.060	0.163	0.006	993	52	984	23	972.9	31	2.02	0.683
DK-67 - 20	211.5	178.8	0.072	0.002	1.59	0.062	0.162	0.006	981	59	971	25	970.2	31	1.10	0.845
DK-67 - 24	115	65.7	0.072	0.002	1.62	0.061	0.163	0.006	983	54	976	23	972.2	31	1.10	0.571
DK-67 - 13	68.1	44.7	0.071	0.002	1.59	0.066	0.162	0.006	945	69	963	26	969	32	-2.54	0.656
DK-67 - 5	108	51.6	0.070	0.003	1.53	0.065	0.159	0.006	921	75	942	25	951	32	-3.26	0.478
DK-67 - 3	116	74.9	0.071	0.002	1.61	0.063	0.166	0.006	947	57	972	24	988	33	-4.33	0.646

Discordant

DK-67 - 9	31.2	13.7	0.080	0.004	1.69	0.093	0.154	0.006	1196	95	1009	35	920	31	23.08	0.439
DK-67 - 16	139.9	81.5	0.076	0.002	1.52	0.057	0.144	0.005	1095	52	935	23	870	29	20.55	0.583
DK-67 - 27	215.7	186	0.074	0.002	1.44	0.052	0.140	0.005	1041	52	904	21	844.6	27	18.87	0.862
DK-67 - 28	171	138.9	0.074	0.002	1.50	0.051	0.146	0.005	1041	48	928	21	879.8	28	15.49	0.812
DK-67 - 34	281	243	0.073	0.002	1.46	0.052	0.145	0.005	1021	49	916	21	870.1	28	14.78	0.865
DK-67 - 26	233	205	0.075	0.002	1.62	0.057	0.156	0.005	1084	49	979	22	934.9	29	13.75	0.880
DK-67 - 15	116.9	73.2	0.076	0.002	1.67	0.062	0.160	0.006	1084	57	999	24	957.9	31	11.63	0.626
DK-67 - 33	646	66	0.069	0.002	1.28	0.045	0.134	0.005	911	44	836	20	807.8	27	11.33	0.102
DK-67 - 17	259	227	0.074	0.002	1.54	0.052	0.152	0.005	1024	43	946	21	909.8	29	11.15	0.876

Concordant

M-25 - 16	210.1	156.1	0.074	0.001	1.63	0.063	0.159	0.004	1028	38	981	24	949	23	7.68	0.743
M-25 - 26	827	431	0.073	0.001	1.58	0.058	0.159	0.004	1006	36	961.6	23	953.3	23	5.24	0.521
M-25 - 1_1	760	720	0.073	0.001	1.61	0.066	0.164	0.005	1008	33	974	26	978	30	2.98	0.947
M-25 - 3	147	83.4	0.072	0.002	1.61	0.083	0.162	0.007	996	53	968	32	968	38	2.81	0.567
M-25 - 10	419	263	0.072	0.001	1.63	0.061	0.164	0.004	1005	35	980.1	24	977.8	24	2.71	0.628
M-25 - 18	190	99	0.072	0.002	1.60	0.064	0.162	0.005	993	42	971	25	968	27	2.52	0.521
M-25 - 12	325	178.6	0.072	0.001	1.61	0.059	0.162	0.004	992	36	975.8	23	967.3	22	2.49	0.550
M-25 - 2_1	514	273	0.073	0.001	1.61	0.076	0.164	0.006	1001	39	974	29	977	35	2.40	0.531
M-25 - 25	488	220	0.072	0.001	1.61	0.069	0.162	0.006	990	39	974	27	968	32	2.22	0.451
M-25 - 34	480	173	0.073	0.001	1.64	0.062	0.165	0.004	1004	39	985	24	981.8	23	2.21	0.360
M-25 - 11	231.1	138.2	0.071	0.001	1.59	0.061	0.161	0.004	968	39	966.2	24	961.8	23	0.64	0.598
M-25 - 20	350	105.8	0.072	0.002	1.63	0.072	0.163	0.006	976	47	978	28	975	34	0.10	0.302

Discordant

M-25 - 14	343	277	0.0784	0.002	0.81	0.040	0.075	0.003	1153	41	598	23	466	20	59.58	0.808
M-25 - 15	400	368.3	0.0756	0.002	0.81	0.032	0.077	0.002	1077	43	600.5	18	479.3	13	55.50	0.921
M-25 - 13	153.2	108.9	0.0724	0.002	1.07	0.046	0.107	0.003	992	50	737	23	655	17	33.97	0.711
M-25 - 5	1059	549	0.0796	0.002	1.25	0.130	0.123	0.006	1040	120	819	61	746	36	28.27	0.518
M-25 - 27	559	352	0.0746	0.001	1.32	0.051	0.129	0.004	1057	36	855.4	22	784.3	20	25.80	0.630
M-25 - 29	800	878	0.0726	0.001	1.26	0.046	0.126	0.003	1002	35	829.8	20	765	18	23.65	1.098
M-25 - 19	884	659	0.0735	0.001	1.33	0.049	0.132	0.004	1027	35	858.8	21	798.3	20	22.27	0.745
M-25 - 24	356	307	0.0742	0.001	1.41	0.052	0.139	0.004	1046	36	892.6	22	838.4	21	19.85	0.862
M-25 - 32	412	286.5	0.0749	0.001	1.48	0.055	0.144	0.004	1061	34	922.9	23	865.4	21	18.44	0.695
M-25 - 22	736	615	0.0728	0.001	1.40	0.052	0.139	0.004	1010	34	885.9	22	840.9	21	16.74	0.836
M-25 - 8	1093	448	0.0746	0.001	1.49	0.059	0.147	0.005	1054	36	927	24	884	25	16.13	0.410
M-25 - 7	1017	400	0.0762	0.001	1.32	0.081	0.135	0.005	963	74	855	34	816	26	15.26	0.393
M-25 - 33	334	262	0.0735	0.001	1.54	0.058	0.152	0.004	1025	34	946.8	23	911.3	22	11.09	0.784